BEAM DISCOVERY AND TRACKING FOR MOBILE MIMO

DISSERTATION

Presented in Partial Fulfillment of the Requirements for the Degree Doctor of
Philosophy in the Graduate School of The Ohio State University

By

Mohamed Naguib Hussein Abdelrazek, B.S, M.S.
Graduate Program in Electrical and Computer Engineering

The Ohio State University

2022

Dissertation Committee

Prof. Can Emre Koksal, Advisor

Prof. Eylem Ekici

Prof. Abhishek Gupta

ABSTRACT

The real-time applications and the IoT promote the need for a newer idle spectrum to support the required high traffic. This pushes toward the emergence of the millimeter-wave (mmWave) and the sub-Terahertz (sub-THz) bands in wireless communication. Albeit these higher frequency bands offer wide spectrum help improving the spectral efficiency, it comes with the challenge of alleviating the severe attenuation.

MmWave transceivers use large antenna arrays to form high-directional beams and overcome severe attenuation. A large array size leads to a costly beam alignment process if no prior information about beam directions is available. Beam alignment has two phases: beam discovery, and beam tracking. Beam discovery is finding the beam direction by consuming several pilot symbols to find the optimum direction. Moreover, beam tracking is a common approach to keep the discovered beams tightly coupled without frequent beam discovery to eliminate the overhead associated with realignment. Both phases become more difficult as the beams get narrower since slight mismatches lead to significant degradation in SNR as the beam coherence times are short. As a result, beams may lose alignment before they can be readjusted periodically with the aid of pilot signals. In this thesis, we introduce two complementary proposals. The first proposal is for the issue of beam tracking, and the second proposal is for the issue of beam discovery.

In the first part of the thesis, we propose a model where the receiver adjusts beam direction continuously over each physical-layer sample according to a carefully calculated estimate of the continuous variation of the beams. Our approach contrasts the classical methods, which fix the beams in the same direction between pilots. In our approach, the change of direction is configured using the estimate of variation rate via two different methods; a Continuous-Discrete Kalman filter and an MMSE of a first-order approximation of the variation. Our method incurs no additional overhead in pilots, yet, the performance of beam tracking and the resulting effective SNR are improved significantly. In addition, we propose a low-complexity discrete beam tracking algorithm that only requires a single pilot symbol with an angle of arrival (AoA) that lies in the main lobe of the beamforming. In typical situations, we achieve up to 4 dB enhancement in SNR and can reach 7 dB for large array sizes. This gain is associated with our algorithm's average Mean Squared Error (MSE) reduction by up to 99.5%. Furthermore, we introduce an analytical method of choosing the Pilot Period to sustain reliable tracking for a desirable *Link Reestablishment Time* based on two definitions: (1) beam coherence and (2) outage probability. The numerical results reveal that the Continuous-Discrete algorithms reduce the pilot overhead by 60% and up to 87% while supporting 95% of the maximum achievable rate.

In the second part of the thesis, we present a novel beam direction discovery approach that utilizes beam pattern amplitudes and combines it with the phase information available for a quick estimate of the beam direction. The proposed approach surpasses the traditional approaches, which exhaustively search all possible directions or follow hierarchical beam-sweeping architecture by dividing the angular space into sectors. Our approach minimizes the signaling overhead by estimating the beam direction in a single measurement in most instances instead of a number of measurements proportional to the array size as in traditional beam discovery approaches. Numerical results reveal a significant reduction of the pilot overhead by 42% and up to 62% compared to the state-of-the-art.

To my father's soul, Naguib Hussein Abdelrazek, who left this world during my Ph.D. study. My dear mother, Fatma, my beloved wife, Samar, my daughter Rouqaya, and my sons, Hamza and Yahya.

ACKNOWLEDGMENTS

I am praising Allah for helping me to accomplish this work. I will always be indebted to my advisor Prof. C. Emre Koksal, for sharing his knowledge, expertise, resources, and precious time through the growth of this work. My gratitude for his patience, devotion, and exemplary attitude in teaching, advising, and guiding research can only be experienced, not expressed.

I wish to express my heartfelt thankfulness to my committee members: Prof. Eylem Ekici and Prof. Abhishek Gupta. I am grateful for having a valuable discussion with Prof. Eylem Ekici during my candidacy exam. Also, I sincerely appreciate Prof. Abhishek Gupta for joining the committee for my qualifying and candidacy exams and for genuinely benefiting from his teaching of the course "Optimization for Static and Dynamic Systems."

I would also like to thank my friend Dr. Yahia Shabara for his support and fruitful discussions during our weekly meetings, which reflected positively on my research and learning experience.

I am very grateful to be a member of the Information Processing Laboratory (IPS) and to all faculty and staff, especially Patricia Toothman, who always provides help, friends, and colleagues at the ECE department, at OSU.

I truly appreciate the gracious and endless support of my great country, Egypt, not merely during my Ph.D. fellowship but also through my educational and professional career. Finally, I thank my family for their love, understanding, and support.

VITA

January 30, 1989	Born - Sharkia, Egypt
July 2012	B.S. Electrical Engineering, Military Technical College, Cairo, Egypt.
August 2018	M.S. Electrical Engineering, Military Technical College, Cairo, Egypt.
2013 - 2020	Graduate Teaching and Research Associate, Military Technical College, Cairo, Egypt.

PUBLICATIONS

Mohamed Naguib, Yahia Shabara, and C. Emre Koksal, ”Continuous-Discrete Analog Beam Tracking for Large-Scale MIMO Systems,” 2022 56th Asilomar Conference on Signals, Systems, and Computers, 2022.

Mohamed Naguib, Yahia Shabara, and C. Emre Koksal, ”Continuous Beam Alignment for Mobile MIMO,” Submitted to IEEE Tansactions on Wireless Communications.

Mohamed Naguib, Yahia Shabara, and C. Emre Koksal, ”High-Resolution Fast Analog Beam Discovery,” to be submitted to IEEE Tansactions on Wireless Communications

FIELDS OF STUDY

Major Field: Electrical and Computer Engineering

Specialization: Wireless Communication Networks

TABLE OF CONTENTS

LIST OF FIGURES

CHAPTER 1

INTRODUCTION

Wireless network generations constantly embrace more new bands on the higher side of the spectrum, such as millimeter-wave (mmWave) bands for 5G-NR, and even tap into the Sub-Terahertz (Sub-THz) bands for 6G [1–3]. The endorsement of a higher spectrum band alleviates the spectrum crunch, but it accompanies the challenge of dealing with the related drastic path loss [4, 5]. Employing large-scale Multiple Input Multiple Output (MIMO) communication systems with enormous antenna directional gain ameliorates the significant attenuation in the high-frequency bands.

In MIMO systems, transceiver architectures are divided into three categories: (1) Fully digital, (2) Hybrid, and (3) Analog architecture. The fully-digital architectures can be visualized as N parallel analog transceivers. Each consists of a single antenna element connected in serial to an RF chain, ADC/DAC, mixer, filter, and other components. Nevertheless, The electronic components operating in high-frequency are expensive and have significant power consumption [6]. Thus, a fully-digital transceiver that deploys a large-scale antenna array is costly and induces power consumption problems. Thus, mmWave systems look for cheaper and more power-efficient transceiver architectures. In addition, fully-digital transceivers are only one of the options to achieve the channel capacity because of the sparsity of the mmWave channel (i.e., it has a few channel paths) [7–9]. The hybrid architecture is less complex and cheaper than the fully-digital ones, where multiple RF chains (i.e., more than one and less than the array size) are connected to all antenna elements in different configurations. Finally, the analog transceiver has a single RF chain, ADC/DAC, and is connected to all antenna elements through phase shifters [10–12]. Although the analog architectures are much cheaper with the lowest power consumption, the resolvability of the incoming path is minimal due to the summation of channel response from all different directions.

Nevertheless, narrow beams resulting from the transmitter (TX) must be aligned with their counterparts at the receiver (RX) to get the potential gain. The challenge is that aligning such narrow beams mandates significant overhead, especially under analog transceiver architectures. Still, the alignment of such narrow beams can be momentary since narrow beams have a short coherence time which means the aligned beams become misaligned in a short time, then, the previously chosen TX and RX beams are no longer valid, and realignment is required. Among other factors, misalignment can be induced by TX/RX mobility, and these variations rapidly degrade the Received Signal Strength (RSS) [13]. The alignment process can be separated into two stages: (i) *Beam Discovery / Initial Beam Alignment* and (ii) *Beam Tracking*. Next, we will elaborate on both stages in detail.

Initial beam alignment: Represent discovering the Angle of Arrival (AoA) / Angle of Departure (AoD) at the establishment of a communication session and on the occasion of beam failure (i.e., when losing beam alignment, e.g., due to blockage). Beam discovery is challenging, mainly when analog transceiver architectures are utilized, because channel measurements have to be acquired one by one, which extends this process. Large-scale antenna arrays are notably susceptible to this problem since the corresponding narrow beams enlarge the number of beam pairs to choose from. Exhaustive search or beam sweeping, whose computational complexity is $O(N_t \times N_r)$, where N_t and N_r stand for TX and RX array sizes, respectively, is an example of the initial beam alignment stage. Derivatives of the traditional beam sweeping with hierarchical designs and less complexity are embraced in WiFi standards and 5G-NR [14, 15]. Other proposals benefit from the channel sparsity property in the mmWave band and have been shown to have complexity in order of $O(k^2 \log(N_t/k) \log(N_r/k))$ (for channels with k paths) [16].

Beam Tracking: In rapid-variation environments, repeatedly probing for beam directions is not optimum due to the significant overhead that would be required. Instead, a more efficient method is to prolong the link reestablishment time (T_{LR}, the time between each beam discovery) by tracking the previously found beam(s) for as long as achievable. This can be accomplished by frequently transmitting reference (pilot) signals to watch minor beam variations. Nevertheless, those reference symbols still comprise an overhead which should be diminished to avert degrading the functional spectral efficiency [17]. A trade-off declares itself where more frequent pilot symbols reveal better beam tracking performance but at a higher overhead cost. On the other hand, less frequent pilots would lead to beam misalignment, which degrades the average received SNR and risks beam alignment failure (i.e., losing alignment). In that case, a recurrence of the costly initial beam alignment procedure would be required.

Contribution of this thesis: In Chapter 5, we introduce a beam tracking approach that continuously corrects the antenna beam direction, even though the available channel measurements are sparse, through the transmission of pilot symbols. In contrast to traditional beam tracking approaches, which update the estimate of beam directions based on pilot symbols and fix them till the arrival of the following pilot symbols, our approach models and utilizes gradual beam variations in between pilot symbols by estimating the beam direction variations at the transmitter and the receiver. Our proposal, which we denote as Continuous-Discrete tracking, exploits the physical nature of beam direction variation in the spatial domain as a time-varying function to build a state transition model. This model fuses information with channel measurements under three different frameworks: (i) an Extended Kalman Filter (EKF), (ii) a Fast Beam Tracking algorithm (iii) a Main-Lobe approximation.

We discuss the three frameworks in detail in Chapter 5. The proposed Continuous-Discrete method enables our solution to rely on less frequent pilot symbols to maintain precise beam tracking. Reducing the number of channel measurements decreases the overhead of pilot symbols needed to perform such measurements. Our proposal (i) enhances the quality of beam alignment over the state-of-the-art approaches under the same pilot overhead, (ii) elongates the link reestablishment time before a new beam realignment would be required, and (iii) reduces the associated pilot overhead mandated to achieve tracking performance similar to the state-of-the-art solutions.

A novel beam discovery approach is proposed in Chapter 6, which leverages both the amplitude and the phase information of the received signal to precisely estimate the beam direction. Contrary to classical beam discovery approaches, which primarily measure all or a sector of the angular domain by narrow beams to detect the beam direction based on the highest RSS, our model utilizes both the amplitude and the phase to minimize the accompanying overheads. Our proposal, which we refer to as Main-Lobe Fast Beam Discovery (ML-FBD), exploits the innovative formula from [18]. This formula is an analytically tractable mapping function from the beam direction to the beam amplitude. The proposed approach is discussed in detail in Chapter 6. Our proposed solution ML-FBD relies on a lower number of channel measurements to preserve accurate beam discovery. Decreasing the number of channel measurements reduces the overhead of pilot symbols required to gather such measurements.

In this work, we first introduce the solution to the beam tracking problem then we present the beam discovery solution since the first is complementary to any beam discovery solution. The two main contributions of this work include:

- A continuous-discrete beam tracking that continuously predicts the beam direction, even though the channel measurements are sparse, via the transmission of pilot symbols. Low-complexity implementation of the idea can be realized via low-complexity control-theory tools.
- A beam discovery approach to quickly narrow down the search in 1-2 shots to the correct beam direction among hundreds of possibilities.

Following this introduction, Chapter 2 gives an overview of the mmWave system, and we discuss the related work in Chapter 3. Furthermore, the system model is introduced in Chapter 4. Chapter 5 demonstrates the Continuous-Discrete beam tracking approaches, and Chapter 6 illustrates the Main-Lobe Fast Beam Discovery approach. Finally, Chapter 7 concludes our work and introduces future work.

CHAPTER 2

MILLIMETER WAVE OVERVIEW

2.1 Introduction

In this chapter, we briefly discuss millimeter wave history, how it became an enabling technology to the most advanced cellular networks and why we need mmWave in wireless communication networks. Moreover, the mmWave propagation characteristics differ from the traditional wireless network systems and add more challenges to the developers and manufacturers, and we are going to summarize these characteristics. Furthermore, we introduce the hidden advantage of the mmWave, designing and manufacturing large-scale antenna arrays in tiny spaces. Finally, utilizing large-scale arrays add more challenges to wireless networks, such as the problem we discuss in this study.

2.2 Road to mmWave

Adopting the millimeter wave (mmWave) in wireless communication systems denotes a recent step in the row of evolution that started more than a century. Starting with Guglielmo Marconi, who was the first to develop and commercialize a wireless telegraphy system, the wireless communication systems industry has extended from Point-to-Point (P2P) topology to Radio Frequency (RF) broadcast systems and, Eventually, to cellular networks. Since more technological systems have developed, wireless communication has become ubiquitous the life. The modern community is gripped in wireless networking, as the majority use cellular networks, WiFi, and other topologies of wireless networking, all of which have evolved considerably over the past two decades. The phenomenal popularity of such technological systems drives designers of new devices, developers of its infrastructure, and manufacturers to search for a broader radio spectrum for better-advanced offerings constantly [19].

Wireless networks in the mmWave band represent the most contemporary development for wireless networking. The significance of mmWave will be caused by consumers seeking higher data transmission rates for real-time activities, which demand lower delays and stable links on wireless networks. The available spectrum at the mmWave band is superior to wireless systems (cellular and WLAN), which operate at frequencies below 10 GHz. Particularly the idle band of frequencies at 60 GHz affords 10x to 100x more available spectrum than the unlicensed spectrum in the Industrial, Scientific, and Medical (ISM) bands (e.g., WiFi users, 2.4 / 5 GHz) and cellular systems up to the 4th generation (i.e., 4G), which operate at frequencies below 6 GHz. The plenty of spectrum facilitates the achievement of higher data transmission rates for identical modulation approaches while supporting more sharable resources for multiple users.

2.3 Radio Wave Propagation for mmWave

The characteristics of radio wave propagation are vital to the design of the receiver, transmitting power, antenna design, interference level, and the expected coverage for wireless networks. At mmWave frequencies, the corresponding wavelengths are tiny, which means that most of the entities in the physical channel are very large relative to the mmWave wavelengths. Therefore, objects with large wavelengths compared to mmWave cause critical propagation phenomena, like signal blockage, when an obstacle blocks the path between the TX and the RX. Nevertheless, wireless links are still potentially established between the TX and RX by reflected and scattered waves, even if the line-of-sight (LOS) paths are blocked.

The mmWave band's wavelengths are so short that the molecular compositions of atmospheric molecules (i.e., water vapor) have a vital role in the achievable free space distances over the sub-terahertz (Sub-THz) spectrum. Fig. 2 depicts the overload attenuation (additional to the Friis distant-dependent path loss) in the air over the RF spectrum band up to 400 GHz and exhibits how electromagnetic waves are drastically attenuated by the absorption of the atmospheric molecules, which is happened due to the oxygen and the water molecules at 60 GHz, and 180 - 320 GHz respectively [20]. In addition, temperature and humidity strongly affect the actual extra attenuation induced by absorption [21]. Also, Fig. 2.1 shows that specific spectrum bands, e.g., 60 GHz, 180 GHz, and 380 GHz bands, have a significant extra attenuation over distance. These spectrum bands are suitable for unlicensed networks for homes and buildings (within a coverage distance of tens of meters) where the radiated signals propagated through space will rapidly attenuate and avoid interference with nearby networks. Fortunately, spectrum bands ranging from 0 to 50 GHz, or 200 to 280 GHz, are potent candidates for cellular networks and mobile systems since they have little excess atmospheric attenuation. This happens since the smaller the attenuation, the better the coverage distances, which is more suitable for cellular systems. Atmospheric attenuation, among other factors, impact coverage distances or interference due to co-channel transceivers. Also, weather conditions (e.g., rain, hail, sleet, or snow) significantly impact frequency-dependent attenuation over distance.

Large-Scale Propagation Channel Effects: Electromagnetic wave propagation in free space is a reasonable starting point for assessing the aspects of the wireless

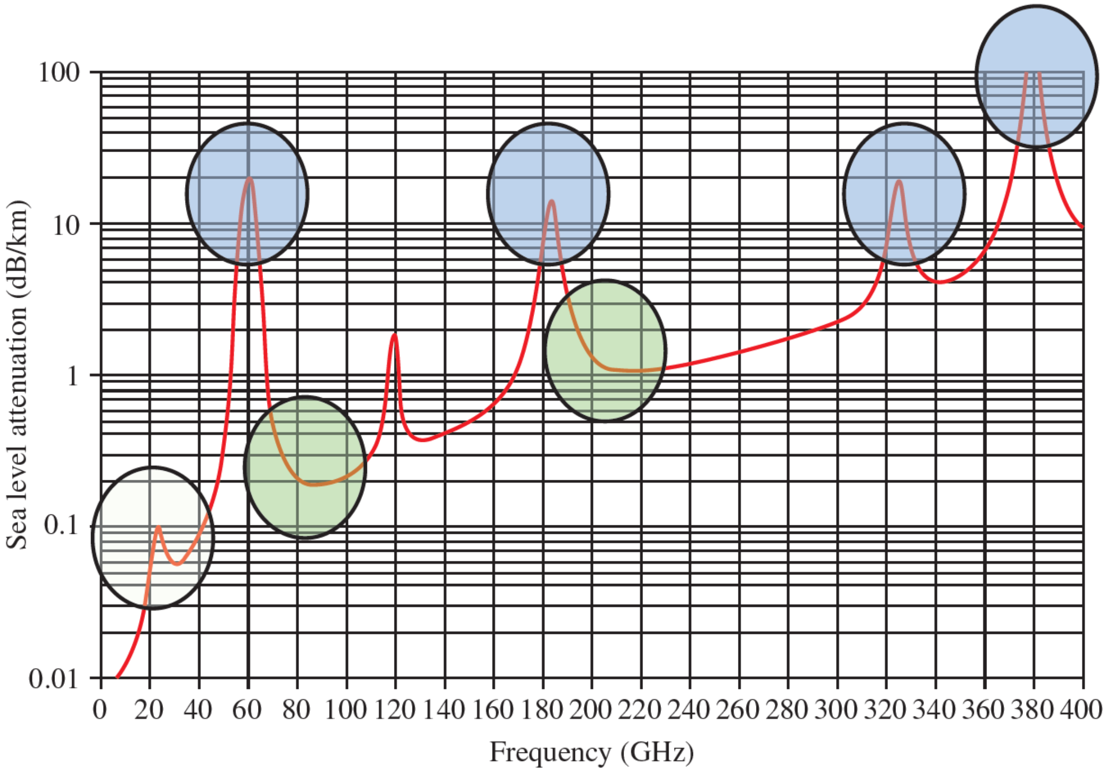

Figure 2.1: The associated attenuation (dB/Km) with absorption in the air that is over free space path loss [20].

channel on a large scale, where the signal power loss is characterized by different orders of magnitude variations in separation between the transmission parties (i.e., transmitter/receiver), up to thousands of meters. The free space propagation with a clear channel (no obstacles, scatterers, or reflectors) is modeled mathematically in the equation of free space path loss attributed to H.T. Friis [22]. In [23], the Friis equation describes how to relate the Effective Isotropic Radiated Power (EIRP) at the RX as a function of the TX power P_t, and the antenna gains G_t, G_r at the TX and the RX, respectively. The free space path loss equation (Friis equation) is given by:

$$P_r = \frac{P_t G_t G_r}{L} \left(\frac{\lambda}{4\pi d} \right)^2 \tag{2.1}$$

where P_t and P_r are presented in units (Watts or milliwatts), while G_t and G_r are linear (not dB) gains, respectively, compared to an isotropic radiator, and $\lambda = c/f_c$ is the operating wavelength (in meters). Moreover, c is the speed of light, f_c is the carrier frequency, d is the separation between the transmitter and the receiver, and L is the path loss. It is clear from the equation that path loss increases as the wavelength are shortened, or the distance is increased. The relation between the wavelength and the frequency of the propagated signal makes it clear that the free space path loss is proportional to the square of the carrier frequency.

Simple calculations can reveal that adopting the mmWave bands will be a critical issue if omnidirectional antennas are deployed. We should compensate for 20-40 dB power loss compared to communication systems below 10 GHz. This severe path loss in the mmWave and Sub-THz has been approved with a bunch of measurement campaigns [24–26].

Free space path loss can work well for the mmWave channel when a LOS path exists and the directional antennas are perfectly aligned [26]. Thus, large-scale propagation effects should also consider, Atmospheric, weather effects, diffraction, reflection, penetration, and scattering.

Small-Scale Channel Effects: The arrival of multipath in the wireless channel produces small-scale fading effects. The most important effects are:

- Rapid variations in signal strength over a short distance or time interval.
- Random modulation in the carrier frequency due to varying Doppler shifts on each incoming path.
- Time echoes produced by multipath propagation delays.

The complex coefficients of an incoming path from the multipath components integrate the large-scale path loss effects. Conceptually, the small-scale effects model the arrival of replicas of a transmitted signal due to scattering, reflection, or diffraction. Also, each multipath component may belong to a different angular direction (arrive from various spatial directions). Signals in the mmWave band also experience a considerable percentage of multipath contributions due to significant surface scattering (i.e., scattering from large objects). Objects comparable in dimension to the λ induce the scattering effect, acting as point sources if it blocks the path between the transmitter and the receiver. The mmWave channel is depicted by severe shadowing [24] since it experiences reduced diffraction. The reflection effect is derived by objects with dimensions much larger than the wavelength of the propagated signal. Thus, traditional scatterers (objects) now act as reflectors at the mmWave and Sub-THz bands and may derive considerable multipath impacts in mmWave systems.

2.4 Antenna Arrays

Up to this point, we discuss the issues with the propagation characteristics of the mmWave channel. However, due to its low wavelength, the mmWave band will allow small-dimension directional antennas with significant gain that can offset and even reduce the associated path loss. This is easily noticed in equation 2.1, where adaptive arrays may be utilized to produce narrow beams (with high directional gain) that are compact enough (physically small) at mmWave frequencies. This high directional gain is steerable that allow the mmWave system to guide beams within the channel and to bounce the propagated energy from the surrounding objects (scatterers and reflectors) while focusing the propagated energy in the strong directions that make a potential link for communication path. Moreover, by employing a mixture of MIMO and beamforming techniques, the severe path loss in the mmWave channel can be alleviated dramatically by forming concurrent beams in various directions. Also,

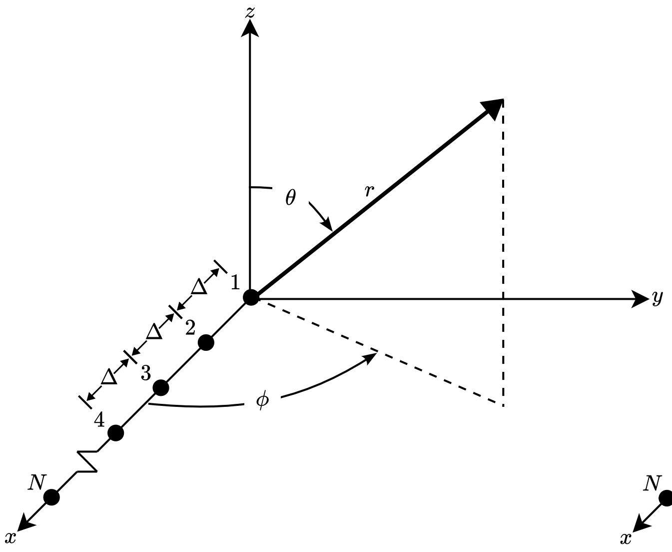

Figure 2.2: Uniform Linear Array with N elements [27]

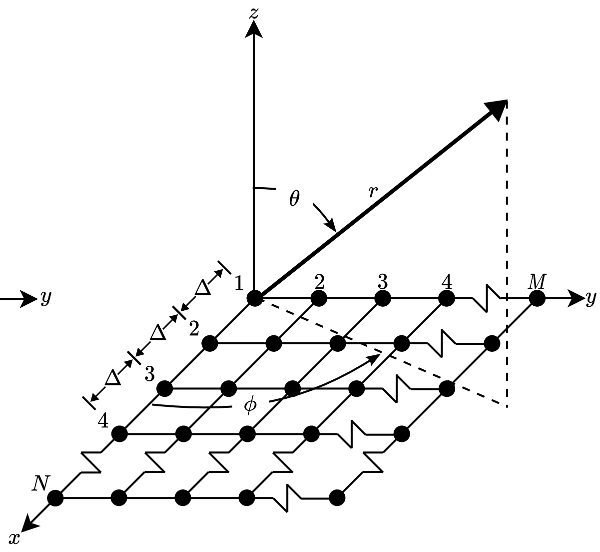

Figure 2.3: Uniform Planar Array with NxM elements [27]

different spatial paths can be utilized to leverage MIMO and spatial multiplexing, where parallel data streams are transferred to increase capacity.

Antenna arrays come with several advantages compared to solo antenna systems, where it may be essential to satisfy link budget requirements when the operating frequency is beyond 10 GHz. Besides improving the antenna gain, such an array can enhance the receiver sensitivity by $10\log(N)$, where N is the array size [28]. This means a system with N antenna elements improves the Signal-to-Noise Ratio (SNR) with N times compared to a single-element system (when $N = 1$). Moreover, an array approach enhances resiliency to robust unwanted signals that may interfere with or obstruct the desired signal, provided these signals impinges from directions other than the desired beam direction.

Array Configuration: The array can take different configurations describing how the elements are equipped and placed to form the array. The geometrical shape of the elements denotes the array configurations as follows: linear, rectangular (planar),

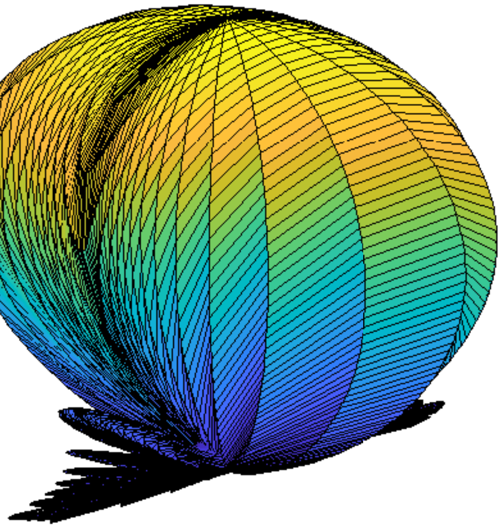

Figure 2.4: A 3D view of the ULA directional gain.

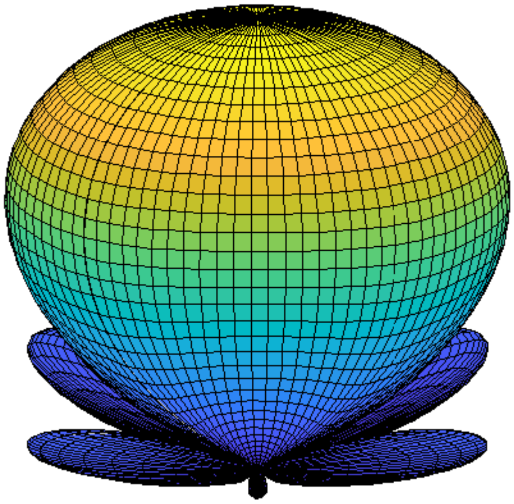

Figure 2.5: A 3D view of the UPA directional gain.

circular, and spherical. Here, we briefly describe linear and planar arrays, while the remaining configurations are out of our scope. We depict the linear and planar configurations in Fig. 2.2 and Fig. 2.3, respectively. We depict the linear and planar configurations in Fig. 2.2 and Fig. 2.3, respectively. As shown in Fig. 2.2, the elements are distributed over a line and spaced by Δ in wavelength (e.g., 0.5λ). When the antenna elements are organized over a rectangle, we denote it by a planar array. Furthermore, an array is classified as (i) uniform and (ii) non-uniform array based on the spacing between elements. Therefore, we can have Uniform Linear Array (ULA) and Uniform Planar Array (UPA) when the array elements are equally spaced in any direction.

The elements of the array can be phased by applying a phase shift to each element to form and steer the beam (directional gain). The beamforming (directional) gain for the ULA ($N = 16$ elements) and UPA (square, with $N = M = 4$, i.e., 16 elements as well) are shown in Figs. 2.4 and 2.5, respectively. Both configurations have the

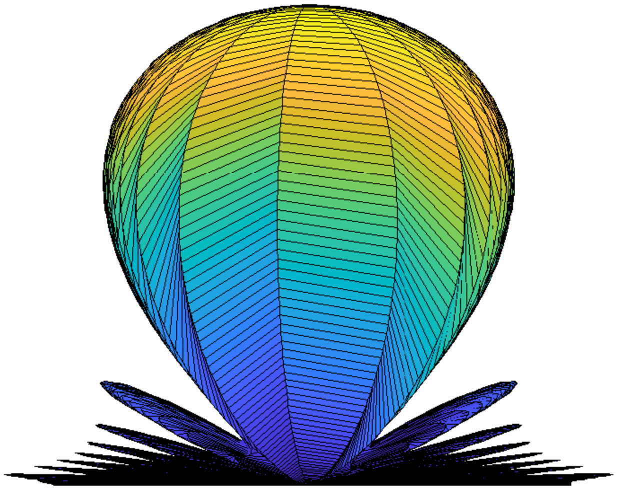

Figure 2.6: X-Z (azimuths) plane for ULA pattern

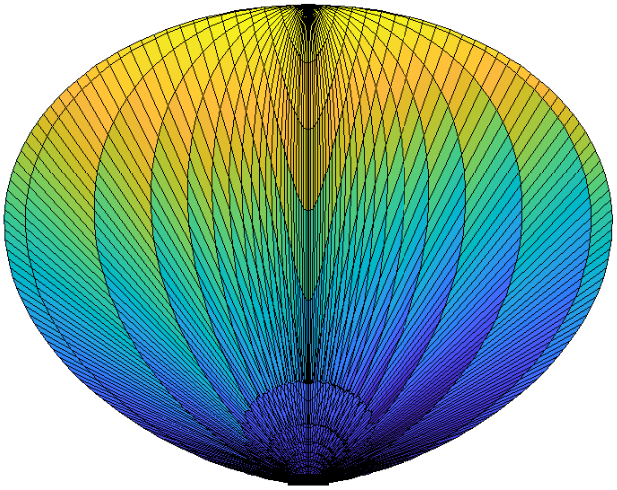

Figure 2.7: Y-Z (elevation) plane for ULA pattern

same gain since they have equal array sizes. Nevertheless, they have different spatial properties. ULA has a narrower beam in the azimuthal plane and a much broader beam in the elevational plane, as shown in Figs. 2.6 and 2.7. On the other hand, Figs. 2.8 and 2.9, a square UPA has a symmetric beam width in both the azimuthal and elevational planes. We can notice that the ULA has a narrower beamwidth than the UPA, especially in the azimuthal plane, which makes it a better candidate for interference cancellation issues. On the other hand, the symmetric and broader beams of the UPA compared to the ULA give the advantage to the UPA when talking about beam alignment.

2.5 Summary

This chapter introduces the mmWave network's history and discusses how the propagation at high-frequency bands (mmWave and Sub-THz) is highly attenuated. Also, we discuss the hidden advantage of the mmWave system, which enables us

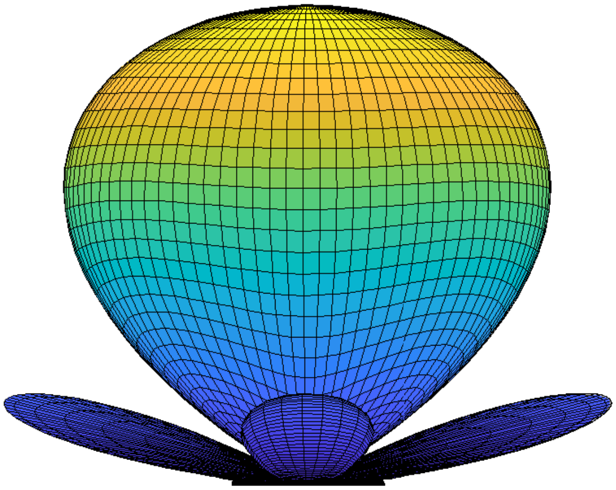

Figure 2.8: X-Z (azimuths) plane for UPA pattern

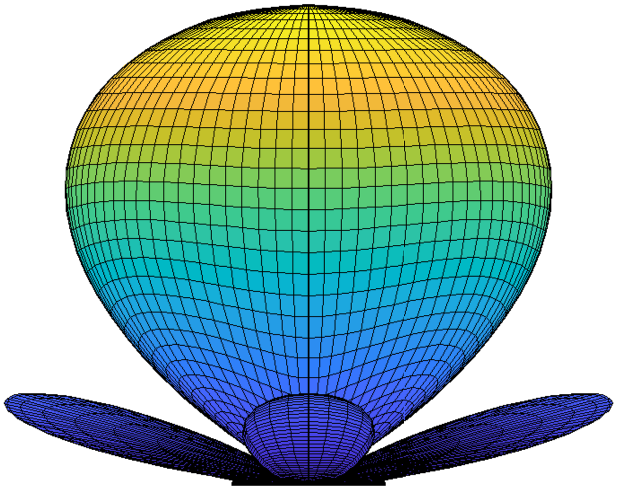

Figure 2.9: Y-Z (elevation) plane for UPA pattern

to reach large-scale antenna arrays in the size of portable devices. Moreover, the large-scale arrays provide high directional gains, compensating for the severe path loss for wireless networks beyond 10 GHz. Finally, utilizing large-scale arrays with narrow directional gains comes with additional beam alignment costs. In Chapter 3, we discuss in detail the problem of beam alignment and how it was handled in the related work.

CHAPTER 3

RELATED WORK

3.1 Introduction

Beam management is open research, especially since mmWave networks had a significant role in the latest wireless networks as 5G/6G. For example, 5G mmWave bands, typically known as Frequency Range 2 (i.e., 24.25 to 52.6 GHz), count on a beam-based air interface instead of a sector-based air interface as in the low-frequency bands [15]. This chapter introduces some related work to the beam management problem. We consider the two main classifications of the beam alignment issue: (i) Initial Beam Alignment (Beam Discovery) and (ii) Beam Tracking.

3.2 Initial Beam Alignment

Beam discovery is the initial stage of beam management, contributing significantly to the link establishment of mmWave networks. Typically, beam discovery is conducted via a sequence of pilot symbols for beam training before data transmission, and this represents an overhead that exacerbates the spectral efficiency in large-scale MIMO systems [29]. This issue has been tackled through several methods, including (1) *Compressed Sensing* (CS), which has long been used for efficiently reconstructing signals [30, 31]. Due to the mmWave channel sparsity, we can exploit CS tools to acquire the beam directions (AoA/AoD). The adaptation of CS tools to the beam discovery problem depends on random beamforming vectors, mainly constructed by assigning each antenna element a random phase shift. The random phase shifts integrated into the beamforming and precoding vectors develop irregular envelopes of beam patterns, which are susceptible to signal power variations and thermal noise [32]. Also, beam discovery methods include (2) *Beam Sweeping* or *Exhaustive Search* [14,29], where the TX and RX examine all potential beam pairs from a predefined set of beamforming/precoding vectors. The beam direction can then be estimated from the accrued information of path gains and their corresponding AoAs/AoDs. The *Exhaustive Search* is time-consuming where the beam discovery complexity is $O(N_t \times N_r)$. So, the time needed to find the optimum pair of beams at the TX and RX scales in quadratic form when $N_t = N_r = N$.

Many approaches have been proposed to scale down the complexity of beam sweeping. A big step is decoupling the beam discovery from the TX and the RX as follows: First, TX exploits a quasi-omnidirectional beam, while the RX utilizes a narrow beam to discover the optimum AoA direction. Second, the first step is reversed so that the TX also discovers the AoD direction [14]. The second big step is the utilization of a hierarchical beam sweeping approaches [10, 33–39], which studies the design of adaptive beamwidth codebooks to decrease the beam discovery complexity and its associated overhead.

The basic idea of these approaches is to utilize coarse and fine beam sweeping stages. In [33], a K stages hierarchical beam sweeping approach is proposed to minimize the number of channel measurements. This approach uses a set of beamforming vectors corresponding to wide beam patterns to scan the angular space at the first stage. In the second stage, the same beamforming vectors are utilized but now correspond to narrower beam patterns. The chosen vectors at stage two cover a sector of the angular space that conforms to the same direction of the beamforming vector with the highest RSS. Similar stages with narrower beam patterns are utilized to precisely estimate the beam direction that maximizes the SNR.

As a practical implementation of the hierarchical beam sweeping, the IEEE 802.11 ad/ay WiFi specifications [35,36] utilize two-stage of coarse and fine beam sweeping. In addition to decoupling the discovery problem between the TX and the RX, [35,36] construct wide beams to cover the angular space as sectors, then scan the sector with high potential using very narrow beams. In [34], a design of MAC scheme is proposed in light of maximizing the spectral efficiency. The basic idea is to reduce the reference (pilot) symbols overhead required for beam training/discovery and tracking. They exploit a hierarchical beam sweeping similar to the IEEE 802.11 ad/ay [35,36]. Furthermore, the 5G-NR standards [15] deploy two-stage coarse-fine beam sweeping. In contrast to beam sweeping, the problem of finding the beam direction is formalized as a Multi-Armed Bandit [13]. In comparison to the WIFI standards [35,36], the approach used in [13] utilizes the contextual information from previous beam alignments is used to minimize pilot overhead.

The works mentioned above consider the beam discovery over an analog beamforming architecture. Nevertheless, many beam discovery methods exist that deploy different architectures, i.e., Hybrid/Digital. [40–50] proposed a two-level phased array architecture (Hybrid) with M subarrays and M RF chains. This work can be described as follows: (1) the first level is the analog domain part, where each subarray constructs a wide beam pattern, and all the subarrays direct their beam toward the same direction. (2) the second level is virtual, where the digital beamformer creates virtual narrow beams directed in all directions. The combined beam is the product of the two-level beams and has the resolution of the narrow beams (virtual level). In similar works, where subarray based approaches are utilized to minimize the pilot symbols overhead, phased subarrays are deployed in two configurations: (1) overlapped [41] and (2) non-overlapped [42]. A cross-correlation beam discovery approach that deploys subarrays is proposed in [42–44], and subspace projection beam search algorithms are presented in [45, 46] when the same phase shift is utilized for each subarray. In [42, 46], additional pilot symbols are employed to resolve the ambiguity in detecting beam direction. Also, a frequency domain post-processing is required for [43], while a noise subspace projection is needed for [45], and iterative updates are necessary for [47, 48]. Moreover, exploiting different phase-shift for each subarray is helpful in reducing the beam discovery latency, which was proposed by [49–51]. This work shows a significant reduction in the number of channel measurements. Still, it has the complexity of the hybrid beamforming architecture, which scales up with the number of RF chains. In this work, we are only interested in beam discovery on systems utilizing analog beamforming architectures.

3.3 Beam Tracking

Beam tracking is a complementary solution to the initial beam alignment solution, which aims to keep the beam alignment tightly coupled while reducing the significant overhead required by initial beam alignment. This can be done by enlarging the time in-between two consecutive beam discoveries. Many algorithms have been proposed for *beam tracking*, with the motivation of using a small number of overhead pilots to track the already discovered beams.

Extended Kalman Filter: The EKF is a non-linear version of the Kalman Filter, where the tracked/predicted object is non-linearly added to the noise. Therefore, the EKF is a suitable solution for tracking the AoA/AoD where the thermal noise is added to the AoA/AoD in a non-linear fashion at the antenna elements. Discrete Extended Kalman Filter (EKF_D) was proposed in [52] as a low-complexity tracking algorithm, utilizing a periodic single pilot symbol each time slot to find a new estimate. In [52], the EKF complements an initial estimate of the AoA/AoD, which means they only consider the beam tracking problem without considering the initial beam alignment problem.

Fast Beam Tracking: In [53], a Fast Beam Tracking (FBT_D) approach was developed to make the MSE converge faster to the Cramér-Rao lower bound (CRLB). In this approach, both the initial beam discovery and the beam tracking problems are considered. A coarse beam sweeping is proposed to discover the initial beam direction, and a recursive beam tracking algorithm is proposed to minimize the MSE of the true AoA.

Auxiliary Particle Filter: Another tracking algorithm that handles the non-linear noisy function of the AoA is proposed in [54]. In this approach, a group of particles are generated at each channel measurement. An estimate of the AoA is found by averaging the estimate of all generated particles.

These approaches update the beams at discrete instances upon fresh measurements and keep the alignment fixed until the subsequent measurement. In contrast, our approach updates the beam directions incrementally in between measurements. Moreover, [55] proposed a CS framework that probes the channel and steers the beam direction per each OFDM symbol to gather more random probing directions to increase the randomness in the sensing matrix compared to traditional beam switching per block of symbols [56]. Symbol-based beam direction switching approach is supported by several previous works that enable the beam switching time in terms of 4 to 50 ns for mmWave [57, 58] and could be reduced as low as 100 ps [59].

Up to this point, we have introduced some beam tracking algorithms that utilize pilot symbols to perform tracking. On the other hand, other techniques exploit different resources to track the beam direction. Previous works leverage Machine

Learning (ML), computer vision, and radar sensory information to enhance beam tracking and blockage prediction in mmWave and Sub-THz bands [60–65].

Vision-aided frameworks were proposed to predict the blockage and position of a mobile user/terminal to complete handoff [62–64]. Furthermore, in [60], an ML framework was proposed to reduce the dependence of beam tracking on pilot symbols. In this approach, an RGB camera is attached to the Base Station (BS) to capture a group of consecutive images. An object detector is utilized to process the captured images and identify the receiver position. An algorithm then predicts the future position of the receiver and its corresponding beam direction. In this study, we do not assume the presence of aiding devices like cameras, and we are only concerned with beam tracking techniques that utilize a single pilot symbol arriving at each time slot. In [61], a deep learning framework exploits the sub- 6 GHz channel holds sufficient information to predict the beam direction and blockage status in the mmWave channel. In addition to radar sensory information, the geographical location of the user/terminal used to conduct the beam tracking procedure is proposed in [65].

CHAPTER 4

SYSTEM MODEL

In this chapter, we present the system model used to solve both the problems of beam discovery and tracking. The proposed model is general for both problems, but certain assumptions are assumed for the number of antenna elements utilized and the channel variations. Following this brief introduction, we introduce the notations in Section 4.1, and the channel model is described in Section 4.2. Finally, Section 4.3 introduces the communication protocol, which describes the beam discovery and tracking issues and shows the crucial role of these issues in accomplishing data transmission.

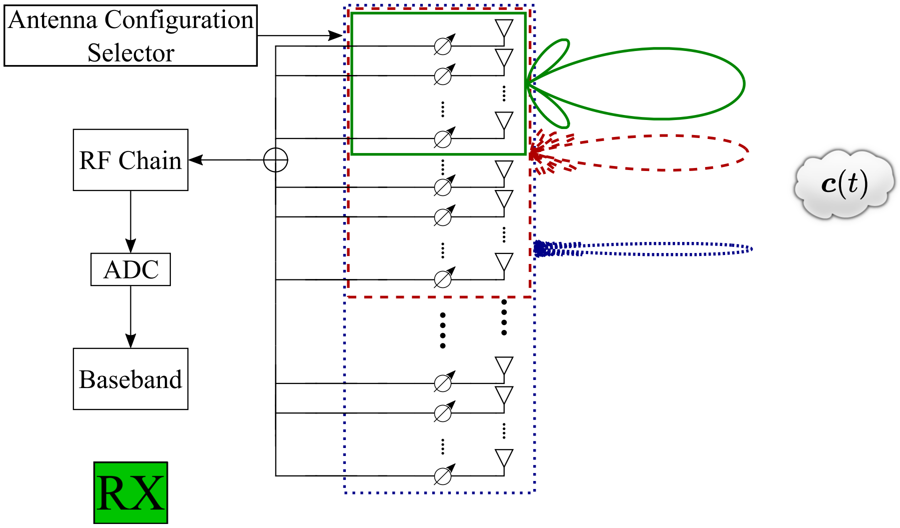

Figure 4.1: Receiver architecture with M subarrays

4.1 Notation

The lowercase x and $\boldsymbol{x}$ denote scalar and vector quantities respectively, while the uppercase $\boldsymbol{X}$ denotes a matrix. The continuous variation in $\boldsymbol{x}$ is denoted by $\boldsymbol{x}(t)$, and $\boldsymbol{x}_k$ is the sampled version of $\boldsymbol{x}(t)$ each T seconds, where $\boldsymbol{x}_k \triangleq \boldsymbol{x}(t)\,|_{t=kT}$. Moreover, $(.)^\dagger$, $\Re(.)$ and $\Im(.)$ denote the conjugate transpose, the real and the imaginary parts respectively. Also, The standard Q function is denoted by $\mathbb{Q}$, while its inverse is denoted by $\mathbb{Q}^{-1}$. Finally, $|\mathcal{S}|$ is the cardinality of a set $\mathcal{S}$.

4.2 Channel Model

We consider a Single Input Multiple Output (SIMO) channel model with a single antenna at the transmitter and N antennas at the receiver as shown in Fig. 4.1. The receiver antennas are equally spaced and arranged linearly to form a Uniform Linear Array (ULA). We assume an analog beamforming transceiver architecture, where a single RF chain is utilized, and a phase shifter is applied for each antenna element in the array. We assume a 2D multi-path channel model from [6, 18, 66] with a channel impulse response:

$$\boldsymbol{c}(t) = \sum_{\ell=1}^{L} \alpha_\ell(t)\, \boldsymbol{a}_R\left(\phi_\ell(t)\right), \tag{4.1}$$

where ℓ is the path index, L is the total number of paths, $\alpha_\ell(t)$ is the complex path gain, $\boldsymbol{a}_R$ is the array steering vector, and $\phi_\ell(t)$ is the time-varying AoA, which changes over time due to mobility of the transmitter, receiver and the environment. The steering vector is given by:

$$\boldsymbol{a}_R(\phi) = \left[1\ e^{-j2\pi\Delta\cos(\phi)}\ \ \dots\ e^{-j2\pi\Delta(N-1)\cos(\phi)}\right]^T, \tag{4.2}$$

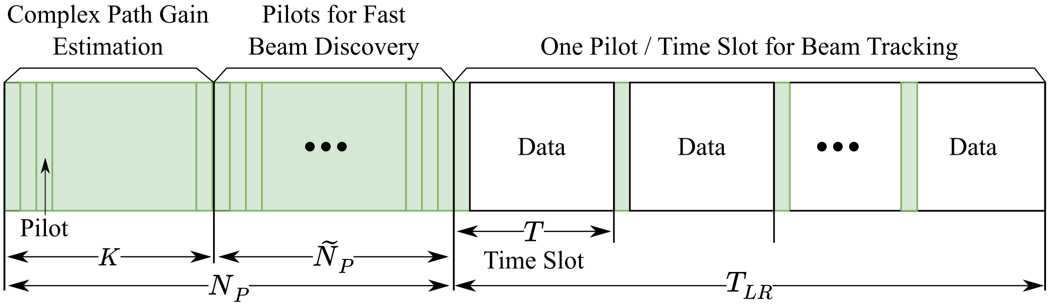

Figure 4.2: Frame Structure of Beam Alignment Procedure.

where $\phi \in [0\,,2\pi)$, Δ is the antenna spacing normalized by the wavelength, and N is the number of array elements.

Fig. 4.1 depicts the analog beamforming architecture with N antenna elements. This antenna array is virtually divided into M subarrays, where each subarray has $N_o = \dfrac{N}{M}$ antenna elements. The receiver can utilize any combination of adjacent subarrays to increase the received array gain. Simply, exploiting a single subarray results in a wide beam with low array gain. Increasing the number of combined subarrays makes the beam narrower with higher array gain.

4.3 Communication Protocol

This section discusses the frame structure representing the presumed communication protocol. The frame structure given in Fig. 4.2 is used in [18, 66] to describe the beam alignment procedure. We have two main stages for beam alignment: the first stage consists of N_P pilots required for beam discovery (*initial beam alignment*), and the second stage applies one pilot each time slot for *beam tracking*. Chapter 6 focuses on the first stage, which treats the initial beam discovery. The second stage is considered in Chapter 5. The following Sections 4.3.1 and 4.3.2 provide the specific assumptions for each stage.

4.3.1 Beam Discovery

In this stage, we assume that the receiver can exploit any combination of the subarrays to produce different beams with different widths. This stage is divided into two substages: (1) Complex path gain estimation and (2) Beam direction estimation. For the complex path gain estimation, we consume K pilot symbols to find an estimate of the path gain. Then, $\widetilde{N}_P$ pilot symbols are utilized to find an estimate for the beam direction given the path estimate in the first stage. Through both substages, we assume the beam direction to be almost constant during the beam discovery period, then the channel model in Eq. (4.1) is reduced to the following:

$$\boldsymbol{c} = \sum_{\ell=1}^{L} \alpha_\ell \boldsymbol{a}_R\left(\phi_\ell\right), \tag{4.3}$$

Given the sparse nature of the mmWave channel, the received power from all directions is limited to a few sharply defined AoAs [3, 67]. In addition, since our receiver has an analog architecture, it can only form one directional beam towards the strongest path in the channel (i.e., the path with the highest received power). Hence, we can assume that all other paths are highly attenuated since they are weaker and lie outside the main lobe of the receive antenna. Therefore, we omit the subscript ℓ for paths and treat attenuated weaker paths as noise.

We utilize a sequence of pilot symbols to measure the channel and thus estimate the AoA. The k^{th} received pilot sample is given by:

$$\begin{aligned} z_k &= \alpha\, p\, \boldsymbol{w}^\dagger(\bar{\phi}_k)\, \boldsymbol{a}_R\left(\phi\right) + n_k \\ &= \frac{\alpha\, p}{\sqrt{N}} \sum_{m=0}^{N-1} e^{-j2\pi\Delta m[\cos(\phi)-\cos(\bar{\phi}_k)]} + n_k, \end{aligned} \tag{4.4}$$

where p is the amplitude for a known pilot symbol, $\bar{\phi}_k$ is the beam pointing direction utilized at each pilot symbol, $n_k \sim \mathbb{C}\mathcal{N}(0, \sigma_n^2)$ is a circularly symmetric complex Gaussian noise sample, and $\boldsymbol{w}(\bar{\phi}) \in \mathbb{C}^{N\times 1}$ is the beamforming vector which is given by:

$$\boldsymbol{w}(\bar{\phi}) = \frac{1}{\sqrt{N}}\Big[1 \; e^{-j2\pi\Delta\cos(\bar{\phi})} \; \ldots \; e^{-j2\pi\Delta(N-1)\cos(\bar{\phi})}\Big]^T \tag{4.5}$$

Succinctly, we can rewrite Eq. (4.4) normalized as follows:

$$y_k = \frac{\alpha}{N}\sum_{m=0}^{N-1} e^{-j2\pi\Delta m[\cos(\phi)-\cos(\bar{\phi})]} + \acute{n}_k, \tag{4.6}$$

where $\acute{n}_k \sim \mathbb{C}\mathcal{N}(0, 1/\rho)$, $\rho = N\rho_a$ is the SNR including the array gain, and $\rho_a = |p|^2/\sigma_v^2$ is SNR for each antenna element.

4.3.2 Beam Tracking

In this stage, we assume that the receiver utilizes the total array size, which means the receiver produces the beam with beamwidth corresponding to the full array size. Moreover, the continuous variation in the AoA is given by:

$$\begin{aligned} \phi_\ell(t) &= \phi_{0,\ell} + \int_0^t \dot{\phi}_\ell(\tau)\, d\tau \\ \dot{\phi}_\ell(t) &= \dot{\phi}_{i,\ell} + \mathcal{B}_\ell(t), \end{aligned} \tag{4.7}$$

where $\phi_{0,\ell}$, and $\dot{\phi}_{i,\ell}$ are the initial AoA and the initial rate of change for the AoA, respectively. The variation term $\dot{\phi}_\ell(t)$ denotes the rate of change in AoA. We model the changes in $\phi(t)$ through modeling its rate of change $\dot{\phi}(t)$. In a general environment, users can accelerate, decelerate, rotate and may move on curved paths. In Fig. 4.3, we depict two different sample paths of the progression over time of the AoA based on the proposed variation from Eq. (4.7). Both paths show that the proposed variation in the AoA is slow when the curve keeps increasing or decreasing. Moreover, sudden

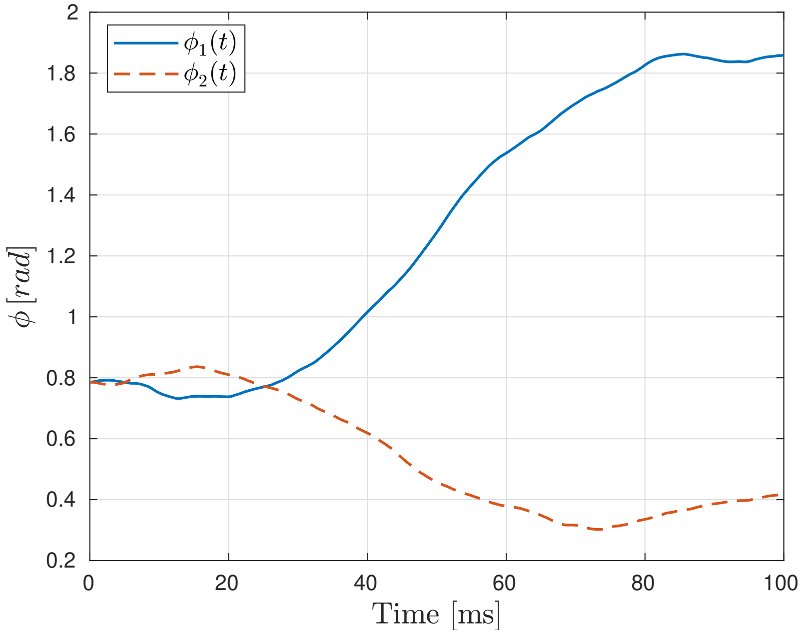

Figure 4.3: Sample paths of the AoA progression over time

reflection in the curve corresponds to a severe change in the AoA, which may come from reversing the motion direction or any other sudden variation in the channel.

The objective of Chapter 5 is not to provide detailed models of motion and integrate them into a cumbersome calculus. Instead, we aim to convey the value of incorporating the variations into beamforming. As a result, we use an approach in which the vagaries of the mobility are summarized in a general stochastic model. In particular, as a representation of $\dot{\phi}(t)$, we use $\mathcal{B}_\ell(t)$, a zero mean Brownian motion process with variance $Q\,t$, where $d\mathcal{B}_\ell(t) = \omega_\ell(t)\,dt$, and $\omega_\ell(t)$ is a zero-mean White Gaussian process with a Power Spectral Density (PSD) Q for all frequencies $-\infty < f < \infty$. A small value of Q means that $\dot{\phi}(t)$ is almost fixed (and that changes in $\phi(t)$ is steady), and vice versa for large values of Q.

Following the same assumption of the sparse channel, and given the knowledge of the path gain found in the previous stage, the measurement Eq. (4.6) can be rewritten as follows:

$$y_k = \frac{1}{N}\sum_{m=0}^{N-1} e^{-j2\pi\Delta m[\cos(\phi_k)-\cos(\bar{\phi}_k)]} + \acute{n}_k, \tag{4.8}$$

where $\acute{n}_k \sim \mathbb{C}\mathcal{N}(0, \frac{1}{\rho})$, $\rho = N\,|\alpha\, p|^2/\sigma_v^2$ is the SNR including the array gain, and $|\alpha\, p|^2/\sigma_v^2$ is SNR for each antenna element. Also, we assume that α is perfectly estimated in the previous stage. Then, there is no amplitude or phase error affecting the signal part. To simplify the notation of Eq. (4.8) , let us define the signal part, excluding the path gain, as:

$$h\left(\phi, \bar{\phi}\right) \triangleq \frac{1}{N}\sum_{m=0}^{N-1} e^{-j2\pi\Delta m[\cos(\phi)-\cos(\bar{\phi})]}. \tag{4.9}$$

CHAPTER 5

CONTINUOUS BEAM ALIGNMENT FOR MOBILE MIMO

5.1 Introduction

In this chapter, we provide a tracking algorithm that continually updates the beam-pointing direction, though the possible channel measurements are sparse, via the transmission of reference/pilot symbols. Away from the classical beam tracking algorithms, which correct the estimate of beam angle based on reference/pilot symbols and fixate them pending the arrival of the next pilot symbol, our method models and uses incremental beam variations in-between pilot symbols by predicting the beam angle variations at the transmitter and the receiver. The proposed approach, which we denote as Continuous-Discrete tracking, utilizes the physical nature of beam angle variation in the angular domain as a function of time to set up a state transition model. This model fuses information with channel measurements under three different frameworks: (i) an Extended Kalman Filter (EKF), (ii) a Fast Beam Tracking algorithm (iii) a Main-Lobe approximation.

Following this introduction, Section 5.2 provides a motivating example to elaborate the key idea of the Continuous-Discrete tracking approach. The particular assumptions of a different array configuration are provided in Section 5.3, and the

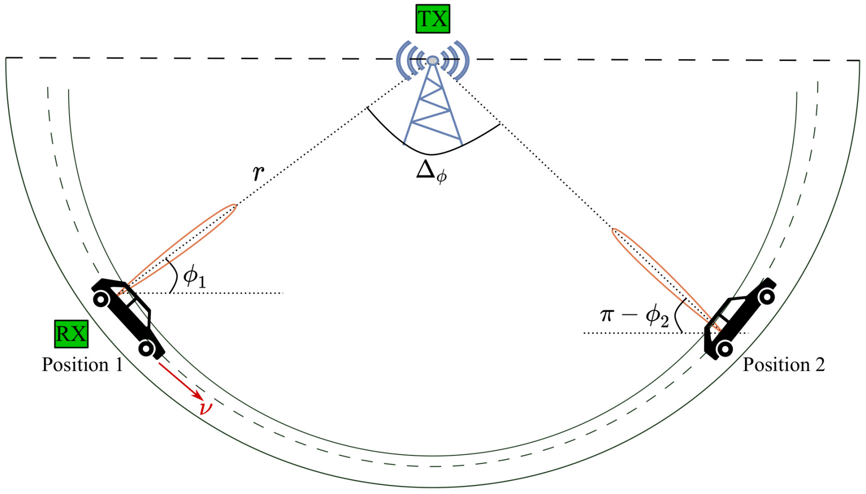

Figure 5.1: Example of a moving receiver with a Continuous-Discrete tracking

problem statement is given in Section 5.4. Section 5.5 demonstrates the Continuous-Discrete beam tracking approaches, and Section 5.6 provides an analytical discussion of a complementary problem to the beam tracking problem, represented by how to choose the pilot period. Section 5.7 shows results comparing the Continuous-Discrete proposal to its counterparts and evaluating methods of selecting the Pilot Period. Finally, section 5.8 summarizes this chapter.

5.2 Illustrative Example

In this section, we provide a simplified example to demonstrate our proposed Continuous-Discrete beam tracking solution and compare it against the traditional discrete beam tracking approaches. The fusion of discrete measurements and continuous AoA updates (which enables continuous beam updates) is called ”Continuous-Discrete” Beam Tracking.

In the example shown in Fig. 5.1, a Transmitter (TX) with a single antenna serves a moving Receiver (RX) with a directional antenna gain. The RX moves along the shown circular path with a constant velocity ν. Let us assume that at position 1, the RX has accurately discovered the AoA, ϕ, of the strongest channel path and has aligned its receive antenna beam towards that path. After that, the RX keeps tracking ϕ using periodic pilot symbols that arrive every T seconds. Upon the arrival of a pilot symbol, the RX updates the estimate of the AoA, ϕ, and its slope variation, $\frac{d\phi}{dt}$. Using the slope variation, the RX predicts the change in the AoA and continuously updates the beamforming vectors to stay tightly coupled with the incoming path.

Recall that RX moves with constant angular velocity. Hence, intuitively, as the prediction errors of the AoA and the slope variations go to zero, the period $T \to \infty$, which means that pilot symbols are not needed to keep tracking the AoA. That is because $\frac{d\phi}{dt}$ perfectly tells us precisely what the value of ϕ will be at any future time. On the contrary, "Discrete" Beam Tracking solutions only update the AoA **once** every pilot symbol arrival. That is, discrete tracking does not update the AoA estimate in the time duration in between pilot arrivals. Also discrete tracking does not rely on AoA rate of change information. Hence, the misalignment between the beam direction and the incoming paths increases as the pilot period increase. This means that, in a Discrete tracking approach, the RX needs to minimize the period T (increase the pilot overhead) as the beamwidth decreases (array size increase). Our proposed Continuous-Discrete measurement framework incorporates extra system information embodied in the rate of change of the AoA. This extra information allows us to predict how the AoA changes even when no measurements are available. This, in turn, allows us to extend the pilot period without significantly degrading the link quality or risking losing beam alignment.

Now, let us introduce how the AoA changes based on the special scenario assumed in Fig. 5.1. The RX at position 1 is moving with constant velocity ν, and the AoA

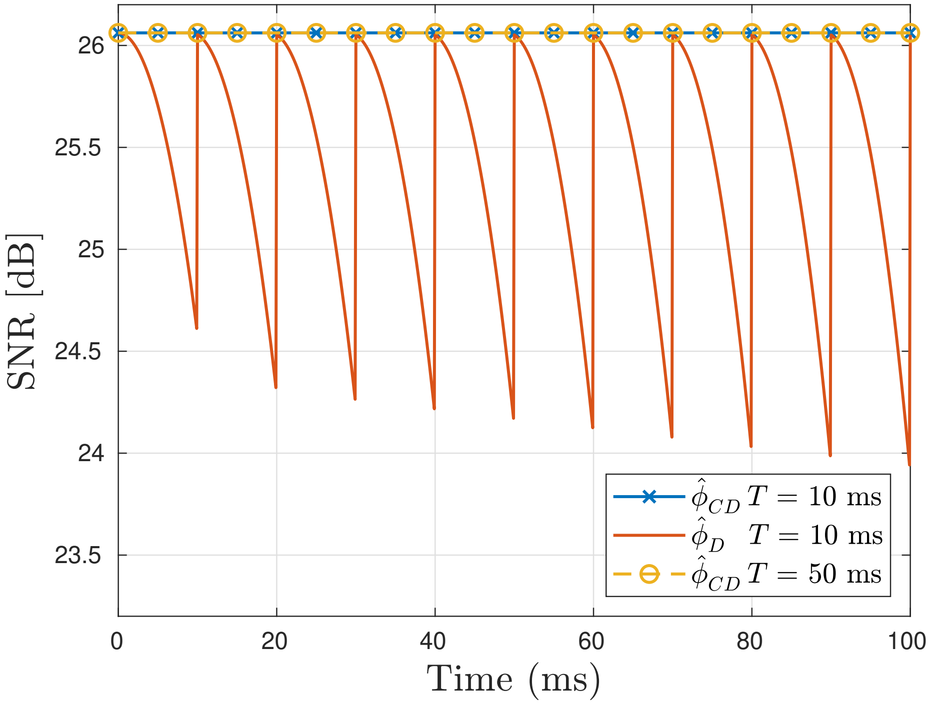

Figure 5.2: SNR for Continuous-Discrete and Discrete tracking

changes continuously based on the following equation:

$$\phi(t) = \phi_0 + \frac{\nu}{r} t, \tag{5.1}$$

where r is the distance from the TX to the RX. So, after a pilot period T, the RX will move to position 2, and the new AoA is $\phi_2 = \phi_1 + \frac{\nu}{r} T$. The Continuous-Discrete tracking allows us to update the beam direction continuously based on a prediction of the angular velocity $\frac{\nu}{r}$, while Discrete tracking only updates the beam direction upon pilot arrival, (i.e., position 1,2). Fig. 5.2, shows the Signal to Noise Ratio (SNR) for the example shown in Fig. 5.1, under both Discrete and Continuous-Discrete measurement frameworks. For that experiment, the total tracking time is 100 ms, $\nu = 100$ Km/hr, $r = 20$ m, and $\phi_0 = \pi/4$, and the two values for the pilot period $T = \{10, 50\}$ ms. The results from Fig. 5.2 reveals the weakness of the Discrete tracking approaches, where the instantaneous SNR drops drastically in between pilot symbols. To overcome the drop in the SNR, the pilot period should be decreased, i.e., $T < 10$ ms. On the other hand, the prediction of the rate of change of the AoA makes the Continuous-Discrete framework to stay tightly coupled even when only two pilot symbols are used over the entire tracking duration (i.e., $T = 50$ ms). Furthermore, the Continuous-Discrete approach can stay aligned without any pilot symbols as long as the prediction of the slope variation is available.

In this example, we have considered an oversimplified scenario. In a real system, however, the channel environment becomes more complex, requiring more sophisticated mathematical modeling and tracking techniques. Modeling real system complexities will be tackled in the following sections. We will see that errors in the prediction of the slope variation force the Continuous-Discrete solution to limit the pilot period to alleviate these errors. However, Continuous-Discrete approaches still can do better than the Discrete approach, as measured in two metrics: (1) Low Pilot Overhead, where the pilot period is longer than the period of the Discrete case. (2) SNR, where the Continuous-Discrete can have higher SNR than the Discrete case for the same pilot period.

5.3 Uniform Planar Arrays

The following sections follow the system model introduced in Chapter 4, especially the specific assumptions in Section 4.3.2. Up to this point, development in Eqs. (4.1), (4.4), (4.5) and (4.8) is based on ULAs. Here, we turn our attention to Uniform Planar Arrays (UPA) since they provide higher gain coupled with resilience to channel variations. We assume a square UPA where N elements are equally spaced and arranged over the area of a square. The steering and the beamforming vectors are given by:

$$\boldsymbol{a}_P(\phi, \theta) = \boldsymbol{a}_R(\theta) \otimes \boldsymbol{a}_R(\phi), \tag{5.2}$$

where $\otimes$ is the Kronecker product, while ϕ and θ are the azimuth and elevation angles, respectively. We assume AoA variation only in the azimuth direction, and we fix $\theta = 90°$. The beamforming vector is given by $\boldsymbol{w}_P(\bar{\phi}_k) = \boldsymbol{a}_P(\bar{\phi}_k)/\sqrt{N}$. Now, the model for the UPA is based on Eq. (5.2), and $\boldsymbol{w}_P(\bar{\phi}_k)$.

5.4 Problem Statement

Our objective is to minimize the instantaneous MSE between the true AoA $\phi(t)$ and its estimate $\hat{\phi}(t)$, which can be stated by:

$$\min_{\hat{\phi}(t)} \mathbb{E}[(\phi(t) - \hat{\phi}(t))^2] \tag{5.3}$$

While traditional solutions update $\hat{\phi}(t)$ at discrete measurement instances only, which create larger MSE as $\phi(t)$ drifts in-between pilots, we update $\hat{\phi}(t)$ continuously using an estimate of the AoA rate of change $\dot{\phi}(t)$ (recall Eq. (4.7)). We define the system state as $\boldsymbol{x}(t) \triangleq \begin{bmatrix} \phi(t) & \dot{\phi}(t) \end{bmatrix}^T$, and let $\hat{\boldsymbol{x}}(t)$ be its estimate, whose error covariance matrix is $\boldsymbol{P}(t)$, where

$$\boldsymbol{P}(t) \triangleq \mathbb{E}\left[(\boldsymbol{x}(t) - \hat{\boldsymbol{x}}(t))(\boldsymbol{x}(t) - \hat{\boldsymbol{x}}(t))^T\right] \tag{5.4}$$

The estimate of $\boldsymbol{x}(t)$, which incorporates both the AoA and its rate of change, is tackled in the following section.

5.5 Continuous-Discrete Beam Tracking Approaches

In traditional beam tracking, the estimate of AoA is updated using a pilot symbol that arrives each time slot, and the RX fixes the beam direction to that estimate until the arrival of the next pilot symbol. In contrast, Continuous-Discrete beam tracking exploits the prediction of the rate of change of the channel variation to update the beam direction and continuously minimize the instantaneous MSE. Furthermore, the approach presented here hinges on updating the estimate of the AoA not only based on pilot symbols but also continuous predictions of the rate of variations of the AoA in between pilots. In other words, we perform continuous beam tracking instead of abrupt adjustments at each pilot.

In this section, we apply the Continuous-Discrete approach to three different techniques to prove that the proposed approach improves the MSE over discrete baseline solutions. The three frameworks are listed as follows:

- An Extended Kalman Filter: An extended version of the well-known Kalman Filter, which is more suitable to a non-linear system.
- A Fast Beam Tracking: The proposed framework in [53], targets converging the MSE faster to the CRLB.
- Main-Lobe Approximation: A novel approach used to track the beam direction based on an approximation of the amplitude of main-lobe proposed in Section 5.5.3.

Following this, we provide a detailed discussion of the three proposed approaches.

5.5.1 Approach 1: Extended Kalman Filter

The Kalman Filter is a popular tool used in tracking problems, which motivates its use in beam tracking. However, recall from Eq. (4.8) that the measurement y_k is a non-linear function of the AoA (ϕ_k). This makes the traditional Kalman Filter unsuitable for this system. Instead, the EKF is the non-linear version of the KF, which is more suitable for the considered non-linear system in this chapter. The EKF can be described by two equations: (1) **State**, which incorporates the continuous dynamics in the AoA ($\phi(t)$), and its rate of change ($\dot{\phi}(t)$). Hence, we can write the state dynamics of the Continuous-Discrete Extended Kalman Filter (EKF$_{CD}$) as follows:

$$\begin{aligned} \dot{\boldsymbol{x}}(t) &= \begin{bmatrix} \dot{\phi}(t) & \frac{d\mathcal{B}(t)}{dt} \end{bmatrix}^T \\ &= \boldsymbol{A}\,\boldsymbol{x}(t) + \boldsymbol{g}\,\omega(t) \\ &= \begin{bmatrix} 0 & 1 \\ 0 & 0 \end{bmatrix} \boldsymbol{x}(t) + \begin{bmatrix} 0 \\ 1 \end{bmatrix} \omega(t), \end{aligned} \tag{5.5}$$

where, $\dot{\boldsymbol{x}}(t)$ is a vector of entry-wise derivative of $\boldsymbol{x}(t)$ with respect to the time, and (2) **Measurement/Observation**, which represents the channel measurements using known pilot symbols, and it is given by Eq. (4.8). The derivation of the state dynamics of the EKF$_{CD}$ can be found in [68], but we only provide a sketch as follows: The main idea of the EKF derivation is the linearization of the signal part ($h(\boldsymbol{x}_k)$) of Eq. (4.8). The following procedures are the same as that of the standard Kalman filter which can be found in [68].

The standard recursion equations (see [68]) are divided into two stages: (1) **Prediction**, and (2) **Update**. The prediction stage is given by:

$$\dot{\hat{\boldsymbol{x}}}(t) = \boldsymbol{A}\,\hat{\boldsymbol{x}}(t) \tag{5.6}$$

$$\dot{\hat{\boldsymbol{P}}}(t) = \boldsymbol{A}\,\boldsymbol{P}(t) + \boldsymbol{P}(t)\,\boldsymbol{A}^T + \boldsymbol{g}\,Q\,\boldsymbol{g}^T, \tag{5.7}$$

where $\dot{\hat{\boldsymbol{x}}}(t)$ is the prediction of the time derivative of the state vector $\boldsymbol{x}(t)$, $\dot{\hat{\boldsymbol{P}}}(t)$ is the prediction of the time derivative of $\boldsymbol{P}(t)$, and $Q\,\delta(\tau) = \mathbb{E}[w(t)\,w(t+\tau)]$ is the process covariance that drives the state vector, and is assumed to be bounded by Q. The estimate $\hat{\boldsymbol{x}}(t)$ during the prediction stage is the solution of the differential equation in (5.6). The update stage, which amends the k^{th} iteration of the standard Kalman gain ($\mathbb{K}_k$), is given by:

$$\mathbb{K}_k = \boldsymbol{P}_k^{k-1}\,\boldsymbol{H}_k^{\dagger}\left(\boldsymbol{H}_k\,\boldsymbol{P}_k^{k-1}\,\boldsymbol{H}_k^{\dagger} + \frac{1}{\rho}\right)^{-1} \tag{5.8}$$

$$\boldsymbol{P}_k^{k} = (\mathrm{I} - \mathbb{K}_k\,\boldsymbol{H}_k)\boldsymbol{P}_k^{k-1} \tag{5.9}$$

$$\hat{\boldsymbol{x}}_k^{k} = \hat{\boldsymbol{x}}_k^{k-1} + \mathbb{K}_k\left(y_k - h(\hat{\boldsymbol{x}}_k^{k-1})\right), \tag{5.10}$$

where $\hat{\boldsymbol{x}}_k^{k-1}$, and $\boldsymbol{P}_k^{k-1}$ is the estimate and the error covariance matrix at k^{th} iteration given $k-1$ measurements. Finally, $\boldsymbol{H}_k = \nabla_{\boldsymbol{x}_k} h|_{\boldsymbol{x}_k = \hat{\boldsymbol{x}}_k^{k-1}}$ is the gradient of the signal part ($h(\boldsymbol{x}_k)$) and estimated at $\hat{\boldsymbol{x}}_k^{k-1}$.

An overview of the EKF$_{CD}$ procedure can be described in Fig. 5.3. First, we assume our knowledge of the estimate of the initial AoA ϕ_0. Then, the state is updated based on Eq. (5.10) if a measurement is available. Otherwise, we repeat the prediction stage n_s times, i.e., we make a prediction every $T\,/\,n_s$ seconds. When the tracking period is over, we start searching for a fresh estimate of the AoA, similar to estimating ϕ_0. In this chapter, our main focus is *beam tracking*, and our solution complements any *beam discovery* (initial AoA estimation). Hence the latter is not included in this work. Further, optimizing the tracking period length is left as future work.

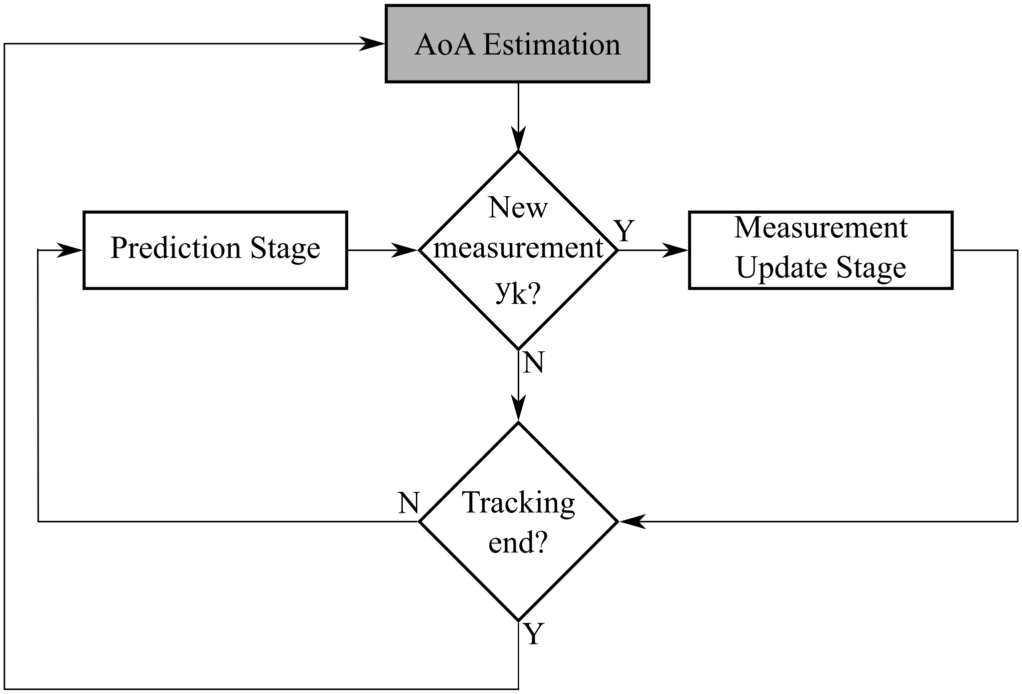

Figure 5.3: An overview of Continuous-Discrete EKF procedure.

In the implementation of EKF$_{CD}$, we replaced $\boldsymbol{H}_k$, y_k, and h by the corresponding matrix/vector $\tilde{\boldsymbol{H}}_k = [\Re[\boldsymbol{H}_k], \Im[\boldsymbol{H}_k]]^T$, $\tilde{\boldsymbol{y}}_k = [\Re[y_k], \Im[y_k]]^T$, and $\tilde{\boldsymbol{h}} = [\Re[h], \Im[h]]^T$, respectively, to cast the problem as a real-valued problem, similar to [52]. However, unlike [52], we utilize the pointing direction of the beamforming vector to be the previous estimate, i.e., $\bar{\phi}_0 = \phi_0$, and $\bar{\phi}_k = \hat{\phi}_k^{k-1}$.

5.5.2 Approach 2: Fast Beam Tracking

The FBT$_D$ was proposed in [53] as a low complexity algorithm that makes the MSE of the true AoA converge faster to the CRLB. In [53], they considered both the beam discovery and the beam tracking problems. In this section, we are only concerned with extending the discrete FBT$_D$ (beam tracking only) to a Continuous-Discrete Fast Beam Tracking (FBT$_{CD}$) solution. The key idea of the Continuous-Discrete is to predict the slope variation of the AoA, so we need a prediction of the slope variation besides the estimate of the AoA itself using FBT$_D$. We take advantage of the prediction stage in the EKF$_{CD}$ to continuously predict the AoA and its slope between two pilot symbols. Two stages describe the recursion of the FBT$_{CD}$: (1) the **prediction** stage using equation (5.6), which continuously predicts the estimate of the AoA and its rate of change found in the update stage. (2) the **update** stage is explained by the following two steps:

Discrete Fast Beam Tracking

The first step is to update the AoA using the FBT$_D$ [53], which can be described as follows:

$$\hat{\beta}_k = \Big[\hat{\beta}_{k-1} - a_n\, \Im[y_k]\Big]_{-1}^{1}, \tag{5.11}$$

where $\hat{\beta}_k = \sin(\hat{\phi}_k)$, $\hat{\beta}_{k-1}$ is the current and the previous estimates of $\sin(\phi_k)$ and $\sin(\phi_{k-1})$ respectively, and a_n is the step size. The estimate $\hat{\phi}_k$ is found by taking the inverse of the sine function. To accommodate for differences from the model of [53], we recalculate the step size as follows:

$$a_n = \frac{\partial \log P(y_k|\hat{\beta}_{k-1}\,, \boldsymbol{w}(\hat{\phi}_{k-1}))}{\partial \hat{\beta}_{k-1}} \Bigg/ I\left(\hat{\beta}_{k-1}, \boldsymbol{w}(\hat{\phi}_{k-1})\right) \tag{5.12}$$

It is easy to find the nominator and the denominator (Fisher Information) of a_n by the following:

$$\begin{aligned} I\left(\hat{\beta}_{k-1}, \boldsymbol{w}(\hat{\phi}_{k-1})\right) &= \mathbb{E}\left[-\frac{\partial^2 \log P(y_k|\hat{\beta}_{k-1}\,, \boldsymbol{w}(\hat{\phi}_{k-1}))}{\partial^2 \hat{\beta}_{k-1}}\right] \\ &= 2(N-1)^2\pi^2\Delta^2\rho, \end{aligned} \tag{5.13}$$

Also,

$$\frac{\partial \log P(y_k|\hat{\beta}_{k-1}\,, \boldsymbol{w}(\hat{\phi}_{k-1}))}{\partial \hat{\beta}_{k-1}} = 2\pi\Delta(N-1)\rho \tag{5.14}$$

Hence, we have the step size as:

$$a_n = [(N-1)\,\pi\,\Delta]^{-1} \tag{5.15}$$

Slope Variation Update

The FBT$_D$ does not consider updating the slope variation of the AoA ($\dot{\phi}$), we utilize the EKF$_{CD}$ in the background of FBT$_{CD}$ to update $\dot{\phi}$, which is needed for the prediction stage.

Algorithm 1 Discrete Beam Tracking Algorithm

```
Input: $k \geq 1$, $\hat{\phi}_0 = \phi_0$, $T$, and $T_{LR}$   ▷ $T$ :Pilot period, and $T_{LR}$ link reestablishment time.
Output: $\hat{\phi}_k$
while $kT \leq T_{LR}$ do
    $\varphi = \angle \hat{h}(\phi_k, \hat{\phi}_{k-1})$, and $\hat{\Omega}_{k-1} = \cos(\hat{\phi}_{k-1})$
    $\hat{\phi}_{k\pm} = \arccos\left(\left[\hat{\Omega}_{k-1} \pm \sqrt{-\frac{2}{N^2}\log\left|\hat{h}(\phi_k, \hat{\phi}_{k-1})\right|}\right]_{-1}^{1}\right)$
    $\varphi_{\pm} = \angle h(\hat{\phi}_{k\pm}, \hat{\phi}_{k-1})$
    if $\varphi = \varphi_{+}$ then
        $\hat{\phi}_k = \hat{\phi}_{k+}$
    else
        $\hat{\phi}_k = \hat{\phi}_{k-}$
    end if
    $k \leftarrow k + 1$
end while
```

5.5.3 Approach 3: Main-Lobe Tracking Algorithm

In EKF$_{CD}$ and FBT$_{CD}$, the slope variation estimate was found using an EKF framework. Here, we introduce a Continuous-Discrete Main-Lobe Tracking Algorithm (ML$_{CD}$) based on the proposed Algorithm 1 to update the estimate of the AoA. The estimate of the rate of change ($\hat{\dot{\phi}}$) is updated using an MMSE of the difference between two consecutive slope variation instants ($\dot{\phi}_k - \hat{\dot{\phi}}_{k-1}$). The proposed approach not only proves the validity of the Continuous-Discrete overall discrete baseline but also provides a tractable analysis needed for the upcoming Section 5.6. The ML$_{CD}$ is described by two stages as in the EKF$_{CD}$, and FBT$_{CD}$; the **prediction** stage using Eq. (5.6), and **update** stage can be divided into two separate steps: (i) updating the AoA based on a Discrete Main-Lobe Tracking (ML$_D$), and (ii) updating the slope variation.

Discrete Main-Lobe Tracking Algorithm

In this section, we propose a Discrete Main-Lobe Tracking Algorithm, which is consistent with the definition of beam coherence time from [17]. This model is built over the assumption that a pilot symbol arrives each T within the main-lobe (i.e., within the beam coherence time). This approach is based on the following approximation of the received signal part for ULAs:

$$\left| h(\phi_k, \hat{\phi}_{k-1}) \right| \approx e^{-\frac{N^2}{2}[\cos(\phi_k) - \cos(\hat{\phi}_{k-1})]^2} \tag{5.16}$$

A comparison between the true value of the amplitude of the received signal and the approximation given in Eq. (5.16) can be shown in Fig. 5.4. We can notice from the figure that the main beam-lobe of the true value ULA$_T$ is almost the same as

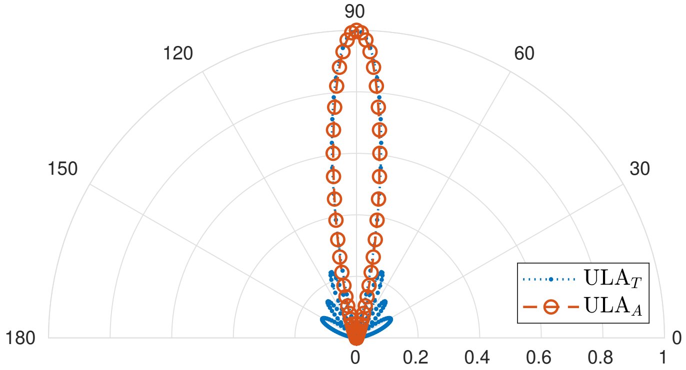

Figure 5.4: Beam Pattern Approximation for 8-element ULA

the approximation ULA$_A$, and the side-lobes can be neglected, especially for a large array size.

The basic idea of the proposed algorithm is that; the value of the signal part $h(\phi_k, \hat{\phi}_{k-1})$: $\mathbb{R}^2 \rightarrow \mathbb{C}$ is a function of the true value ϕ_k, and the previous estimate $\hat{\phi}_{k-1}$. If we have an estimate of the signal part from a given measurement, and using the approximation formula in Eq. (5.16) we can solve it to find the current estimate. We assume the signal and noise parts are zero-mean Gaussian with variances, σ_h^2, and R respectively. Also, we assume the signal and noise parts are orthogonal i.e. $\mathbb{E}[h\, n_k] = 0$. Hence, the Linear Minimum Mean Estimate (LMMSE) of $h(\phi_k, \hat{\phi}_{k-1})$ is found as follows:

$$\begin{aligned} \hat{h}(\phi_k, \hat{\phi}_{k-1}) &= y_k \, \frac{\sigma_h^2}{\sigma_h^2 + R} \\ &= y_k \, \frac{\rho}{\rho + 1} \end{aligned} \tag{5.17}$$

The current estimate is found by solving the approximation given in Eq. (5.16), and the estimate given in Eq. (5.17). An overview of the proposed algorithm is presented in Algorithm 1, which can be described as follows: first, we equalize the estimate from Eq. (5.17) with the approximation formula in Eq. (5.16), then take log for both sides. Also, we are going to change the symbol ϕ_k in Eqs. (5.16) and (5.17) with $\hat{\phi}_k$ since we looking for an estimate.

$$\log|\hat{h}(\hat{\phi}_k, \hat{\phi}_{k-1})| = -\frac{N^2}{2}[\cos(\hat{\phi}_k) - \cos(\hat{\phi}_{k-1})]^2 \tag{5.18}$$

Hence, the estimate found on Line 2 is found directly from Eq. (5.18). As we can notice from Fig. 5.4, we can have the same amplitude for two different values of AoA, that is why we need to compare the phases of the two possible solutions as found in Algorithm 1.

Slope Variation Update

The current estimate of the slope variation ($\hat{\dot{\phi}}_k$) is found as an update of $\hat{\dot{\phi}}_{k-1}$ as follows:

$$\hat{\dot{\phi}}_k = \hat{\dot{\phi}}_{k-1} + \frac{Q\,T\,\xi\,\Im[y_k]}{Q\,T\,\xi^2 + 0.5\,R}, \tag{5.19}$$

where $\xi = \pi\,T\,\sin(\hat{\phi}_{k-1})\,\frac{N-1}{2}$, and we assume initial estimate $\hat{\dot{\phi}}_0 = 0$. As shown from Eq. (5.19), the current estimate depends on the previous estimate and an update term. The update term is found as follows; first, we use a first order approximation of the signal part in the measurement equation by:

$$h(\dot{\phi}_k, \hat{\phi}_{k-1}) = h(\hat{\dot{\phi}}_{k-1}, \hat{\phi}_{k-1}) + \varepsilon_k\,h^{'}(\hat{\dot{\phi}}_{k-1}, \hat{\phi}_{k-1}), \tag{5.20}$$

where $\varepsilon_k = (\dot{\phi}_k - \hat{\dot{\phi}}_{k-1})$, and by assuming good estimate (i.e., $\hat{\dot{\phi}}_{k-1}$,$\hat{\phi}_{k-1}$) we can have $h^{'}(\hat{\dot{\phi}}_{k-1}, \hat{\phi}_{k-1}) \approx j\varepsilon_k\,\xi$, and $h(\hat{\dot{\phi}}_{k-1}, \hat{\phi}_{k-1}) \approx 1$. In that case, the imaginary part of the measurement equation is given by:

$$\Im[y_k] = \varepsilon_k\,\xi + \Im[n_k]/\rho, \tag{5.21}$$

where $\varepsilon_k \sim \mathcal{N}(0, Q\,T)$, and for a given ξ, the MMSE of ε_k (i.e., $\hat{\varepsilon}_k$) is given by:

$$\begin{aligned}\hat{\varepsilon}_k &= \mathbb{E}\left[\varepsilon_k | y_k\right] \\ &= \frac{Q\,T\,\xi\,\Im[y_k]}{Q\,T\,\xi^2 + 0.5\,R}\end{aligned} \tag{5.22}$$

5.6 Performance Evaluation

The main goal of beam tracking, is to elongate the link reestablishment time T_{LR}; the time at which we lost the tracking of the AoA, and we need to search for the new best incoming path. Recall the frame structure in Fig. 4.2, where we need to send a frame of k time slots with a fixed rate. In Section 5.7.1, we show that large array size is not able to cope with channel variation for a given *pilot period* (Time slot) T. Hence, we need to choose the *pilot period* T based on array size beside other factors we will discuss later. In the following, we propose two different ways to choose the *pilot period*; (i) comparable to the beam coherence and (ii) to maintain specific outage probability and fixed rate.

5.6.1 Beam Coherence Time

Intuitively, the *pilot period* T has to be comparable to the beam coherence time T_b to cope with the channel variation. From [17], the beam coherence time is defined as the time at which the power received at perfect alignment time drop by ζ at time $t + T_b$.

$$\frac{P(t+T_b)}{P(t)} = \zeta \tag{5.23}$$

Since we assume perfect alignment at time t, then the received power $P(t) = 1$. For

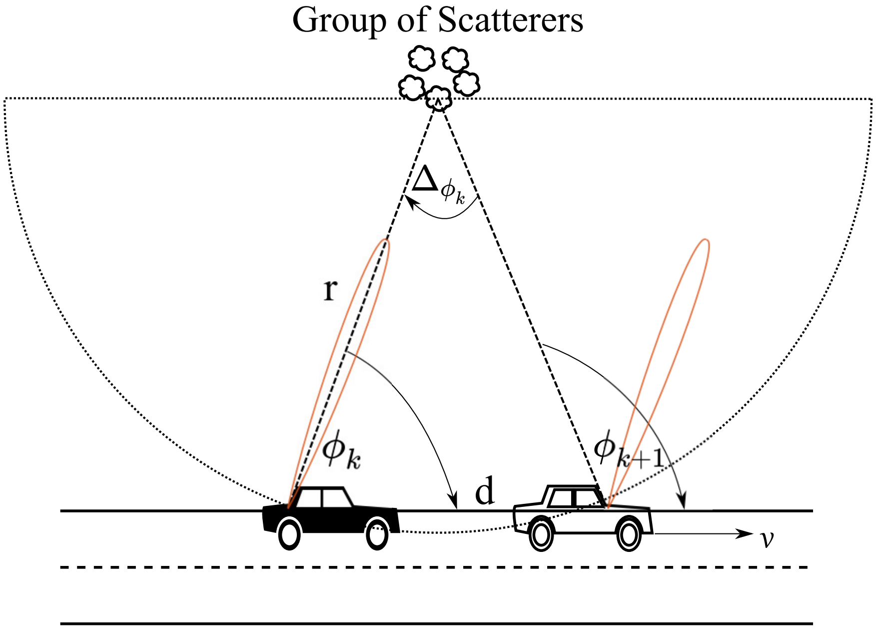

Figure 5.5: Model of variation over Pilot Period

ULA, the received power at time $t + T_b$ while ignoring the noise power is given by:

$$\begin{aligned} P(t+T_b) &= \left| \boldsymbol{w}^{\dagger}(\phi(t))\boldsymbol{a}_R(\phi(t+T)b)) \right|^2 \\ &= \frac{1}{N^2} \left| \sum_{m=0}^{N-1} e^{-j2\pi m\Delta(\cos(\phi(t+T_b))-\cos(\phi(t)))} \right|^2 \end{aligned} \tag{5.24}$$

Now, we try to visualize the picture of a simple example to grasp the whole idea. As shown in Fig. 5.5, we assume the receiver is perfectly aligned with the incoming path at the first position. The receiver is moving with speed v and a fixed beam direction equals to the AoA at the first position, i.e. ϕ_k. Hence, after motion for a distance d there will be a Δ_{ϕ_k} misalignment, and the received power will be dropped to ζ. Our model relates the channel variation to the angular variation $\dot{\phi}_k$, and Fig. 5.5

shows how we relate the linear speed v to that angular variation as:

$$\begin{aligned}\phi_{k+1} &= \phi_k + T\,\dot{\phi}_k \\ &= \phi_k + T\,\frac{v\,\sin(\phi_k)}{r},\end{aligned} \tag{5.25}$$

where r is the distance from source of the path to the receiver and now we can say that the angular variation is bounded by speed over the distance as : $\dot{\phi}_k \leq \frac{v}{r}$. This is the typical situation for the Discrete tracking approach, and we are seeking the *pilot period* T to be within the beam coherence time T_b.

For a Continuous-Discrete tracking algorithm, the beam direction changes dynamically based on estimate of the slope variation $\dot{\phi}_k$, then to find the pilot duration we need to take care of slope variation estimate in addition to the AoA variations. In this case, the notion of beam coherence time does not hold for the Continuous-Discrete algorithms, and we introduce the notion of the *Beam Locking Time* T_L. This time represents the duration at which the power will drop by ζ while the receiver continuously update the estimate of the AoA and the beamforming.

In order to find a consistent formula of the *pilot period*, we had to assume it is the time to have an average drop μ_ζ instead of ζ since both sides of Eq. (5.23) are random. Now, we introduce how to choose the *pilot period* for a Discrete and Continuous-Discrete beam tracking using Theorems 1.

Theorem 1. *For the channel model with angular variation given by Eq.* (4.7)*, the link reestablishment interval* T_{LR} *is achievable if the pilot period* $T \leq T_L$ *is given by:*

$$T_L = \sqrt{\frac{\frac{1}{\mu_\zeta^2} - 1}{2\,\kappa\,Q\,T_{LR}\,\sin^2(\phi_k) N^2}}, \tag{5.26}$$

where μ_ζ is the average drop in the received power, and $0 < \kappa < 1$, the lower value of κ the better estimate of the slope variations and the T_L gets larger. If $\kappa = 1$, then the beam locking time T_L is limited to the beam coherence time T_b which is used in the Discrete beam tracking to choose the *pilot period* T. Proof of Theorem 1 can be found in Appendix A.1, and A.2.

Clearly, the power will drop in the discrete beam tracking algorithm faster than the continuous-discrete tracking algorithms. This is because continuous-discrete tracking continuously varies the beamforming based on the prediction of the AoA variation and gain from discrete pilot updates. While the discrete approaches only update the AoA upon the arrival of pilot symbols.

5.6.2 Outage Probability

An outage event can be defined as a situation when the channel is so poor that no scheme can communicate reliably at a specific data rate. The highest data rate of reliable communication at a specific outage probability is denoted as the outage capacity [69]. Specifically, we can define the outage probability of a channel as the probability that the data rate is less than the threshold/targeted data rate. For the situation where the transmitter is aware of the channel distribution, this motivates the transmitter to choose the *pilot period* that sustain a specific outage probability P_{out} for a fixed rate $\mathcal{R}_f$. In that case, the *pilot period* is chosen based on Theorem 2.

Theorem 2. *For the channel model with angular variation given be Eq.* (4.7)*, the link reestablishment interval* T_{LR} *is achievable with outage probability* P_{out}*, and a fixed rate* $\mathcal{R}_f$ *if the pilot period* $T \leq T_o$ *is given by:*

$$T_o = \sqrt{\frac{\log\left(\frac{\rho}{(2^{\mathcal{R}_f} - 1)}\right)}{N^2 \sin^2(\phi_k) \kappa\, Q T_{LR} (\mathbb{Q}^{-1}(P_{out}/2))^2}}, \tag{5.27}$$

similarly, $0 < \kappa < 1$, and for $\kappa = 1$, then T_o is valid as the *pilot period* for the Discrete beam tracking algorithm, otherwise, T_o is valid for the Continuous-Discrete beam tracking algorithm.

Proof. From Appendix A.3, we get the outage probability for a Continuous-Discrete tracking approach is given by Eq. (A.20):

$$\begin{aligned} P_{out} &= P(\gamma \leq \gamma_k) \\ &= 2\,\mathbb{Q}\left(\sqrt{\frac{\log(\rho/\gamma_k)}{N^2 {T_o}^2 \sin^2(\phi_k) \kappa\, Q T_{LR}}}\right) \end{aligned} \tag{5.28}$$

for a given γ_k, the corresponding spectral efficiency is $\mathcal{R}_f = \log_2(1+\gamma_k)$. Alternatively, we can replace γ_k in Eq. (5.28) by $2^{\mathcal{R}_f} - 1$. After that, we divide both sides by 2, then take the inverse of the Q function. Finally, Eq. (5.27) is found directly by taking T_o to the left side. Similarly, The Discrete case where $\kappa = 1$ is derived in similar procedures as Eq. (5.27) by starting from the CDF for the Discrete case which is given by Eq. (A.17). □

5.6.3 Pilot Overhead Reduction

The key point of utilizing the spatial variations in-between two pilot symbols is to reduce pilot overhead by extending the pilot symbols duration. Now, we show how a Continuous-Discrete tracking algorithms reduce pilot overheads as follows:

Beam Coherence and Locking Time

$$\begin{aligned} \frac{T_b}{T_L} &= \sqrt{\frac{1/\mu_\zeta^2 - 1}{2\,Q\,T_{LR}\,\sin^2(\phi_k) N^2} \frac{2\,\kappa\,Q\,T_{LR}\,\sin^2(\phi_k) N^2}{1/\mu_\zeta^2 - 1}} \\ &= \sqrt{\kappa} \end{aligned} \tag{5.29}$$

Outage Probability Time

$$\begin{aligned}\frac{T_o(D)}{T_o(CD)} &= \sqrt{\frac{\log(\frac{\rho}{(2^{\mathcal{R}_f}-1)})\, N^2 \sin^2(\phi_k)\kappa\, QT_{LR}(\mathbb{Q}^{-1}(\frac{P_{out}}{2}))^2}{N^2 \sin^2(\phi_k) QT_{LR}(\mathbb{Q}^{-1}(\frac{P_{out}}{2}))^2\, \log(\frac{\rho}{(2^{\mathcal{R}_f}-1)})}} \\ &= \sqrt{\kappa}\end{aligned} \tag{5.30}$$

Hence, utilizing the Continuous-Discrete algorithms results in overhead reductions by $(1-\sqrt{\kappa})\%$.

5.6.4 Effective Achievable Rate

Now, we are looking to represent the overhead reduction by the effective achievable rate by excluding the time of pilots training. The effective rate is given by:

$$\begin{aligned}\mathcal{R}_e &= \eta\, \mathcal{R}_a \\ &= \frac{T - T_s}{T} \times \frac{T_{LR}}{T_{LR} + T_{sw}} \mathcal{R}_a,\end{aligned} \tag{5.31}$$

where $\mathcal{R}_a$ is the achievable rate, T will be replaced by T_b, T_L, T_o(D), and T_o(CD) for each case of choosing the *pilot period*. Also, T_s is the training time for a single pilot symbol, and T_{sw} is the beam sweeping time, which is needed to find the angle of arrival after losing the tracking. Considering the sweeping time, we utilize the same formula proposed by [17] based on the hierarchical beam code book in [14] and follows the IEEE 802.15.3c guidance. The formula was given as function of the beamwidth, which can be shown as function of the array size as:

$$T_{sw} = \mathbb{L}\, (\pi\, N)^{(2/\mathbb{L})}\, T_s, \tag{5.32}$$

where $\mathbb{L}$ is the number of levels in the hierarchical beam codebook given in [14].

5.7 Numerical Results

5.7.1 Performance of Beam Tracking Algorithms

In this section, we evaluate and compare the performance of EKF and FBT algorithms under both the Continuous-Discrete and the Discrete frameworks, while the ML_{CD} and ML_D are left to the evaluation in Section 5.7.2. For each experiment, we assume perfect knowledge of the initial AoA at $t = 0$, i.e., ϕ_0. We simulate $\dot{\phi}(t)$ as a Brownian motion and $\phi(t)$ as in Eq. (4.7), and we let the algorithms run for a total tracking time of 100 ms and average the output over 5000 runs. Our performance metrics are: (1) the MSE of the estimated AoA, and (2) the average received SNR. Except when stated otherwise, we let $Q = 10^4$, $N = 64$ ULA and we fix $\rho = 20$ dB. We evaluate the performance under two array orientations, i.e., ULA and UPA.

Different ULA Array Size: Fig. 5.6 depicts a sample path of the progression of the simulated true value of the AoA as well as its tracking performance using both EKF_{CD} and EKF_D algorithms when ULAs of sizes 16 and 64 are employed. The

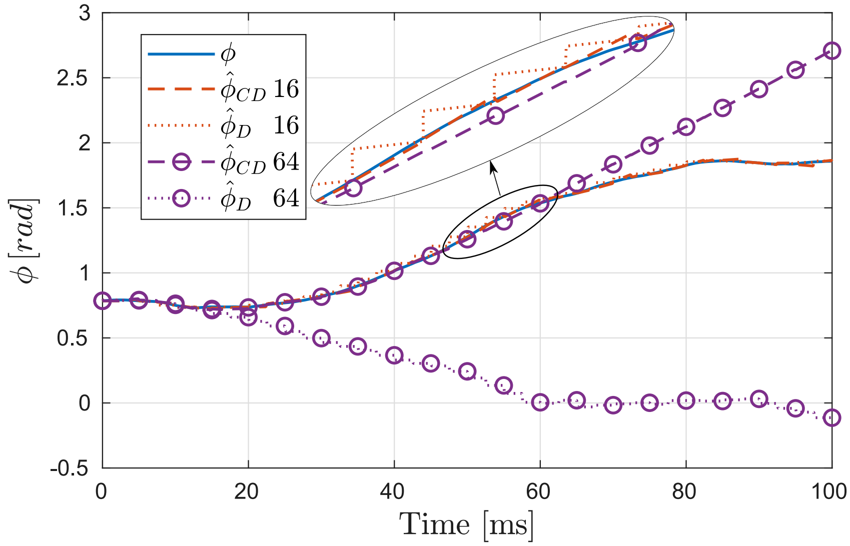

Figure 5.6: Angle of Arrival Tracking with 16 and 64 ULAs for $T = 2.5\,ms$.

pilot period is fixed at $T = 2.5\,ms$. For the ULA of size 16, both EKF$_{CD}$ and EKF$_D$ frameworks provide accurate tracking performance for the entire tracking duration. Only a closer inspection reveals the superiority of EKF$_{CD}$ as shown in the zoomed-in part. However, as the array size gets larger, the beamwidth gets narrower, making it harder to track the beam. Consequently, for ULAs with 64 antenna elements, we see a clear difference in favor of EKF$_{CD}$ where it is able to track the beam for a significantly longer time duration (∼200% longer), compared to EKF with discrete updates. In general, as the number of antenna elements increases, the performance gap between EKF$_{CD}$ and EKF$_D$ increases in favor of our EKD$_{CD}$ solution as long as the variation in the AoA over T is less than the variation over the beam coherence time.

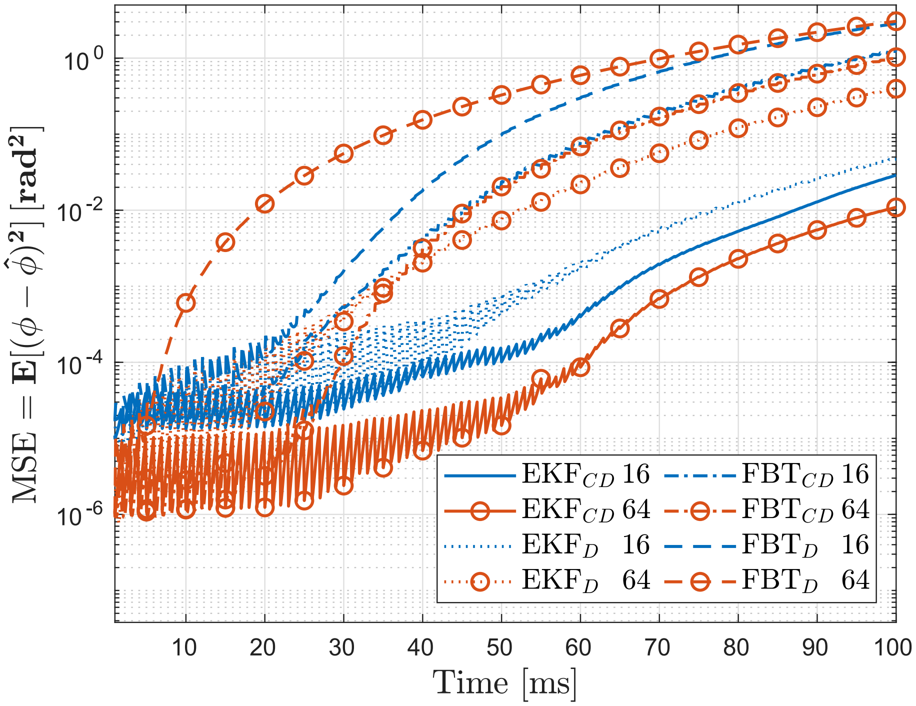

Figure 5.7: MSE for different tracking approaches using 16, and 64 ULAs

In Fig. 5.7, the MSE for the continuous-discrete and the discrete approaches for $T = 1.0\,ms$ is shown. Here, we also provide results for the FBT$_{CD}$ and FBT$_D$ algorithms. These results show that the continuous-discrete framework significantly improves performance over the baseline discrete solutions. We also see that EKF$_{CD}$ has the lowest MSE, i.e., best tracking performance, among all other solutions. Interestingly, EKF$_{CD}$ performs even better for the larger array size, despite the overall difficulty in tracking sharper beams. On the other hand, the performance of EKF$_D$ degrades by increasing the array size (especially when AoA variations become faster over the tracking time). This happens since the larger array size has shorter beam coherence time, and EKF$_D$ becomes unable to cope with the fast channel variation. The Effect of the array size over FBT$_{CD}$ and FBT$_D$ is similar to that of EKF$_{CD}$ and EKF$_D$. Yet, EKF$_D$ and EKF$_{CD}$ outperform the Fast-tracking approach (especially

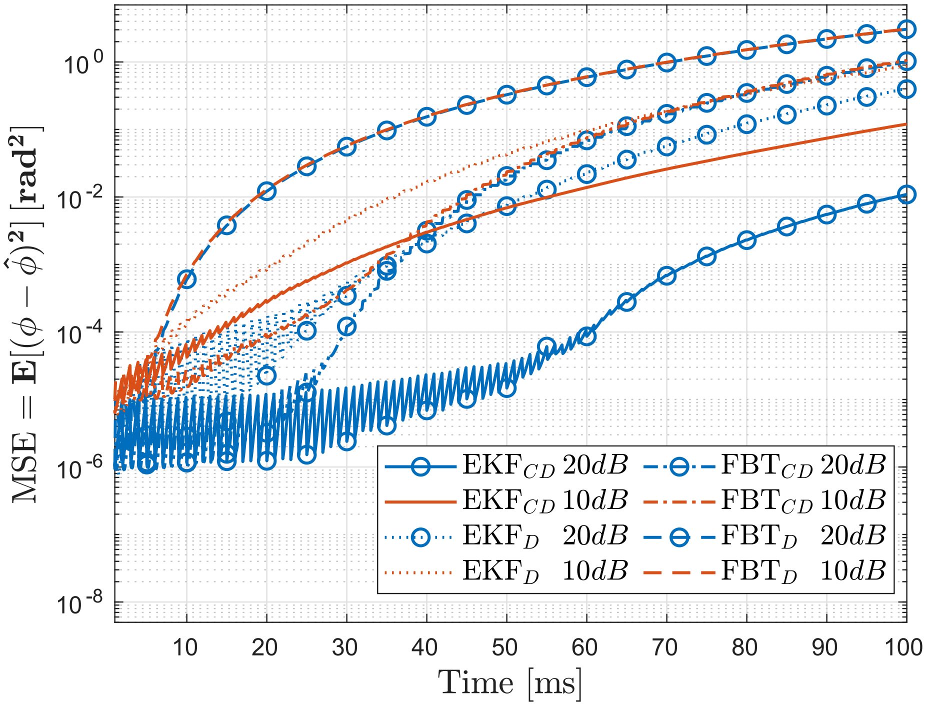

Figure 5.8: MSE for Different Tracking Approaches for 20, and 10 dB

when the channel variations become faster). EKF$_{CD}$ achieves 80% and 99.5% lower MSE than EKF$_D$, for 16 and 64 array sizes, respectively.

Different SNR values: Fig. 5.8 shows the MSE under different SNR values; 10 and 20 dB. Here, we fix the array size to 64 and the pilot period to $T = 1.0\,ms$. As expected, decreasing the SNR degrades the performance for all approaches. EKF$_{CD}$, however, still outperforms all other algorithms due to its ability to predict the rate of change of the AoA between pilot symbols. The superiority of EKF$_{CD}$ is very dominant that even at 10 dB, it still has comparable performance to FBT$_{CD}$ and EKF$_D$ with 20 dB. The MSE for all approaches is tiny at the beginning of the tracking period since the variation of AoA is negligible. As the tracking time advances, the variation in AoA increases, and the MSE for all approaches increases.

Different Pilot Frequencies: Measurement frequency is an important design parameter. More frequent pilots ensure better beam tracking, but it also wastes more transmission opportunities. Here, we shed more light on the effect of tracking performance as the measurement frequency changes, where we plot the MSE for a medium AoA variation at $Q = 10^3$ for a 64-element ULA, as shown in Fig. 5.9. First, we observe that for $T = 1\,ms$, the performance of both EKF$_{CD}$ and EKF$_D$ are almost identical at the measurement update instances. However, the MSE of EKF$_D$ fluctuates more aggressively in-between measurements. This is due to the AoA estimate of the EKF$_D$ being kept constant between measurements despite the continuous AoA changes over time. Second, accounting for the nature of variation between measurements gives an advantage to EKF$_{CD}$ and allows it to use less frequent measurements while keeping the MSE comparable to EKF$_D$. This can be seen when comparing the MSE of EKF$_{CD}$ with $T = 2.5\,ms$ to the MSE of EKF$_D$ with $T = 1.0\,ms$. Finally, at the same T, FBT$_{CD}$ achieves up to 99.8% lower MSE compared

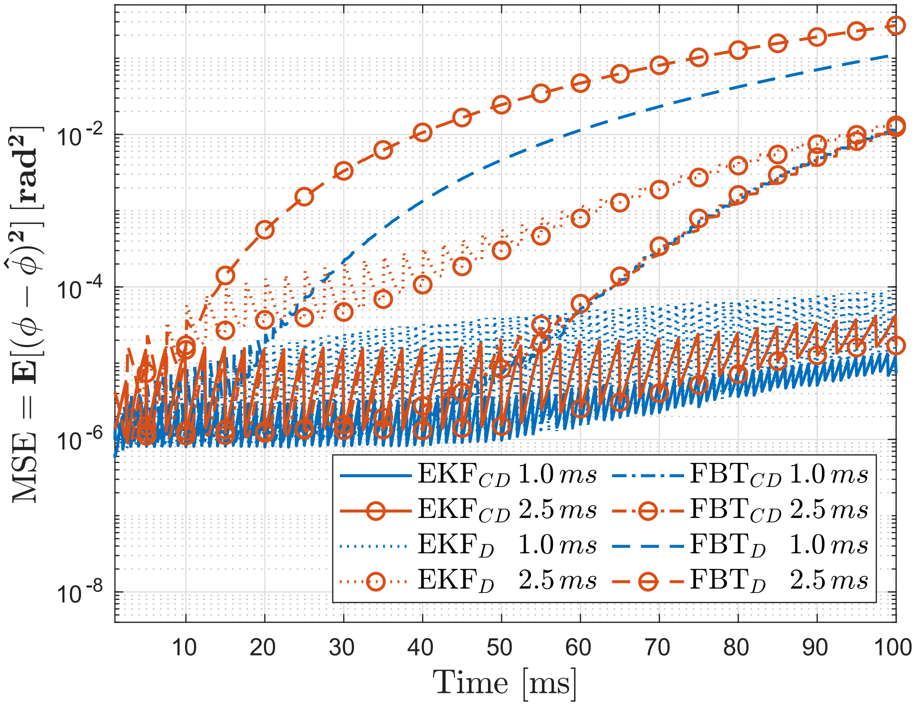

Figure 5.9: MSE for Different Tracking Approaches for $T = 1.0,\ 2.5\,ms$

to FBT$_D$. Also, FBT$_{CD}$ performs almost identically at both $T = 1.0$ and $2.5\,ms$, showing the effectiveness of continuous AoA updates.

In Fig. 5.10, we present the average received SNR for different T. Averaging is over the whole tracking time and 5000 runs. Here, we also normalize ρ, with respect to the array size. This normalization helps isolate the tracking performance as a function of the beamwidth only. Next in Fig. 5.11, we will remove this normalization and study the overall performance with sharp beams, by accounting for the beam gain, as well. We notice that average SNR is degraded by increasing the array size since increasing the array size decreases the beam coherence time. In order to have good performance over large array sizes, we need to utilize smaller T. The EKF$_{CD}$ outperforms the EKF$_D$ by 1 dB and up to 4 dB for small and large array sizes, respectively, while the FBT$_{CD}$ has an advantage by 4 dB and can reach 7 dB. Increasing the *pilot period*

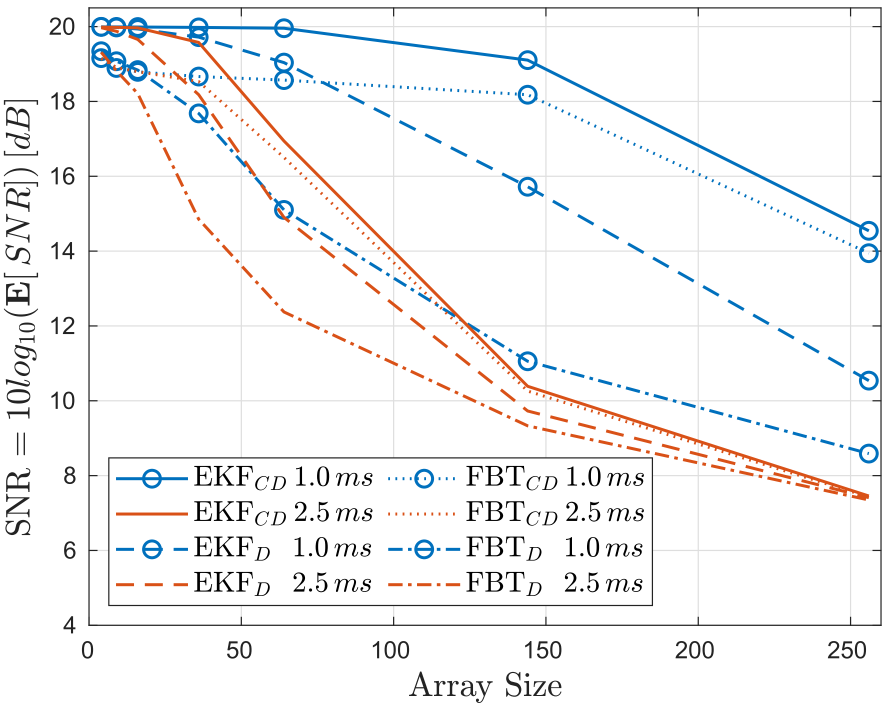

Figure 5.10: Average SNR for ULA for Different Array Sizes

degrades the average SNR for all approaches, yet EKF$_{CD}$ still outperforms EKF$_D$ by 2 dB for $T = 2.5\,ms$. Also, FBT$_{CD}$ has superiority over FBT$_D$ by 5 dB for $T = 2.5\,ms$.

Fig. 5.11 shows the average SNR for 16 dB per each antenna element. We observe that increasing the array size increases the average received SNR to a certain point, before it drops slowly for larger sizes. This can be explained by arguing that the array gain compensates for small mismatches in beam alignment, despite the difficulty imposed by the larger array size. However, as arrays get larger, beams get sharper, and alignment fails more often, leading to a drop in the average SNR.

Uniform Planar Arrays: A UPA has better spatial properties than ULA in terms of beam coherence time. Hence, a UPA can utilize longer T and still obtain better performance than ULA. We notice from Fig. 5.12 that UPA scenarios, which

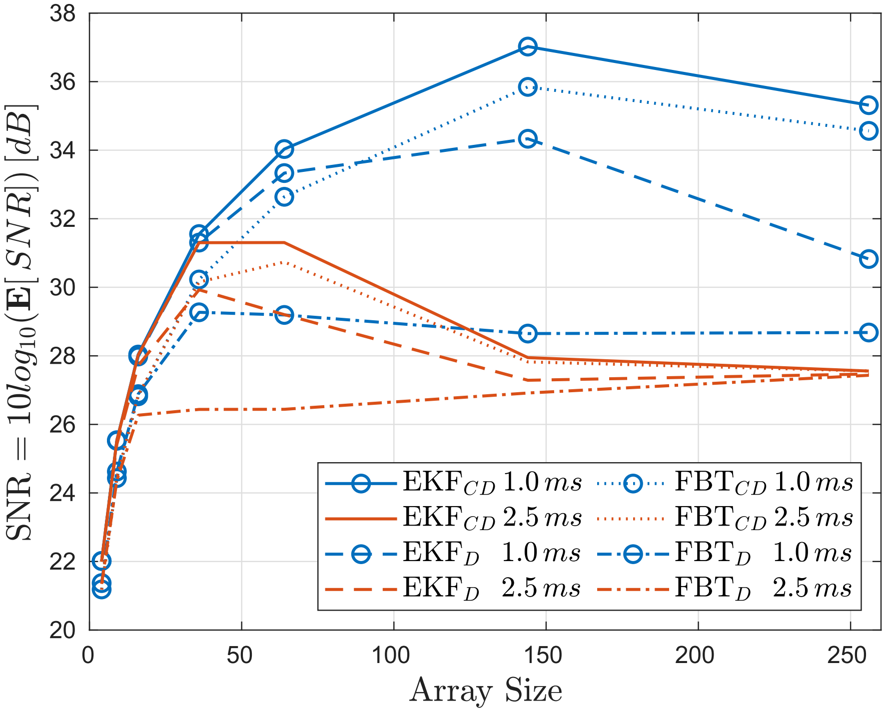

Figure 5.11: Average SNR for ULA for Different Array Sizes

are denoted by EKF-P$_{CD}$ and FBT-P$_{CD}$ have better average SNR for $T = 1.0,\, 2.5\,ms$, especially for large array sizes and fast channel variations.

Fig. 5.13 shows the effect of the array gain, similar to Fig. 5.11. The UPA shows a better use of the array gain, even for the large array size. Intuitively, the average SNR for UPA will eventually start dropping when the beam coherence time of larger arrays becomes much smaller than $T = 1.0,\, 2.5\,ms$.

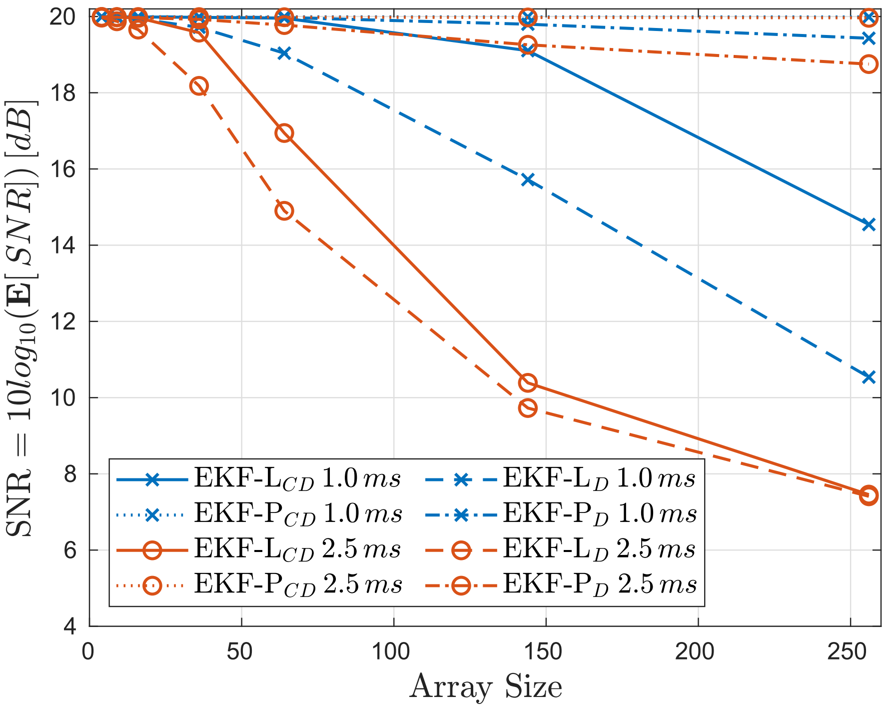

Figure 5.12: Average SNR for UPA, ULA for Different Array Sizes

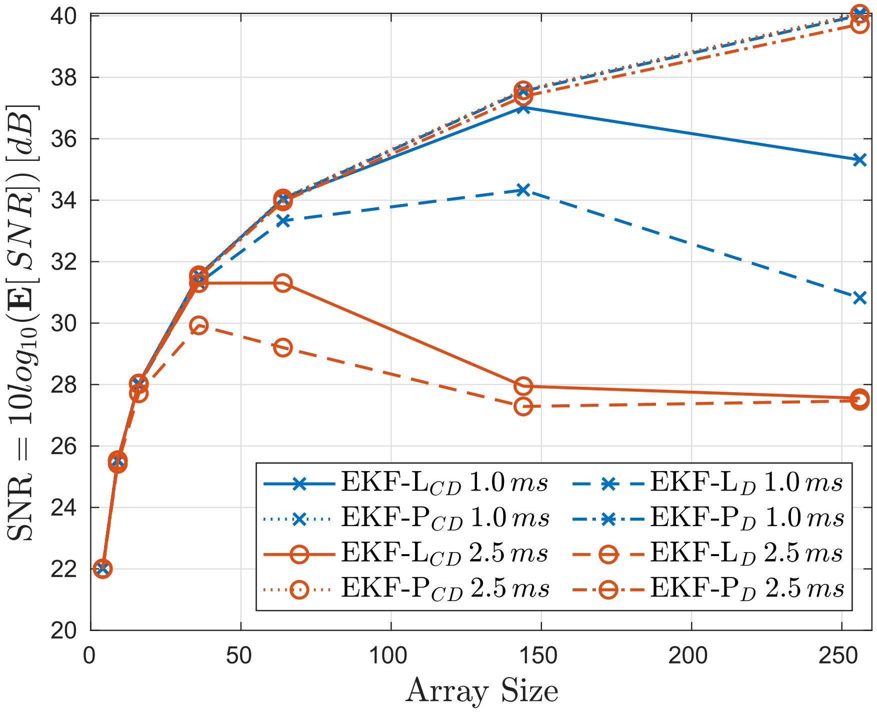

Figure 5.13: Average SNR for UPA, ULA for Different Array Sizes

Table 5.1: Pilot Overhead Reduction under two different methods of choosing T for Different Antenna Array Size with $T_{LR} = 100\,ms$

			Overhead Reduction								
	Array Size		4	9	16	36	64	144	256	512	1024
How to choose T	Beam Coherence		19%	29%	36%	46%	53%	62%	67%	72%	76%
	Outage Probability	$0.5\,\mathcal{R}_{max}$	19%	29%	35%	44%	52%	60%	65%	71%	75%
		$0.95\,\mathcal{R}_{max}$	60%	60%	61%	73%	76%	80%	83%	85%	87%

5.7.2 Choosing the pilot period

Here, we verify our discussion of choosing the *Pilot Period T* using the proposed tracking algorithms ML$_{CD}$, and ML$_D$ since these algorithms are modeled on the concept of beam coherence. The assumptions that we assumed in Section 5.7.1 still hold. In addition, we assume $\phi_0 = \pi/2$, $Q = 10^3$, the frame length $T_{LR} = 100$ ms, and SNR/antenna element 8 dB. Finally, the average drop in the SNR $\mu_\zeta = 0.5$ at time T_{LR}, the outage probability $P_{out} = 0.05$, and a fixed rate $\mathcal{R}_f = \delta\,\mathcal{R}_{max}$ as a factor of the maximum rate $\mathcal{R}_{max} = \log_2(1+\rho)$. Our performance metrics are: (1) the CDF of the received SNR and the achievable rate , and (2) the effective achievable rate.

First, we numerically investigate the pilot overhead reduction, as shown in Table 5.1. We compare the overhead reduction for different array sizes by choosing the *pilot period T* either by the beam coherence or outage probability definitions. The overhead reduction increases with the array size, and this comes from the fact that for a small array size, the beam is wide, and the ML$_D$ can cope with channel variation with a *pilot period* comparable to ML$_{CD}$. Yet, for a large array size, the beam coherence time becomes much smaller, and the *pilot period* becomes smaller for a ML$_D$, which gives the advantage to the ML$_{CD}$. Increasing the rate to $0.95\mathcal{R}_{max}$, imposes the tracking algorithms to sustain higher received SNR, which can be maintained by decreasing the *pilot period.* The ML$_{CD}$ algorithm can sustain a higher rate with a very comparable *pilot period* used at the lower rate. On the contrary, the ML$_D$ needs

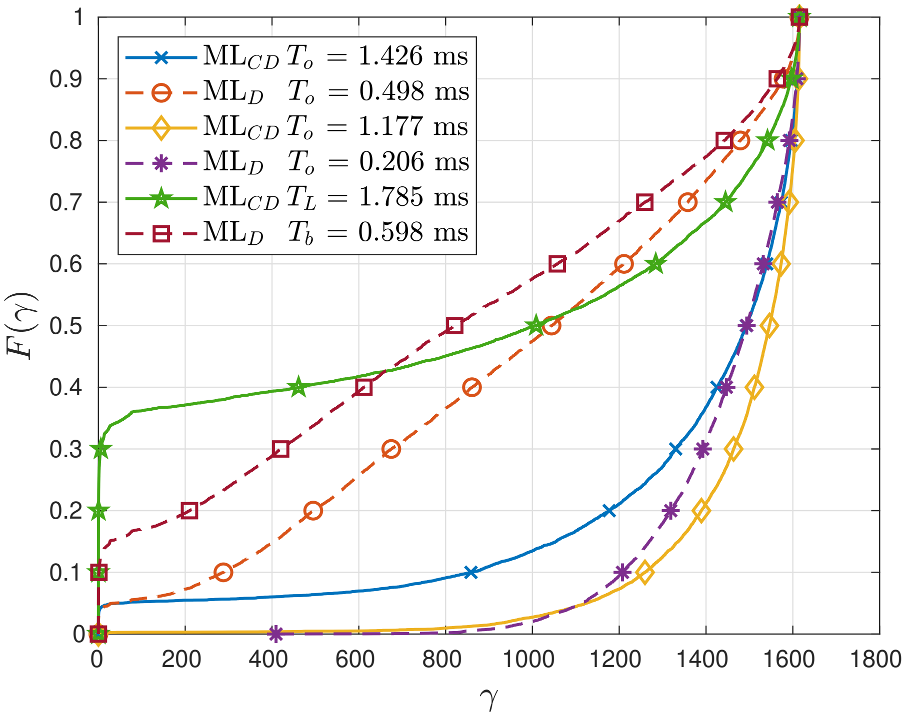

Figure 5.14: CDF of the Received SNR

to reduce the *pilot period* too much. This can be noticed from Table 5.1, where the overhead reduction is increased even for the small array sizes. Finally, the overhead reduction for beam coherence and the outage probability with the rate $\mathcal{R} = 0.5\mathcal{R}_{max}$ are almost the same, but both have different *pilot periods*.

Now, we consider the CDF to compare between the two proposed methods of choosing the *pilot period* T. In Fig. 5.14, we present the CDF of the received SNR for array size $N = 256$ for three different cases: (1) outage with $\mathcal{R}_f = 0.5\,\mathcal{R}_{max}$ (2) outage with $\mathcal{R}_f = 0.95\,\mathcal{R}_{max}$ (3) beam coherence with $\mu_\zeta = 0.5$. For case 1, with *pilot period* $T_o = 1.426$, and 0.498 ms for ML$_{CD}$, and ML$_D$ respectively. It is clear ML$_{CD}$ outperforms the ML$_D$, where it can maintain SNR up to 600 for the same outage probability. Case 2, with *pilot period* $T_o = 1.177$, and 0.206 ms still shows superiority in terms of SNR but not significant as in case 1. However, the pilot

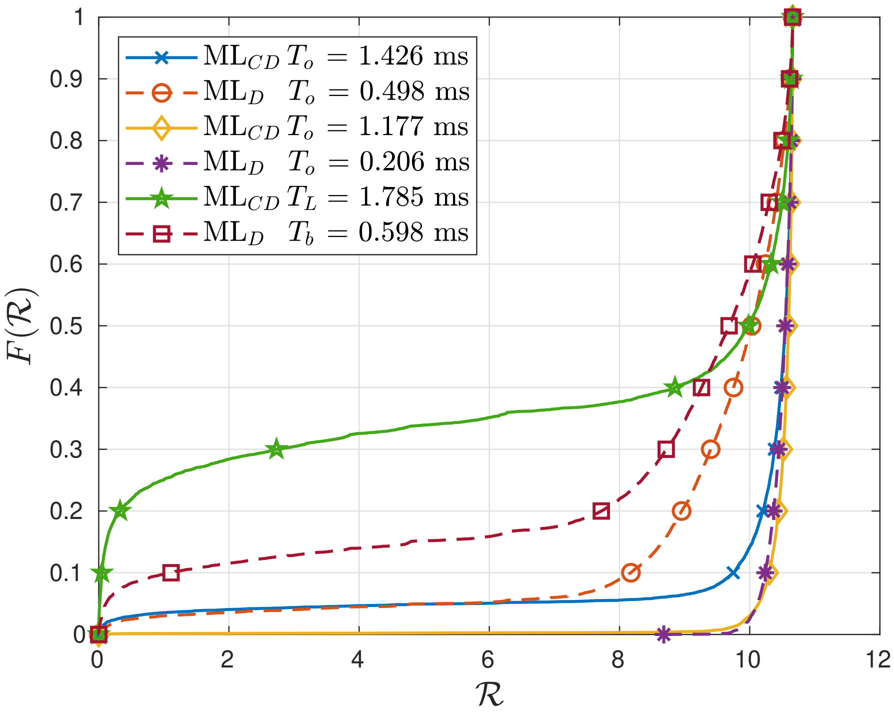

Figure 5.15: CDF of the Achievable Rate

overhead reduction is significantly increased in case 2 to 83% instead of 65% as in case 1. Case 3 shows that both ML_{CD} and ML_{D} nearly have the same average SNR as designed but the ML_{D} has lower probability for the smaller SNR values. Albeit, choosing the *pilot period* by the beam coherence method aimed to have the same average drop in the SNR, but the ML_{CD} is more likely to have lower SNR values in that case due to additional errors caused by estimating the slope variations rather than the AoA estimation errors.

Fig. 5.15, involve the three cases in Fig. 5.14 but in terms of the achievable rate. We can see that for case 1, $P_{out} = 0.05$ is satisfied for both ML_{CD}, and ML_{D} at the 50% of the maximum rate. Moreover, the ML_{CD} surpass the ML_{D} roughly by 4 bps/Hz for the same outage without reducing the *pilot period*. For case 2, both ML_{CD}, and ML_{D} are nearly the same with minor advantage to the ML_{CD} at the higher rate. Similar to our discussion for Fig. 5.14, ML_D obligated to reduce its *pilot period* by almost 59% to support $0.95\,\mathcal{R}_{max}$ instead of $0.5\,\mathcal{R}_{max}$ while ML_{CD} only reduce its period by 17%. Case 3, shows both algorithms can have $P_{out} = 0.05$ but only for a very small rate. Still we can notice an advantage to ML_D in terms of outage probability since we force both algorithms to drop to the same level which worsen the situation of the ML_{CD} due to additional slope variations errors. From our discussions about Fig. 5.14, and 5.15, we can say that its better to choose the *pilot period* based on the outage probability definition due to:(1) the beam coherence method is not directly related to the operational rate and the outage probability (2) the beam coherence method is not a fair choosing method especially if an additional estimation errors exists in the ML_{CD}.

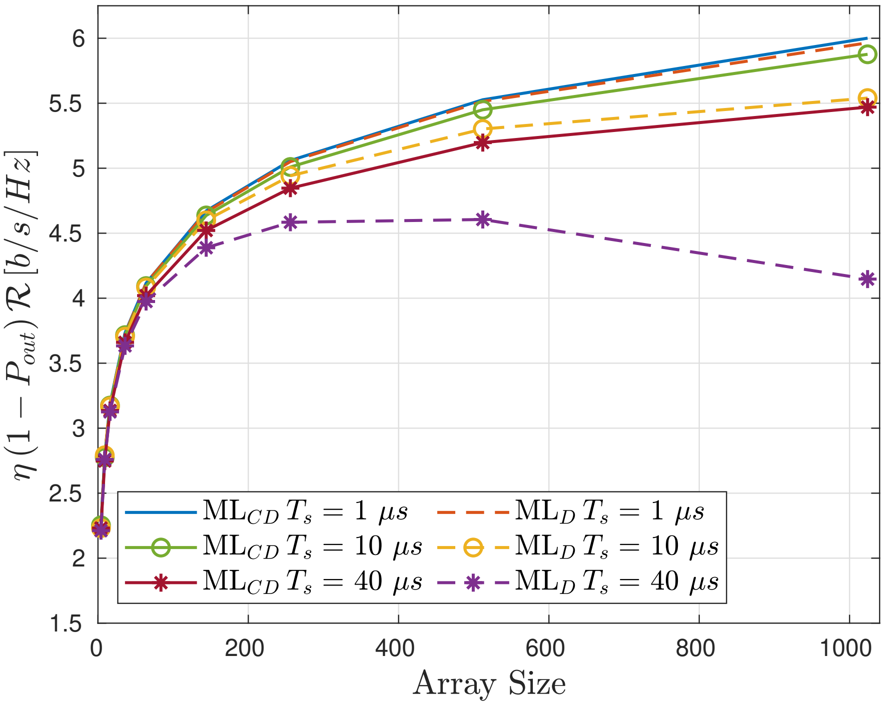

Figure 5.16: Achievable Rate for $P_{out} = 0.05$ and $\mathcal{R}_f = 0.5\,\mathcal{R}_{max}$

Up to this point, we have argued the overhead reduction. Now, we measure the performance of the ML_{CD} in terms of the effective rate given by Eq. (5.31) when the achievable rate $\mathcal{R}_a$ is either the outage rate $(1 - P_{out})\mathcal{R}_f$ or the average rate $\mathbb{E}[\mathcal{R}]$. First, for the effective outage rate as shown in Fig. 5.16, the ML_{CD} outperforms the ML_D for all pilot training intervals values. Moreover, we can notice that ML_{CD} is more resilient to discontinuities such that it reduced only by 0.5 bps/Hz for 1024 array element. On contrary, the ML_D is more sensitive to pilots disruptions causing a rate drop by 2 bps/Hz for $T_s = 40\,\mu s$.

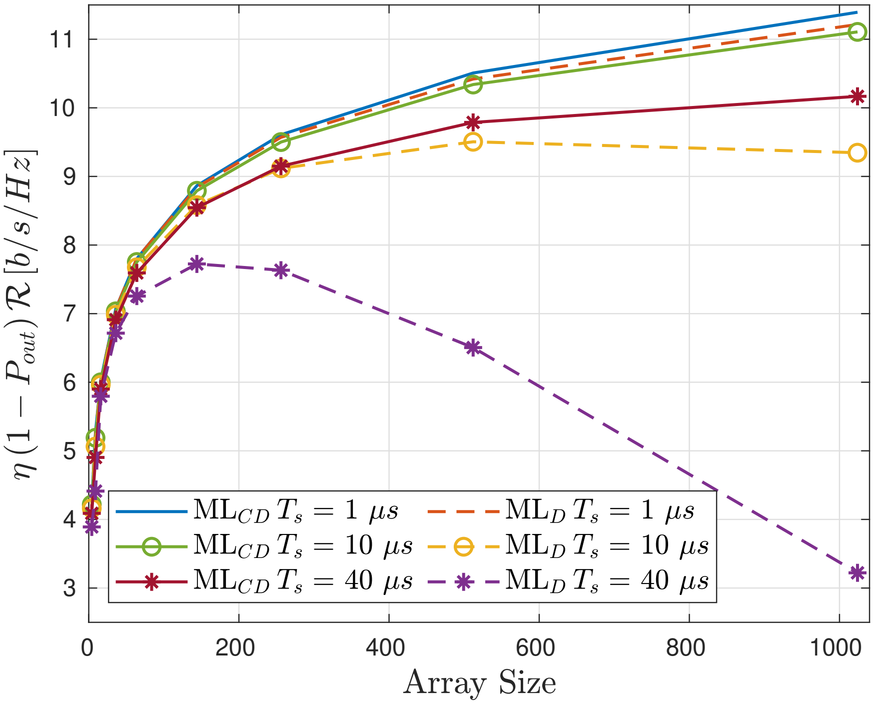

Figure 5.17: Achievable Rate for $P_{out} = 0.05$ and $\mathcal{R}_f = 0.95\,\mathcal{R}_{max}$

Increasing the operational rate to $0.95\,\mathcal{R}_{max}$ increases the pilot overhead reduction which gives the advantage to the ML_{CD} algorithm as shown in Fig. 5.17. This makes

ML$_{CD}$ to surpass the ML$_D$ by 0.25 bps/Hz for the smallest pilot training interval $T_s = 1\,\mu s$. Moreover, ML$_{CD}$ has a rate drop by nearly 1 bps/Hz for $T_s = 40\,\mu s$ while ML$_D$ suffers a rate drop up to 8 bps/Hz. Finally, the higher pilot disruptions makes the efficiency slope decreases too fast, and in that case the array gain is not able to compensate. This noticed for the ML$_D$ with $T_s = 40\,\mu s$, where the rate begins to drastically drop instead of increasing with the array size.

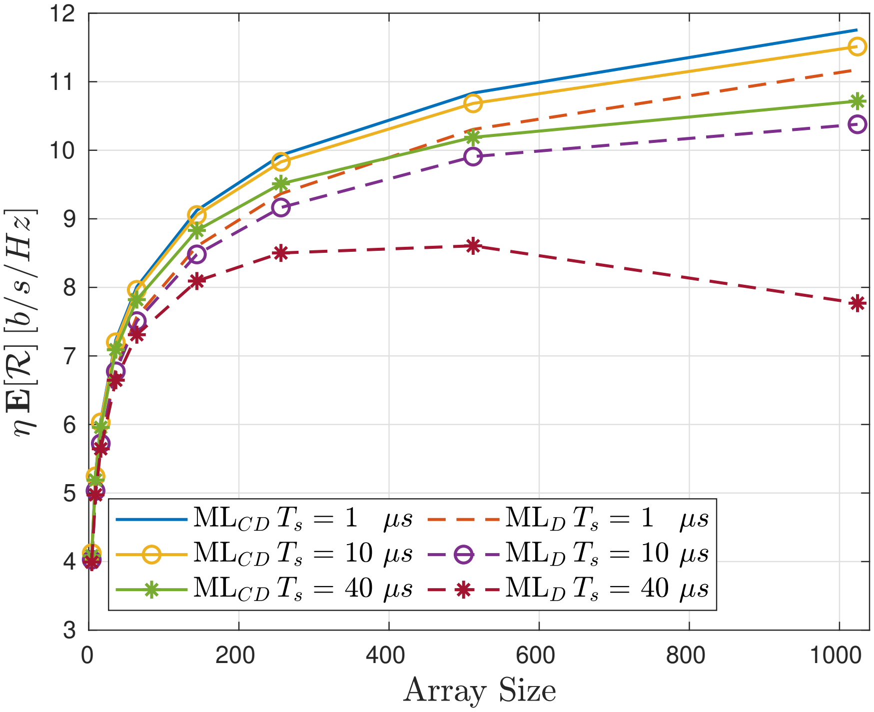

Figure 5.18: Average Achievable Rate for $P_{out} = 0.05$ and $\mathcal{R}_f = 0.5\,\mathcal{R}_{max}$

Now, we consider the effective average achievable rate as shown in Fig. 5.18, and Fig. 5.19. as a verification way of the Continuous-Discrete advantage. Not only the ML$_{CD}$ gain from the overhead reduction or higher efficiency, but also it is more likely to have the higher received SNR than ML$_D$. The average rate is more significant in

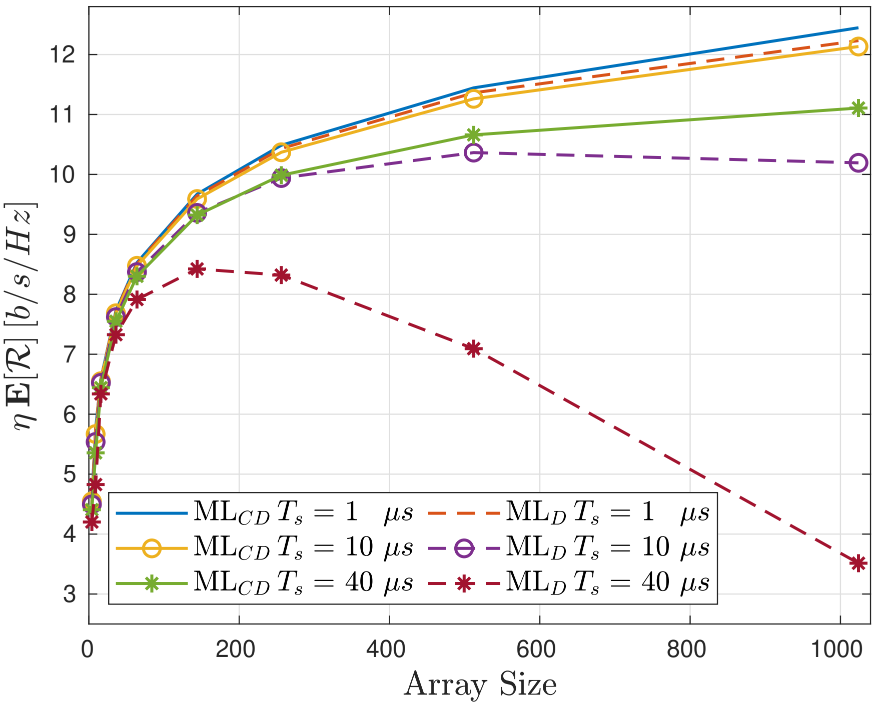

Figure 5.19: Average Achievable Rate for $P_{out} = 0.05$ and $\mathcal{R}_f = 0.95\,\mathcal{R}_{max}$

case of $0.5\,\mathcal{R}_{max}$ than $0.95\,\mathcal{R}_{max}$ since in the later case both algorithm are expected to operate near the edge of the maximum rate. This makes the average of both algorithms to be almost the same.

Partially, we have assumed fixed T_{LR} for both approaches. Two more scenarios can be considered when both approaches are assigned the same *pilot period* and that period is designed for; (1) the Discrete tracking algorithms and (2) the Continuous-Discrete tracking algorithms. In these two scenarios, the Continuous-Discrete tracking algorithm will have longer T_{LR} than the Discrete algorithm.

5.8 Summary

Beam tracking is crucial for maintaining the quality of established links and avoiding the high-cost initial link establishment process. Traditional solutions for the beam tracking problem rely on discrete measurement updates which occur at the instances of pilot signal arrival. By nature, such an approach ignores the information on the first order variation of the beams in between channel measurements. On the contrary, by considering the continuous nature of channel variation over time, a smarter beam tracking solution should exploit the gradual beam variation, and thus attempt to continuously and actively adjust the beam directions even when no measurements are available. This can be achieved by deriving a continuous state transition model for the channel.

In this chapter, we propose a "Continuous-Discrete" beam tracking solution, which exploits system information like the first derivative of the beam angles, to allow continuous beam updates while still relying on discrete measurements. Our solution requires less frequent pilot symbols (less overhead) while maintaining similar tracking performance to discrete tracking, and it can achieve much better performance if the pilot frequency is kept the same. The performance is studied under different SNR levels, array sizes, pilot periods, and different array configurations, i.e., ULA and UPA. We show that our Continuous-Discrete solution outperforms Discrete tracking algorithms in terms of overhead reduction. We also show that increasing the array size for fixed SNR and pilot period increases the tracking accuracy as long as the pilot period is comparable to the beam coherence time.

Another interesting result we show is that larger MIMO arrays do not necessarily lead to improved beam tracking performance. This is due to (1) shorter beam coherence time, and (2) higher link disruption (more frequent pilot symbols), especially for pilot training time in tens of microseconds. Furthermore, we demonstrate that in certain situations, uniform planar arrays may provide improved beam tracking performance over ULAs of similar size, in terms of average SNR, due to longer beam coherence time.

CHAPTER 6

HIGH-RESOLUTION ANALOG FAST BEAM DISCOVERY

6.1 Introduction

In this chapter, we propose a novel beam discovery approach that utilizes both the amplitude and the phase of the received signal to estimate the beam direction. In contrast to traditional beam discovery approaches, which mainly measure all or a sector of the angular space using narrow beams to estimate the beam direction based on the highest RSS, our approach uses both the phase and the RSS to reduce the overhead. Our solution, which we call Main-Lobe Fast Beam Discovery (ML-FBD), leverages a tractable mapping function from the beam direction to the beam amplitude to reduce the number of measurements needed to discover the beams at a given accuracy [18]. The proposed framework is discussed in detail in Section 6.4. Our proposed ML-FBD rely on a low number of channel measurements to preserve accurate beam discovery. Reducing the number of channel measurements minimizes the overhead of pilot symbols to perform such measurements. We consider the same model introduced in Chapter 4, where the notations and the channel model are described in Sections 4.1 and 4.2, and the specific assumptions in Section 4.3.1.

Following this introduction, we provide a motivating example to elaborate on the

Main-Lobe beam discovery approach in Section 6.2. Section 6.3 introduces the problem statement, and Section 6.4 demonstrates the Main-Lobe Fast Beam Discovery approach. Section 6.5 provides a criterion to evaluate and find the number of pilot symbols required for beam discovery. Section 6.6 reveals the numerical results, and Section 6.7 summarizes this chapter.

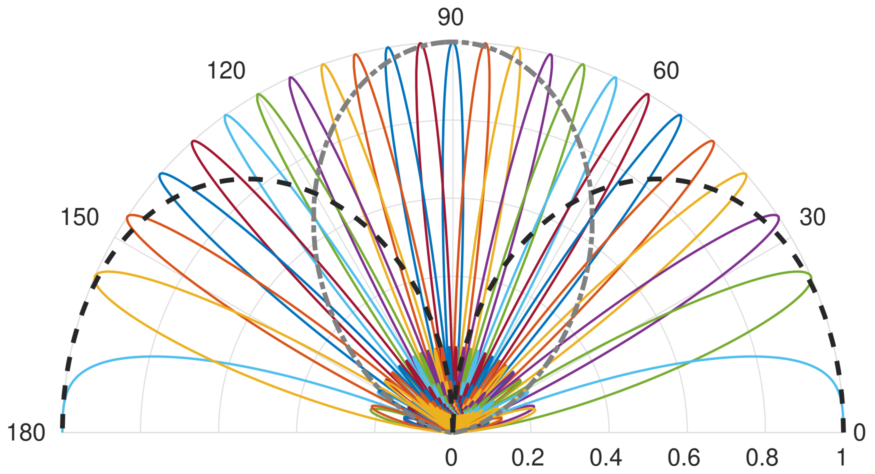

Figure 6.1: Beam sweeping for ULA of sizes 24 (solid) and 2 (dashed)

6.2 Illustrative Example

For a clear view of the proposed idea, we introduce the following example: consider a communication system with a single antenna element at the TX ($N_t = 1$) and $N_r = 24$ antenna elements at the RX. Therefore, we have a Single Input Multiple Output (SIMO) with a channel vector $\in \mathbb{C}^{24\times 1}$. In that case, the RX has 24 resolvable angular bins, which can be represented by the equally spaced beam patterns, as shown in Fig. 6.1. Traditionally, TX/RX exhaustively searches the angular space

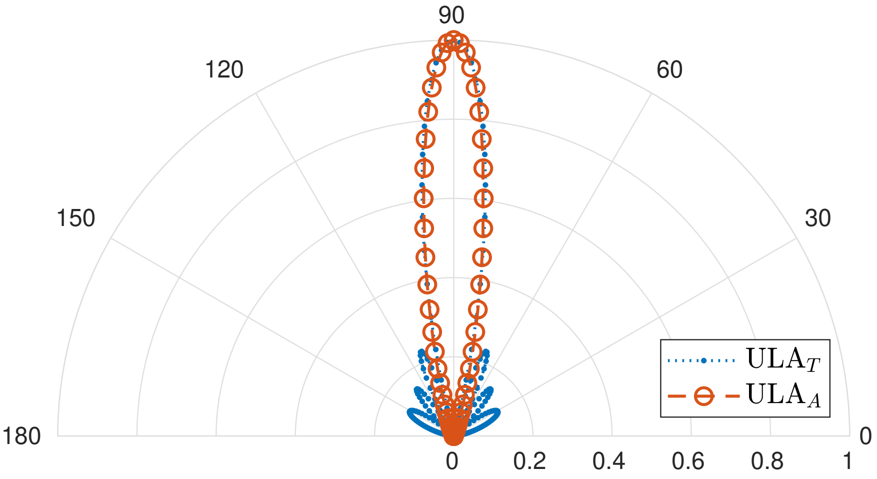

Figure 6.2: Beam Pattern Approximation for 8-element ULA

with narrow beams to find an estimate of the beam direction with minor misalignment. This costs the communications system a significant number of pilot symbols, degrading the effective spectral efficiency. Still, the hierarchical solutions [33–36] have done an excellent job by narrowing down the search space. However, these solutions only consider the relative RSS of obtained measurements and neglect the phase information.

In our approach, we still use hierarchical beams to perform measurements, but in addition, we exploit the beamforming gain function defined as:

$$\left|\bar{h}(\phi, \bar{\phi})\right| \triangleq e^{-\frac{N^2}{2}[\cos(\phi)-\cos(\bar{\phi})]^2} \tag{6.1}$$

where $\bar{\phi}$ is the beam direction, while ϕ is the AoA. During the measurement process, the receiver knows $\bar{\phi}$ and can estimate $\bar{h}(\phi, \bar{\phi})$, from which the receiver can work out the value of ϕ. This is performed only on the beam with the strongest RSS, and it gives a more accurate estimate of ϕ, unlike the traditional solutions, which consider $\bar{\phi}$ of the beam with the strongest RSS to be the best estimate of ϕ. Nonetheless, the beamforming gain function has a challenging formula (will be detailed later in Eq. (4.9)), which makes it difficult to solve for ϕ. Hence, an approximation of the main lobe is used, which is given by Eq. (6.1) and shown in Fig. 6.2.

The key idea of the proposed approach can be demonstrated as follows: (1) We use a subarray of size $N_o = 2$ to form wide beams to scan the angular space as shown in Fig. 6.1. This requires only two measurements (with $\bar{\phi}_1 = 0$, and $\bar{\phi}_2 = \pi/2$) instead of 24 measurements. (2) We choose the direction with the highest RSS. Then, we use Eq. (6.1) to find an estimate of the true beam direction. (3) However, Eq. (6.1) does not provide a unique solution, but two solutions, which we define as $\hat{\phi}_+$ and $\hat{\phi}_-$. (4) Leveraging the phase information of the channel measurement ($\angle\bar{h}(\phi, \bar{\phi}_2)$, if $\bar{\phi}_2$ is chosen in step (2)). We pick the estimate as:

$$\hat{\phi}^\star = \underset{\hat{\phi}\in[\hat{\phi}_-, \hat{\phi}_+]}{\operatorname{argmin}} \left|\angle\bar{h}(\phi, \bar{\phi}_2) - \angle\bar{h}(\hat{\phi}, \bar{\phi}_2)\right| \tag{6.2}$$

Now, we provide a numerical example under different array sizes to show how significantly we can reduce the number of channel measurements. To that end, we do not consider the noise, the complex-path gain, or the main-lobe approximation errors. In this example, we are neglecting the noise and path gain effect, and then the normalized channel measurement can be represented by Eq. (6.1). Therefore, we only face the approximation error, which can be ignored by increasing the array size. In Fig. 6.3, we assume two receivers with different subarray sizes, $N_o = 2$, $N_o = 16$. The figure shows the average SNR under different array sizes. The solid line is the SNR limit when a perfect alignment is assumed, while the coarse stage (C $N_o = 2$, $N_o = 16$), where each receiver consumes 2 and 16 pilot symbols, respectively. Firstly, the receiver with $N_o = 2$ performs poorly in the coarse stage due to approximation error. Adding one more pilot symbol as a refinement improves the performance to

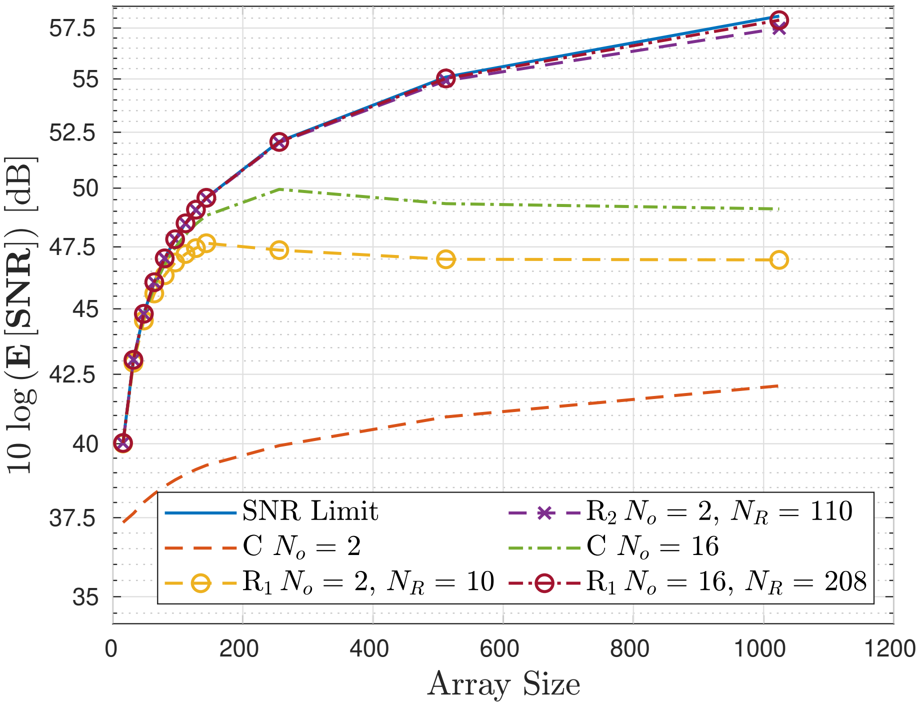

Figure 6.3: SNR of the proposed approach with two different subarray sizes, i.e., 2, 16

cover a receiver with a full array size of nearly up to 200. The second refinement pilot significantly improves the performance to include array sizes up to 1024. In each refinement stage, the number of antenna elements (concatenated subarrays), i.e., N_R, is chosen based on the squared error of the previous stage, which will be discussed later. Increasing the subarray size reduces the approximation error and improves the performance correspondingly. It is clear when $N_o = 16$, where the coarse stage covers up to 256, and a single refinement pilot covers up to 1024 and more.

Here, we show that we need to consume only four pilot symbols to find beam direction with a high resolution (small estimation error), which is essential for a TX/RX with large-scale array size. Albeit this outstanding performance and the great pilot overhead reduction, we need to consider the noise and the complex path gain effects. Modeling those factual wireless channel assumptions exacerbates the situation and forces the need for either additional refinement of pilot symbols or the transmitted SNR.

6.3 Problem Statement

The following sections follow the system model introduced in Chapter 4, especially the specific assumptions in Section 4.3.1. In the beam discovery stage, the problem is choosing the beamforming vector that maximizes the SNR. The same beamforming vector maximizes the beamforming gain. Then we can write the problem as follows:

$$\boldsymbol{w}^{\star} = \underset{\boldsymbol{w} \in \mathcal{F}}{\arg\max} \left| \boldsymbol{w}^{\dagger} \, \boldsymbol{a}_R(\phi) \right|^2 , \tag{6.3}$$

where $\mathcal{F} \in \mathbb{C}^{N \times J}$ is the set of the beamforming vectors, and $\mathcal{F} = \{\boldsymbol{w}_1, \boldsymbol{w}_2, \cdots, \boldsymbol{w}_J\}$. As the array size increases, the resolution of estimating the beam direction should increase. This increases $|\mathcal{F}|$, which means a large number of channel measurements, and this pilot overhead degrades the spectral efficiency.

6.4 Main-Lobe Fast Beam Discovery

A brief overview of the proposed approach is shown in Fig. 6.4, where we start by estimating the complex path gain using K of pilot symbols. After that, a coarse beam sweeping utilizes $\widetilde{N}_P$ to find an initial estimate of the beam direction. Based on the accuracy of the initial estimate, we determine whether a refinement of that estimate is needed or not. The refinement stage can be repeated until a threshold accuracy is achieved. In the following, we will discuss the basic idea and clarify each step in that flow chart.

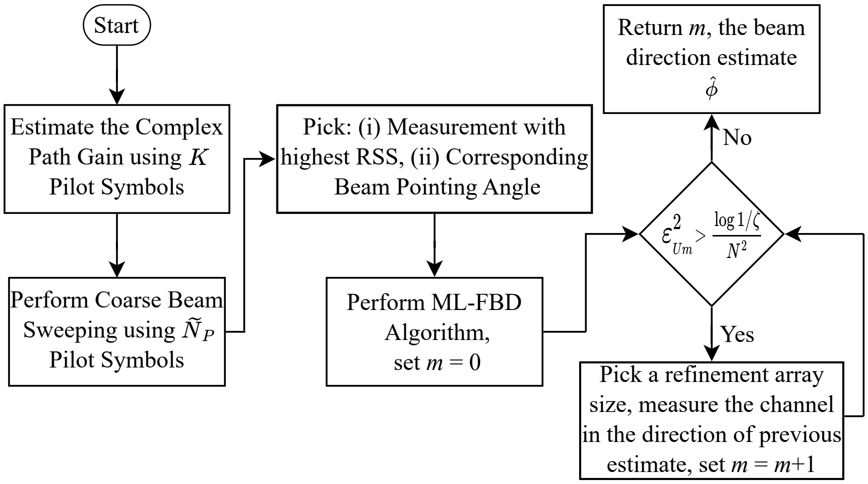

Figure 6.4: Flow chart for the proposed ML-FBD approach.

Now, recall Eq. (4.8), which describes the received symbols, and using Eq. (4.9), we get:

$$y_k = \alpha h\left(\phi, \bar{\phi}_k\right) + \acute{n}_k. \tag{6.4}$$

We try to solve Eq. (6.4) for the AoA ϕ directly. To do that, let us assume that we have a perfect estimate of α and that we can filter out the noise term, which becomes much easier in a high SNR regime. In this case, we have an estimate of $h\left(\phi, \bar{\phi}_k\right)$, and the unknown becomes the AoA ϕ.

However, ϕ is an implicit variable, and attempting to solve Eq. (6.4) proves to be very challenging since $h\left(\phi, \bar{\phi}\right)$ is a summation of exponentials, which makes it challenging to isolate ϕ. In addition, α is unknown beforehand, creating another challenge.

In the remainder of this section, we describe how we achieve our goal of solving Eq. (6.4) using a two-stage solution: First, we estimate the path gain, α. Second, we present an algorithm called *Main-Lobe Fast Beam Discovery* to find ϕ.

6.4.1 Complex Path Gain Estimator

To find an estimate of the path gain, we use a single antenna element ($N = 1$), which reduces the beamforming gain to 1. Hence, Eq. (6.4) is reduced to

$$\tilde{y}_k = \alpha + \acute{n}_k, \tag{6.5}$$

where $\alpha \sim \mathcal{CN}(0, 1)$, with a unit variance to ensure unit power channel coefficients, i.e, $\mathbb{E}[|\alpha|^2] = 1$. The Minimum Mean Squared Error (MMSE) estimate of α is found by [69] as:

$$\begin{aligned} \hat{\alpha} &= \frac{1}{K + 1/\rho} \sum_{k=1}^{K} \alpha + \acute{n}_k \\ &= \frac{\rho}{K\,\rho + 1} \sum_{k=1}^{K} \alpha + \acute{n}_k \\ &= \frac{\rho}{K\,\rho + 1} \left[K\,\alpha + \mathcal{V}\right], \end{aligned} \tag{6.6}$$

where K is the total number of measurements used to average the estimate. Note that $\rho = \rho_a$ for a single antenna element. Also, $\mathcal{V} \sim \mathcal{CN}(0, K/\rho)$, $\hat{\alpha} \sim \mathcal{CN}(0, \sigma^2_{\hat{\alpha}})$ and the MSE associated with $\hat{\alpha}$ is $\frac{1}{1 + K\,\rho}$, which converges to zero as K increases.

We are interested in the number of channel measurements needed to estimate the complex path gain, i.e., K. As we see, increasing K improves the MMSE estimator performance (i.e., decreasing the MSE). In order to have a finite number of channel measurements, let the target MSE be β. Then, the number of channel measurements required to evaluate the MMSE estimator is given by:

$$K = \left\lceil \frac{1 - \beta}{\rho\,\beta} \right\rceil. \tag{6.7}$$

Now that we have knowledge of the path gain through K measurements, the remaining $N_P - K$ measurements will be used to find the beam direction. To further simplify the notation, let us normalize Eq. (6.4), with respect to $\hat{\alpha}$, as follows:

$$\bar{y}_k = \delta\, h\left(\phi, \bar{\phi}\right) + \bar{n}_k, \tag{6.8}$$

where $\delta = \dfrac{\alpha}{\hat{\alpha}}$ is the path gain equalization error, while the noise term becomes $\bar{n}_k = \dfrac{\acute{n}_k}{\hat{\alpha}}$, where $\bar{n}_k | \hat{\alpha} \sim \mathcal{CN}(0, 1/(\rho\, |\hat{\alpha}|^2))$.

6.4.2 Main-Lobe Fast Beam Discovery

Overview: Recall Eq. (6.4), and let us assume we have perfectly estimated $h\left(\phi, \bar{\phi}_k\right)$. Then, we are ready to solve Eq. (4.9) for ϕ. Nonetheless, $h\left(\phi, \bar{\phi}\right)$ is a complex formula, which makes it difficult to find a closed-form solution for ϕ. In addition, even if such a solution existed, that solution is not unique. In fact, if we only consider the magnitude of the measurement, then by visual inspection of Fig. 6.1, we see that beam patterns may have up to $2N$ nulls. Hence, up to $2N$ solutions for ϕ may exist. However, if we limit the solution range to the main lobe of the beam above the intersection points with the neighboring beams, then only two solutions may exist. Furthermore, by exploiting the phase of the measurement, we can find one unique solution. We will use the latter observation in the algorithm we present here.

Our solution relies on two steps. In the first step, we try to find the beam whose main lobe contains the channel path. Then, owing to the complexity of $h\left(\phi, \bar{\phi}\right)$, we instead exploit the main-lobe approximation formula given by Eq. (6.1). This makes solving for ϕ significantly easier, in addition to forcing the solution to be confined to the main-lobe we are focusing on. Eq. (6.1) is easy to solve analytically, and we can retrieve the beam direction using the amplitude and the phase of the channel measurement.

Algorithm 2 Main-Lobe Finding AoA/AoD

```
Input: $\bar{\phi}$, and $\bar{y}$
Output: $\hat{\phi}$
$\hat{h}(\phi, \bar{\phi}) = \frac{\rho}{\rho + 1}\bar{y}$, $\varphi = \angle\hat{h}(\phi, \bar{\phi})$, and $\bar{\Omega} = \cos(\bar{\phi})$
$\hat{\phi}_{\pm} = \arccos\left(\left[\bar{\Omega} \pm \sqrt{-\frac{2}{N^2}\ln\left|\hat{h}(\phi, \bar{\phi})\right|}\right]_{-1}^{1}\right)$
$\varphi_{\pm} = \angle h(\hat{\phi}_{\pm}, \bar{\phi})$
if $\varphi = \varphi_{+}$ then
    $\hat{\phi} = \hat{\phi}_{+}$
else
    $\hat{\phi} = \hat{\phi}_{-}$
end if
```

Formal description: Our solution procedure depends on a ***coarse beam search*** followed by ***refinements***. It relies on a single iteration of the Discrete Beam Tracking Algorithm from [18]. We describe it as follows:

Coarse Beam Discovery

(i) We perform a coarse beam sweeping using a single subarray with $N_o = \frac{N}{M}$ antenna elements. Then, we obtain a set of measurements $\mathcal{Y} = \{\bar{y}_1, \bar{y}_2, \cdot\cdot\cdot, \bar{y}_{N_o}\}$, and its corresponding set of beam pointing directions $\mathcal{T} = \{\bar{\phi}_1, \bar{\phi}_2, \cdot\cdot\cdot, \bar{\phi}_{N_o}\}$.

(ii) We initialize Algorithm 2 with the beam pointing direction $\bar{\phi}_C \in \mathcal{T}$ that corresponds to the measurement $\bar{y}_C \in \mathcal{Y}$ with the highest amplitude.

(iii) The estimate of the coarse stage $\hat{\phi}_C$ from Algorithm 2 when initialized with $\bar{\phi}_C$, and $\bar{y}_C$ is too sensitive to noise and path gain equalization error due to the wide beams used at this stage. This lead us to perform a fine stage to reduce the MSE of the true value of the beam direction.

Fine Beam Discovery

Here, We do not consider traditional fine beam sweeping in which a sequence of narrow beams searches all or a sector of the space to precisely detect the beam direction. Instead, we utilize a single narrow beam pointed at the initial estimate $\hat{\phi}_C$ to measure the channel with two or more subarrays to reap from the array gain. Algorithm 2 is then utilized to estimate the fine beam direction, i.e., $\hat{\phi}_F$. This step can be performed several times or not done at all based on some criteria.

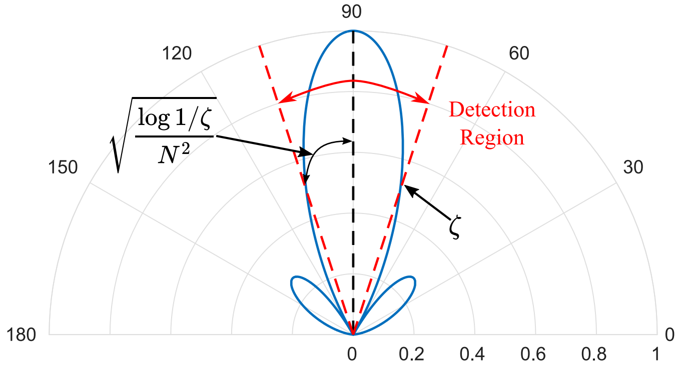

Figure 6.5: Detection region of the beam direction

6.5 Performance Evaluation

Up to this point, we have only introduced our approach. Now, we propose a criteria to evaluate the performance of the proposed approach. We choose the squared-error, i.e., $\mathcal{E}^2 = \left|\Omega - \hat{\Omega}\right|^2$, where $\Omega = cos(\phi)$ is the true angular cosine, and $\hat{\Omega} = cos(\hat{\phi})$ is the estimate angular cosine. From Eq. (6.1), we get the gain of received power as follows:

$$\zeta \triangleq \left|\bar{h}(\Omega, \hat{\Omega})\right|^2 = e^{-N^2 \mathcal{E}^2} \tag{6.9}$$

From Fig. 6.5, we can visualize the criteria we aim to utilize, as shown from the figure if an incoming path lies in the narrow window that satisfies the array gain. We are interested in the squared-error value that causes a power drop ratio by ζ (e.g., 0 dB in the SNR means $\zeta = 1$). In that case, we can represent the squared error as a function of the power drop ratio using Eq. (6.9) as follows:

$$\mathcal{E}^2 = \frac{\log 1/\zeta}{N^2} \tag{6.10}$$

Now, we have the criteria that help us to find the number of fine iterations as mentioned in Section 6.4.2. For example, if we limit the threshold to a 3 dB power drop ratio (i.e., $\zeta = 0.5$) and the array size is $N = 1024$. So, if the squared error of the coarse stage in Section 6.4.2 is upper bounded by $\frac{\log 2}{1024^2} = 6.6 \times 10^{-7}$, then we do not need any fine iterations, and the number of measurements is limited to $N_P = N_o$. Otherwise, we will need to perform one or more fine iterations based on the following theorem.

Theorem 3. *The number of channel measurements $\widetilde{N}_P$ required to find the beam direction is bounded by:*

$$N_o \leq \widetilde{N}_P \leq N_o + \sum_{m=0}^{\infty} \mathbb{1}\left(\mathcal{E}^2_{_{Um}} > \frac{\log 1/\zeta}{N^2}\right), \tag{6.11}$$

where, $\mathcal{E}^2_{_{Um}}$ is the upper bound squared error for the m^{th} iteration, and $m = 0$ denotes the coarse stage. Proof of Theorem 3, and the definition of the upper bound squared error for the m^{th} iteration can be found in Appendix B.1. The squared error bound mainly depends on the array gain. Hence, we need to choose the array size for each iteration carefully. The array size of the coarse stage is the size of a single subarray, $N_o = \dfrac{N}{M}$, while for the m$^{\text{th}}$ iteration is given by:

$$\begin{aligned} N_m &= \underset{N \in L\, N_o}{\arg\min} |N_{req} - L\, N_o| \\ &\qquad\qquad \forall\, L = m+1,\, m+2,\, m+3, \ldots \end{aligned} \tag{6.12}$$

where, $N_{req} = \sqrt{\dfrac{\log 1/\zeta}{\mathcal{E}^2_{U m-1}}}$ is the array size that has an upper bound squared error $\mathcal{E}^2_{U m-1}$, for a ζ power drop.

6.6 Numerical Analysis

In this section, we compare the performance of the ML-FBD to three baselines approaches: (1) Two stages hierarchical (CFH 2 Stages), (2) Hierarchical with adaptive array sizes (CFH Adaptive), where the array size of each fine stage is chosen based on Eq. (6.12). (3) Hierarchical with fixed array sizes (CFH Fixed), where each array size is doubled in each fine stage. We assume the AoA, $\phi \sim U(0, \pi)$, and we average the output over 10^4 simulation runs. Except when stated otherwise, the SNR per each antenna element, $\rho_a = 10$ dB, $\zeta = 1$, $\beta = 0.95$, $N = 1024$ and the number of channel measurements in the coarse stage $N_o = 2$. Our performance metrics are: (1) the average received SNR, and (2) The total number of measurements required to estimate the beam direction, N_P. The performance is evaluated under two decision rules of the refinement stages: (1) *Offline Decision* and (2) *Dynamic Decision*.

Offline Decision means we determine the number of refinements needed and the corresponding array sizes before we start the discovery approach. However, in that case, we need to have the knowledge of the complex path gain distribution, which is assumed as $\alpha \sim \mathcal{CN}(0, 1)$. In contrast, the *Dynamic Decision* means that the number of refinements needed and the number of equipped antenna elements at each

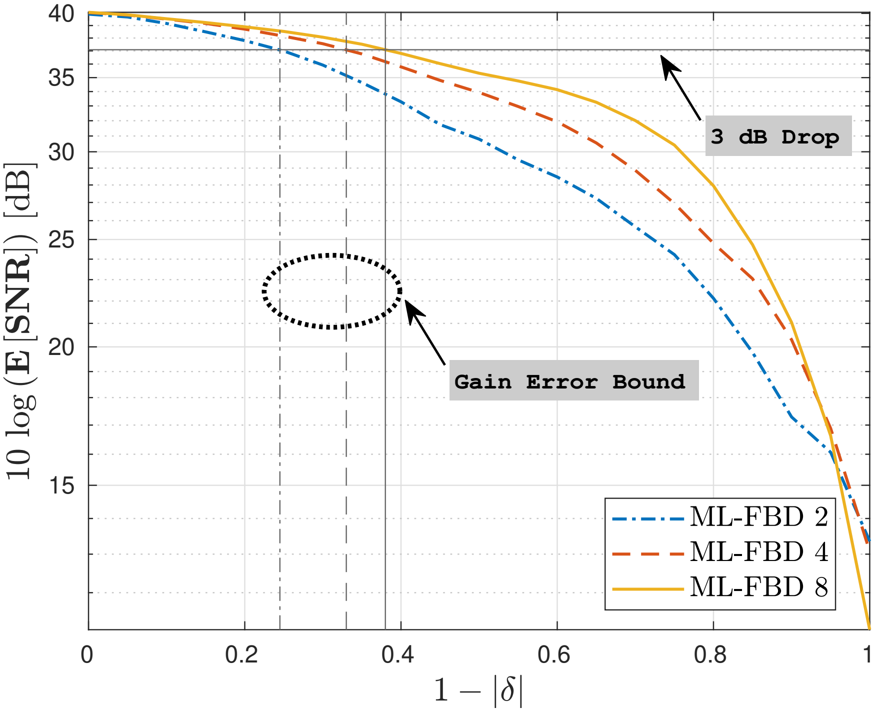

Figure 6.6: SNR against error of path gain amplitude for three different array sizes in the coarse stage, i.e., $N_o = 2$, 4, 8, and the full array size $N = 1024$.

refinement stage are random variables. Finally, in the *Dynamic Decision*, we assume $|h| = 0.6$, which is the intersection point between the overlapped beams utilized at the coarse stage. Also, $|\hat{h}|$ is given from the previous stage.

Offline Decision: First, we decouple the problem of estimating the complex path gain and the problem of beam discovery. We consider two types of error in the path gain equalization error: (1) Error in the amplitude only, i.e., $\angle\delta = 0$, (2) Error in the phase only, i.e., $|\delta| = 1$. Fig. 6.6, shows the first type of error for three different values of N_o. We fix the threshold of SNR drop to be 3 dB, i.e., the path direction stays in the Half Power Beam Width (HPBW). We note that the proposed beam discovery can sustain amplitude drop due to path gain error by 25% for $N_o = 2$ and reach 40% when $N_o = 8$. For a significant drop in the equalization amplitude, i.e.,

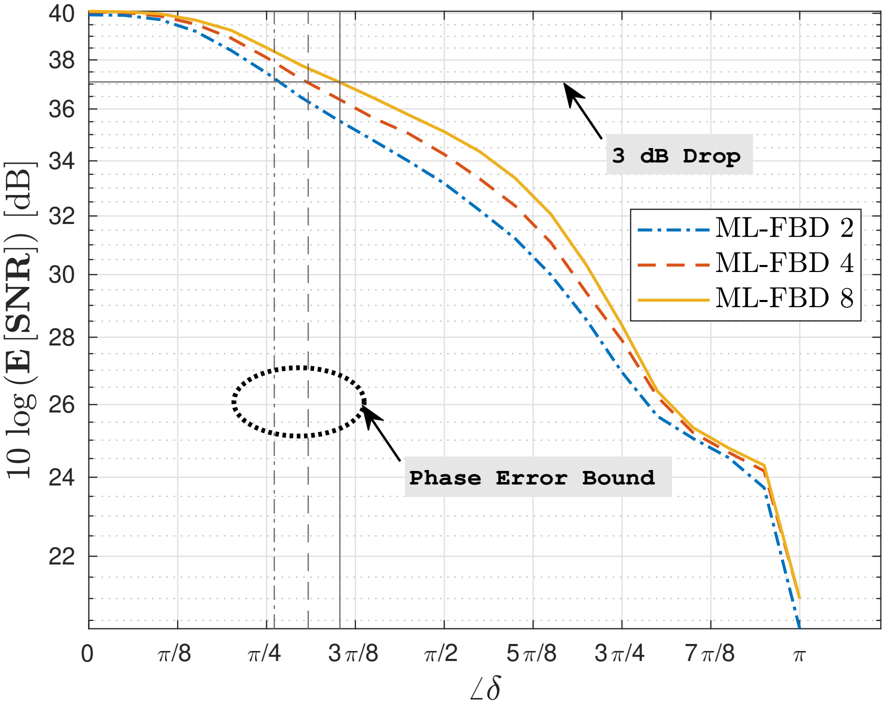

Figure 6.7: SNR against error of path gain phase for three different array sizes in the coarse stage, i.e., $N_o = 2$, 4, 8, and the full array size $N = 1024$.

$|\delta| \approx 0$, increasing the array size in the coarse stage exacerbates the beam discovery performance since narrower beams are more sensitive to errors.

We introduce the second type of error in the Fig. 6.7. The results reveal that the ML-FBD can incur phase error up to $\pi/4$ for $N_o = 2$ and reach $3\pi/8$ for $N_o = 8$. Also, we can notice that the proposed approach is less susceptible to phase errors than amplitude errors.

Now, we compare the proposed ML-FBD to the three proposed baselines of the hierarchical beam sweeping approaches in terms of the SNR under different array sizes, as shown in Fig. 6.8. First, we notice that all approaches sustain an expected SNR beyond the HPBW threshold. Moreover, the zoom-in part shows that sacrificing more pilot symbols in the coarse stage results in better performance. This improvement can be shown by gain results from utilizing 8 pilots instead of 2 pilots for the proposed ML-FBD.

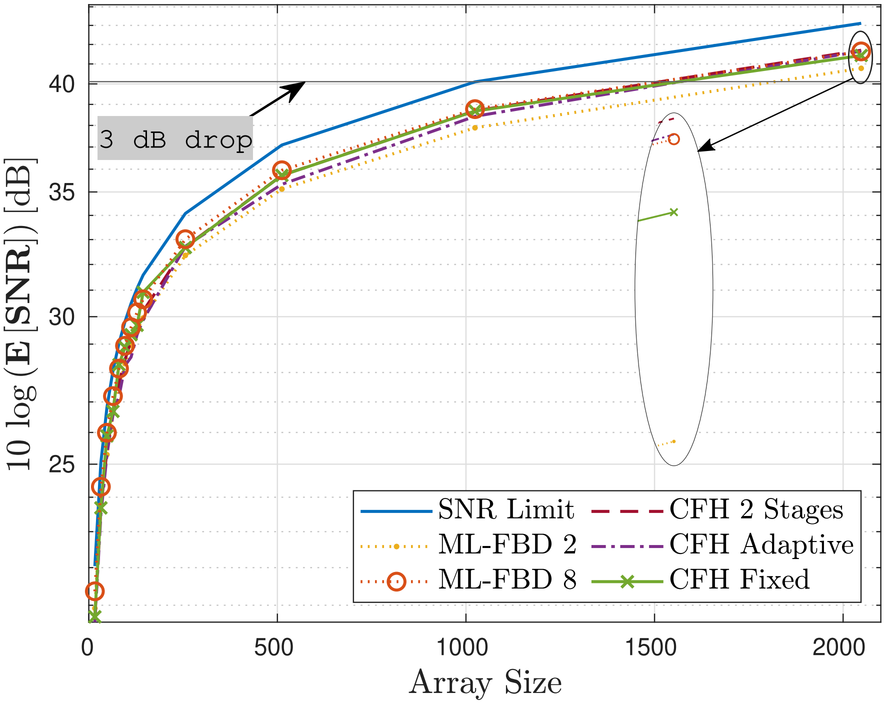

Figure 6.8: SNR for different array sizes under ML-FBD for $N_o = 2,\ 4\,8$, and the Hierarchical approaches for $N_o = 2$.

We present the main advantage of the proposed approach, which is pilot overhead reduction. Fig. 6.9, shows the number of channel measurements exploited to estimate the beam direction. We compare ML-FBD without the overhead incurred by the complex path gain estimation stage to the hierarchical approaches. Also, we present the number of pilot symbols utilized by ML-FBD$_K$ when additional K measurements utilized at the complex gain estimation are added. The proposed ML-FBD roughly utilizes a fixed number of pilot symbols, no matter the array size. We can achieve pilot overhead reduction from the best hierarchical case by 70% for $N = 2048$ array size by excluding the K pilot symbols utilized for estimating the path gain. By adding the overhead incurred to estimate the path gain, we achieve pilot overhead reduction by 62% for 10 dB and reduced to 42% for 5 dB SNR per antenna element.

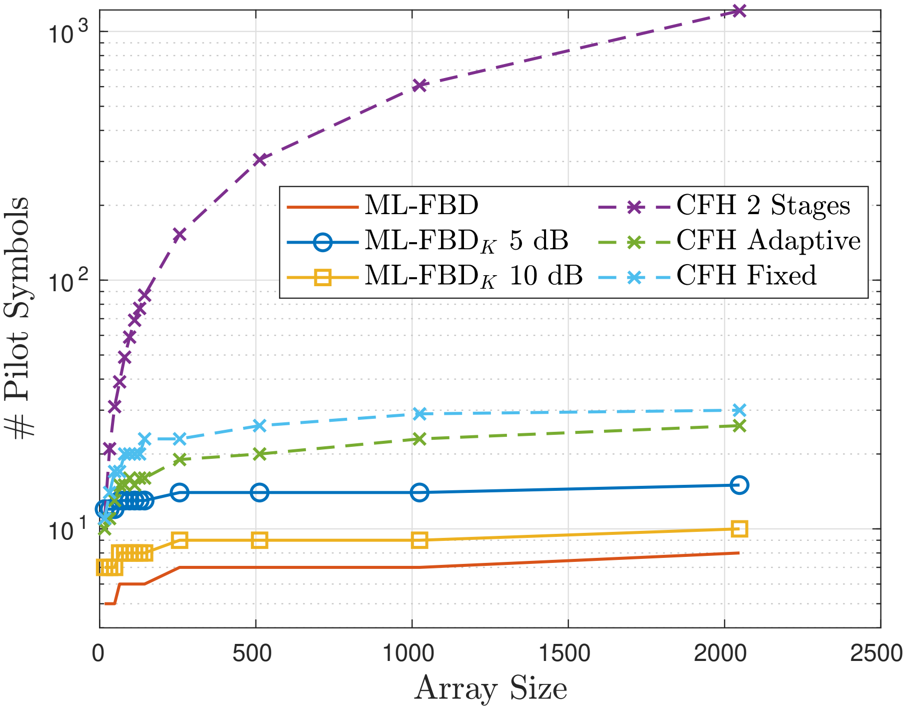

Figure 6.9: Number of pilot symbols for estimating the beam direction under different array size.

Finally, Fig. 6.10 presents the variations in the number of fine stages under different array sizes and the corresponding array sizes (annotated over bars) utilized at each stage. We only need two additional pilot symbols to have similar beam discovery when the array size increases by a factor of 2^7. Furthermore, we can see that the last two stages for each array size have nearly the same performance, which is beyond the HPBW threshold, and the proposed approach needed the last stage with the full array size since we set $\zeta = 1$. This means we forced the algorithm to have a 0 dB drop which is not necessarily happening, and in turn, we reach the full array size in the last stage.

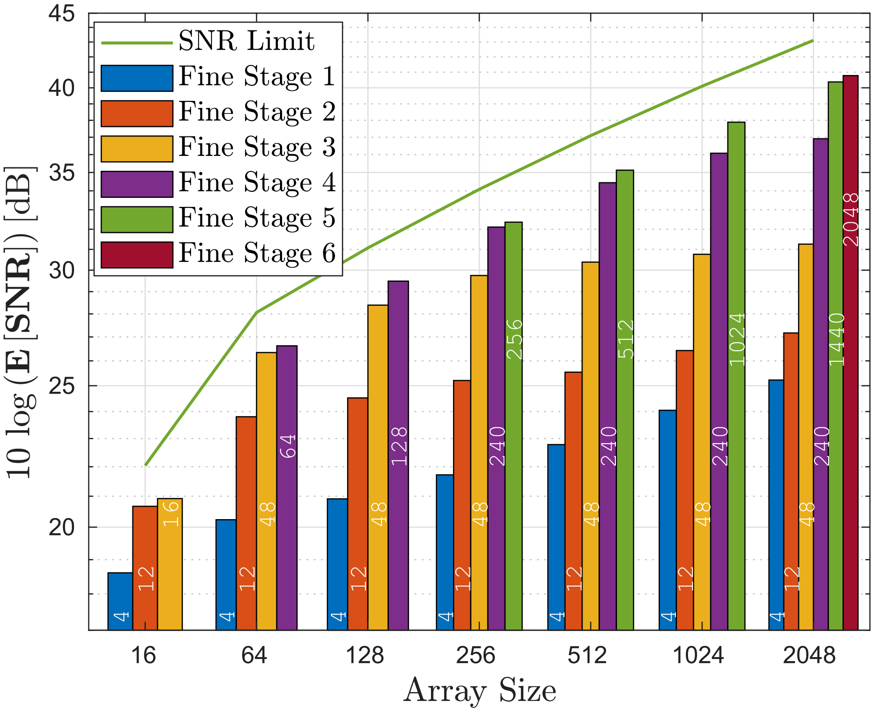

Figure 6.10: SNR for each fine stage of the ML-FBD approach under different array size

Dynamic Decision: Instead of repeating the previous results with the *Dynamic Decision* rule, we are only interested in comparing the two rules in terms of the average number of refinements and the probability of detection. In the following, we assume three different values of K (the number of pilot symbols needed to estimate the complex path gain). Fig. 6.11 depicts the average number of pilot symbols required to find the beam direction. The *Dynamic Decision* rule is more conservative than the *Offline Decision* rule, which consumes more pilot symbols on average.

Moreover, consuming more pilot symbols for estimating the complex path gain (i.e., $K = 2, 3,$ and 4) does not affect the average number of pilot symbols required for beam discovery. However, the K parameter will play a critical role in the probability of detection, which will be discussed in the following.

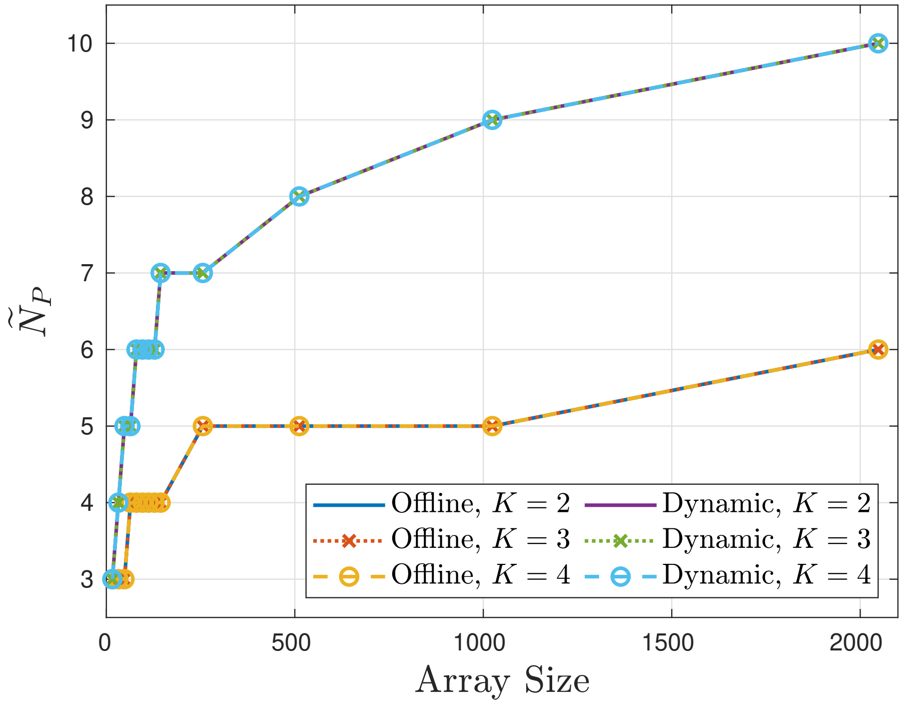

Figure 6.11: Number of pilot symbols under Offline and Dynamic decision rules

Now, we evaluate both decision rules under the probability of detection metric. Fig. 6.12 shows the Cumulative Distribution Function (CDF) of the SNR (including the array gain) of the last refinement stage. The SNR per antenna element is assumed to be 10 dB. The 3 dB drop line is the detection threshold, and above this threshold, we have a detection event, while below the threshold is a misdetection event. The *Dynamic Decision* rule has a higher detection probability since it is more conservative

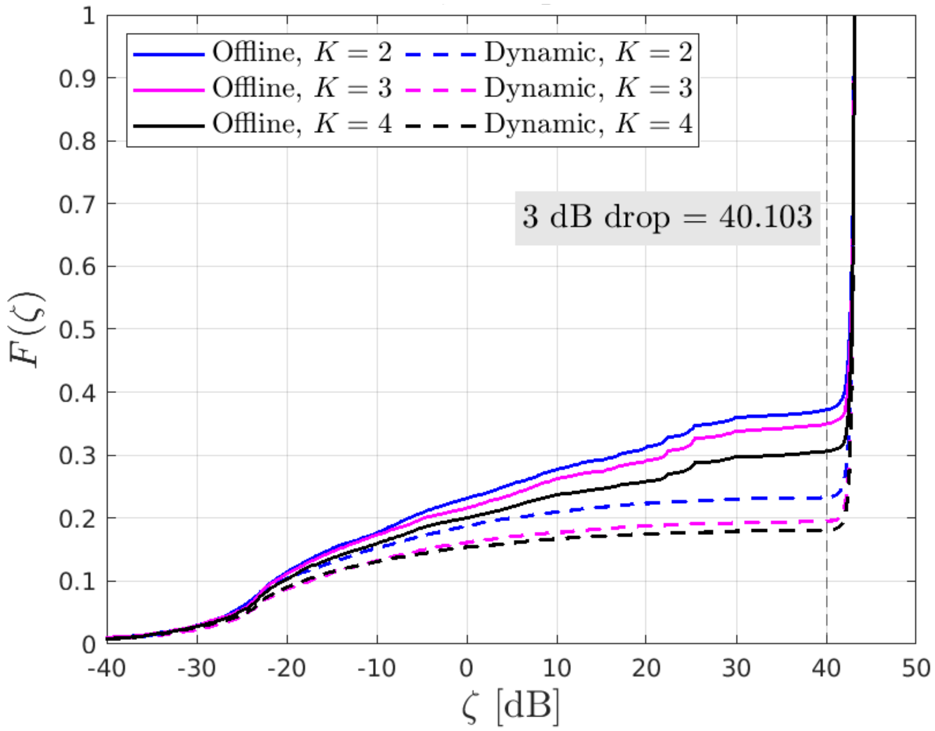

Figure 6.12: CDF of the SNR of the final refinement stage with array size, $N = 2048$

than the *Offline Decision* rule. Furthermore, the K parameter affects the detection probability for both rules, where increasing K improves the path gain estimation, improving the beam discovery performance.

Moreover, increasing the SNR per antenna element improves the detection probability for both rules. In Fig. 6.13, we assume 15 dB per antenna element and $K = 2$. We notice that by increasing the SNR by 5 dB, the probability of detection is increased by 20% for both rules. Although both rules have different detection probabilities, both cases achieve average SNR above the 3 dB drop threshold, where the average SNR is 46.99 dB and 47.51 dB for *Offline* and *Dynamic* rules, respectively.

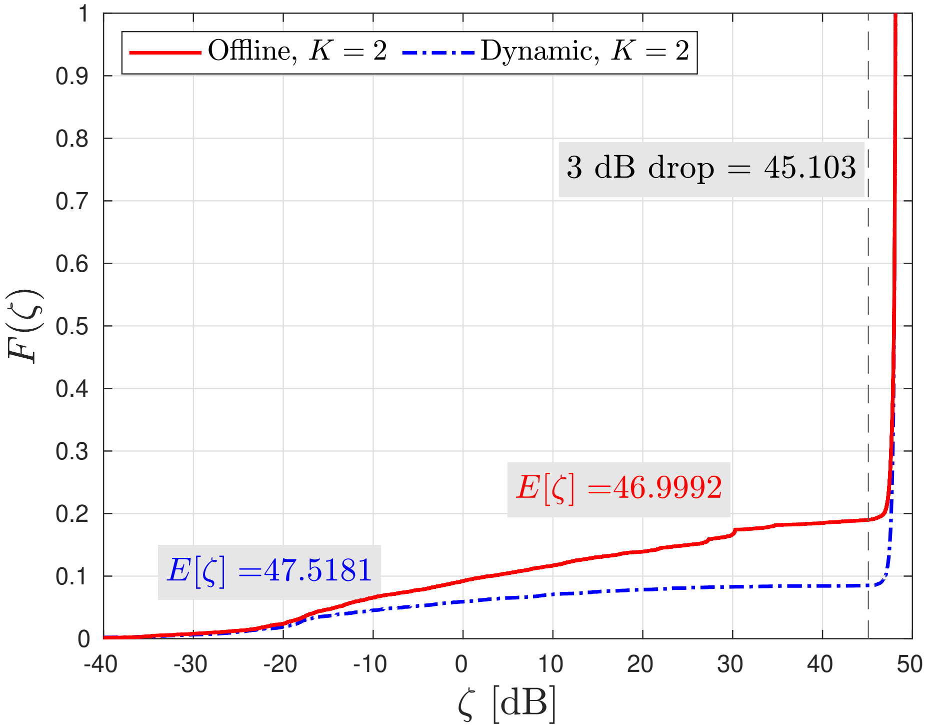

Figure 6.13: CDF of the SNR of the final refinement stage with array size, $N = 2048$

Finally, sacrificing more pilot symbols by increasing the K parameter can be satisfactory since it achieves nearly similar performance to the dynamic rule with fewer pilot symbols.

6.7 Summary

Beam discovery is critical for preserving a communication link with high spectral efficiency and avoiding prolonged disruptions, especially in fast-varying channels. Conventional solutions for the beam discovery issue depend on measuring the channel in all possible angular directions or even space sectors. By nature, traditional approaches ignore the phase information of the channel measurements and focus only on the RSS. On the contrary, by considering the phase information accompanying the channel measurements used to find the beam direction, a more innovative beam discovery approach could use that neglected information to quickly find the beam direction with a significant signaling overhead reduction.

In this chapter, we introduce a Main-Lobe Fast beam discovery solution, which employs a novel formula of the beam main-lobe approximation along with the phase information of the channel measurement to discover the beam direction. Our approach requires less signaling overhead while maintaining a similar performance to the traditional coarse-fine beam discovery.

We study the performance under different array sizes and two distinct cases of path gain errors (amplitude and phase). We show that the proposed approach sustains similar performance in the SNR compared to traditional approaches. Moreover, the Main-Lobe beam discovery achieves an overhead reduction by 42% and up to 64% in terms of pilot symbols required to discover the beam direction. Finally, we show that a large-scale antenna array no necessarily incurs significant overhead to discover the beam direction.

CHAPTER 7

CONCLUSION AND FUTURE WORK

Beam alignment is vital to maintain the desired directional gain, alleviating the severe attenuation in mmWave networks. In this study, we consider two classes of beam alignment: (1) Beam Discovery / Initial beam alignment and (2) Beam Tracking.

Beam discovery is essential to establish the communication link in the mmWave system to maximize the directional gain. In typical beam discovery approaches, a sequence of pilot symbols is exploited to measure the whole angular space, which elongates the discovery process. Those approaches neglect a vital part of the available resources, the phase information, while considering the RSS only. The associated phase of each channel measurement significantly reduces the signaling overhead.

Beam tracking is crucial in reducing the significant overhead of the beam discovery / initial beam discovery process. Conventionally, periodic symbols are exploited to measure the channel to estimate and update the beam direction. The information on the first-order variation of the beam direction between the arrival of two symbols is ignored in traditional approaches. Thus, a more innovative beam-tracking solution should leverage the gradual angle variation and continuously update the beam directions in-between pilot arrivals. A channel's continuous state transition model should be derived to perform such an approach.

In Chapter 5, a "Continuous-Discrete" beam tracking proposal is introduced that leverages system information such as the first derivative of the beam variations to implement continuous beam updates while keeping periodical pilots symbols to correct minor deviations. Our proposal requires fewer periodic reference signals while sustaining comparable tracking performance to the state-of-the-art. Actually, it can attain considerable performance when the pilot frequency is the same. The performance is studied under different SNR levels, array sizes, pilot periods, and different array configurations, i.e., ULA and UPA. In Chapter 6, a novel beam discovery approach is proposed, which utilizes an intelligent formula of the beam main-lobe approximation that maps the RSS of the channel measurement and determines a unique estimate of the beam direction using the phase information. Our method requires less signaling overhead while maintaining a similar performance to the traditional coarse-fine beam discovery.

7.1 Key outcomes

- **Beam Tracking**
  - The proposed Continuous-Discrete approach outperforms Discrete tracking algorithms in terms of overhead reduction.
  - Increasing the array size for fixed SNR and pilot period increases the tracking accuracy as long as the pilot period is comparable to the beam coherence time.
  - Larger MIMO arrays do not necessarily lead to improved beam tracking performance. This is due to the following:
    - ∗ shorter beam coherence time.
    - ∗ higher link disruption (more frequent pilot symbols), especially for pilot training time in tens of microseconds.

  - Uniform planar arrays may improve the beam tracking performance over ULAs of similar size, in terms of average SNR, due to longer beam coherence time.

- **Beam Discovery**
  - We show that there are situations where the proposed Main-Lobe beam discovery approach can reduce the signaling overhead by 42% and up to 64%.
  - We elaborate that Large-scale antenna arrays do not necessarily incur significant overhead to discover the beam direction.

7.2 Future Work

Multiple Path Tracking: In this dissertation, we have only considered tracking a single significant path and ignoring all other paths. Although the lowest complexity, we miss the benefits of multiple paths. If we can track multiple paths, we can exploit the spatial diversity to increase the transmit diversity or the multiplexing gain. **Simple Example** Let the number of discovered paths at the initial link establishment $k = 3$, and we need to track the three paths instead of one. Two proposals for applying multiple path tracking:

- **Run three parallel versions of the single beam tracking.** We need three pilot symbols for each period T for this proposal to update each path independently. In that case, increasing the number of pilot symbols exacerbates spectral efficiency.
- **Joint AoA tracking.** Here, we assume that we can model the correlation between the different paths and exploit that correlation to decrease the number

of pilots used to update the AoA. Accordingly, we can reduce the pilot overhead, and the spectral efficiency should surpass the parallel proposal.

Multiple path Discovery: In this study, we have considered the beam discovery issue under the assumption of a single dominant path received at the receiver side. In a more complex scenario, multiple paths should be considered. The proposed approach can still have considerable performance only if we can estimate the complex gain of each path arriving at the receiver side. The proposed path gain estimator does not consider multiple paths. If we exploit it for the discovery of multiple paths, it will lead to ambiguities in the dominant path gain estimate and, in turn, will exacerbate the discovery performance.

BIBLIOGRAPHY

[1] Y. Xing and T. S. Rappaport, "Millimeter Wave and Terahertz Urban Microcell Propagation Measurements and Models," *IEEE Communications Letters*, vol. 25, no. 12, pp. 3755–3759, 2021.

[2] T. S. Rappaport, Y. Xing, O. Kanhere, S. Ju, A. Madanayake, S. Mandal, A. Alkhateeb, and G. C. Trichopoulos, "Wireless Communications and Applications Above 100 GHz: Opportunities and Challenges for 6G and Beyond," *IEEE Access*, vol. 7, pp. 78 729–78 757, 2019.

[3] T. S. Rappaport, S. Sun, R. Mayzus, H. Zhao, Y. Azar, K. Wang, G. N. Wong, J. K. Schulz, M. Samimi, and F. Gutierrez, "Millimeter Wave Mobile Communications for 5G Cellular: It Will Work!" *IEEE Access*, vol. 1, pp. 335–349, 2013.

[4] T. S. Rappaport, Y. Xing, G. R. MacCartney, A. F. Molisch, E. Mellios, and J. Zhang, "Overview of Millimeter Wave Communications for Fifth-Generation (5G) Wireless Networks—With a Focus on Propagation Models," *IEEE Transactions on Antennas and Propagation*, vol. 65, no. 12, pp. 6213–6230, 2017.

[5] W. Saad, M. Bennis, and M. Chen, "A Vision of 6G Wireless Systems: Applications, Trends, Technologies, and Open Research Problems," *IEEE Network*, vol. 34, no. 3, pp. 134–142, 2020.

[6] R. W. Heath, N. González-Prelcic, S. Rangan, W. Roh, and A. M. Sayeed, "An Overview of Signal Processing Techniques for Millimeter Wave MIMO Systems," *IEEE Journal of Selected Topics in Signal Processing*, vol. 10, no. 3, pp. 436–453, 2016.

[7] M. R. Akdeniz, Y. Liu, M. K. Samimi, S. Sun, S. Rangan, T. S. Rappaport, and E. Erkip, "Millimeter Wave Channel Modeling and Cellular Capacity Evaluation," *IEEE Journal on Selected Areas in Communications*, vol. 32, no. 6, pp. 1164–1179, 2014.

[8] S. Rangan, T. S. Rappaport, and E. Erkip, "Millimeter-Wave Cellular Wireless Networks: Potentials and Challenges," *Proceedings of the IEEE*, vol. 102, no. 3, pp. 366–385, 2014.

[9] K. Haneda, J. Zhang, L. Tan, G. Liu, Y. Zheng, H. Asplund, J. Li, Y. Wang, D. Steer, C. Li, T. Balercia, S. Lee, Y. Kim, A. Ghosh, T. Thomas, T. Nakamura, Y. Kakishima, T. Imai, H. Papadopoulos, T. S. Rappaport, G. R. MacCartney, M. K. Samimi, S. Sun, O. Koymen, S. Hur, J. Park, C. Zhang, E. Mellios, A. F. Molisch, S. S. Ghassamzadeh, and A. Ghosh, "5G 3GPP-Like Channel Models for Outdoor Urban Microcellular and Macrocellular Environments," in *2016 IEEE 83rd Vehicular Technology Conference (VTC Spring)*, 2016, pp. 1–7.

[10] A. Alkhateeb, O. El Ayach, G. Leus, and R. W. Heath, "Channel Estimation and Hybrid Precoding for Millimeter Wave Cellular Systems," *IEEE Journal of Selected Topics in Signal Processing*, vol. 8, no. 5, pp. 831–846, 2014.

[11] R. Méndez-Rial, C. Rusu, A. Alkhateeb, N. González-Prelcic, and R. W. Heath, "Channel Estimation and Hybrid Combining for mmWave: Phase Shifters or Switches?" in *2015 Information Theory and Applications Workshop (ITA)*, 2015, pp. 90–97.

[12] S. Han, C.-l. I, Z. Xu, and C. Rowell, "Large-Scale Antenna Systems with Hybrid Analog and Digital Beamforming for Millimeter Wave 5G," *IEEE Communications Magazine*, vol. 53, no. 1, pp. 186–194, 2015.

[13] M. Hashemi, A. Sabharwal, C. Emre Koksal, and N. B. Shroff, "Efficient Beam Alignment in Millimeter Wave Systems Using Contextual Bandits," in *IEEE INFOCOM 2018 - IEEE Conference on Computer Communications*, 2018, pp. 2393–2401.

[14] J. Wang, Z. Lan, C. woo Pyo, T. Baykas, C. sean Sum, M. Rahman, J. Gao, R. Funada, F. Kojima, H. Harada, and S. Kato, "Beam Codebook Based Beamforming Protocol for Multi-Gbps Millimeter-Wave WPAN Systems," *IEEE Journal on Selected Areas in Communications*, vol. 27, no. 8, pp. 1390–1399, 2009.

[15] M. Enescu, *5G New Radio: A Beam-Based Air Interface*. John Wiley & Sons, 2020.

[16] Y. Shabara, C. E. Koksal, and E. Ekici, "How Long to Estimate Sparse MIMO Channels," in *2021 IEEE International Symposium on Information Theory (ISIT)*, 2021, pp. 2834–2839.

[17] V. Va, J. Choi, and R. W. Heath, "The Impact of Beamwidth on Temporal Channel Variation in Vehicular Channels and Its Implications," *IEEE Transactions on Vehicular Technology*, vol. 66, no. 6, pp. 5014–5029, 2017.

[18] M. Naguib, Y. Shabara, and C. E. Koksal, "Continuous Beam Alignment for Mobile MIMO," 2022. [Online]. Available: https://arxiv.org/abs/2208.02945

[19] T. Rappaport, R. Heath, R. Daniels, and J. Murdock, *Millimeter Wave Wireless Communications.* Prentice Hall, 2015, includes bibliographical references (pages 585-651) and index.

[20] T. S. Rappaport, J. N. Murdock, and F. Gutierrez, "State of the Art in 60-GHz Integrated Circuits and Systems for Wireless Communications," *Proceedings of the IEEE*, vol. 99, no. 8, pp. 1390–1436, 2011.

[21] G. B. T. D. of Trade and I. R. Division, *The Use of the Radio Frequency Spectrum Above 30 Ghz: A Consultative Document.* Radiocommunications Division, The Department of Trade and Industry, 1988. [Online]. Available: https://books.google.com/books?id=0nYVPAAACAAJ

[22] H. Friis, "A Note on a Simple Transmission Formula," *Proceedings of the IRE*, vol. 34, no. 5, pp. 254–256, 1946.

[23] T. Rappaport, *Wireless Communications: Principles And Practice, 2/E.* Pearson Education, 2010. [Online]. Available: https://books.google.com/books?id=VmPT8B-5_tAC

[24] C. Anderson and T. Rappaport, "In-building Wideband Partition Loss Measurements at 2.5 and 60 GHz," *IEEE Transactions on Wireless Communications*, vol. 3, no. 3, pp. 922–928, 2004.

[25] C. Anderson, T. Rappaport, K. Bae, A. Verstak, N. Ramakrishnan, W. Tranter, C. Shaffer, and L. Watson, "In-building Wideband Multipath Characteristics at 2.5 and 60 GHz," in *Proceedings IEEE 56th Vehicular Technology Conference*, vol. 1, 2002, pp. 97–101 vol.1.

[26] E. Ben-Dor, T. S. Rappaport, Y. Qiao, and S. J. Lauffenburger, "Millimeter-Wave 60 GHz Outdoor and Vehicle AOA Propagation Measurements Using a Broadband Channel Sounder," in *2011 IEEE Global Telecommunications Conference - GLOBECOM 2011*, 2011, pp. 1–6.

[27] C. Balanis, *Antenna Theory: Analysis and Design.* Wiley, 2015. [Online]. Available: https://books.google.com/books?id=u-xbCwAAQBAJ

[28] X. Guan, H. Hashemi, and A. Hajimiri, "A Fully Integrated 24-GHz Eight-element Phased-array Receiver in Silicon," *IEEE Journal of Solid-State Circuits*, vol. 39, no. 12, pp. 2311–2320, 2004.

[29] M. Giordani, M. Polese, A. Roy, D. Castor, and M. Zorzi, "A Tutorial on Beam Management for 3GPP NR at mmWave Frequencies," *IEEE Communications Surveys Tutorials*, vol. 21, no. 1, pp. 173–196, 2019.

[30] A. Alkhateeb, G. Leus, and R. W. Heath, “Compressed Sensing Based Multi-user Millimeter Wave Systems: How Many Measurements are Needed?” in *2015 IEEE International Conference on Acoustics, Speech and Signal Processing (ICASSP)*, 2015, pp. 2909–2913.

[31] C. Rusu, N. González-Prelcic, and R. W. Heath, “Low Resolution Adaptive Compressed Sensing for mmWave MIMO Receivers,” in *2015 49th Asilomar Conference on Signals, Systems and Computers*, 2015, pp. 1138–1143.

[32] Y. Shabara, “Establishing Large-Scale MIMO Communication: Coding for Channel Estimation,” Ph.D. dissertation, 2021. [Online]. Available: http://rave.ohiolink.edu/etdc/view?acc_num=osu1618578732285999

[33] S. Hur, T. Kim, D. J. Love, J. V. Krogmeier, T. A. Thomas, and A. Ghosh, “Millimeter Wave Beamforming for Wireless Backhaul and Access in Small Cell Networks,” *IEEE Transactions on Communications*, vol. 61, no. 10, pp. 4391–4403, 2013.

[34] J. Zhao, D. Xie, X. Wang, and A. Madanayake, “Towards Efficient Medium Access for Millimeter-Wave Networks,” *IEEE Journal on Selected Areas in Communications*, vol. 37, no. 12, pp. 2786–2798, 2019.

[35] L. Zhou and Y. Ohashi, “Efficient Codebook-based MIMO Beamforming for Millimeter-Wave WLANs,” in *2012 IEEE 23rd International Symposium on Personal, Indoor and Mobile Radio Communications - (PIMRC)*, 2012, pp. 1885–1889.

[36] P. Zhou, K. Cheng, X. Han, X. Fang, Y. Fang, R. He, Y. Long, and Y. Liu, “IEEE 802.11ay-Based mmWave WLANs: Design Challenges and Solutions,” *IEEE Communications Surveys Tutorials*, vol. 20, no. 3, pp. 1654–1681, 2018.

[37] S. Noh, M. D. Zoltowski, and D. J. Love, “Multi-Resolution Codebook and Adaptive Beamforming Sequence Design for Millimeter Wave Beam Alignment,” *IEEE Transactions on Wireless Communications*, vol. 16, no. 9, pp. 5689–5701, 2017.

[38] J. Song, J. Choi, and D. J. Love, “Common Codebook Millimeter Wave Beam Design: Designing Beams for Both Sounding and Communication With Uniform Planar Arrays,” *IEEE Transactions on Communications*, vol. 65, no. 4, pp. 1859–1872, 2017.

[39] Z. Xiao, C. Yin, P. Xia, and X.-G. Xia, “Codebook Design for Millimeter-Wave Channel Estimation with Hybrid Precoding Structure,” in *2016 IEEE International Conference on Communication Systems (ICCS)*, 2016, pp. 1–6.

[40] S. Noh, J. Song, and Y. Sung, "Fast Beam Search and Refinement for Millimeter-Wave Massive MIMO Based on Two-Level Phased Arrays," *IEEE Transactions on Wireless Communications*, vol. 19, no. 10, pp. 6737–6751, 2020.

[41] C. R. Berger, B. Demissie, J. Heckenbach, P. Willett, and S. Zhou, "Signal Processing for Passive Radar Using OFDM Waveforms," *IEEE Journal of Selected Topics in Signal Processing*, vol. 4, no. 1, pp. 226–238, 2010.

[42] X. Huang, Y. J. Guo, and J. D. Bunton, "A hybrid Adaptive Antenna Array," *IEEE Transactions on Wireless Communications*, vol. 9, no. 5, pp. 1770–1779, 2010.

[43] X. Huang and Y. J. Guo, "Frequency-Domain AoA Estimation and Beamforming with Wideband Hybrid Arrays," *IEEE Transactions on Wireless Communications*, vol. 10, no. 8, pp. 2543–2553, 2011.

[44] J. A. Zhang, X. Huang, V. Dyadyuk, and Y. J. Guo, "Massive Hybrid Antenna Array for Millimeter-Wave Cellular Communications," *IEEE Wireless Communications*, vol. 22, no. 1, pp. 79–87, 2015.

[45] S.-F. Chuang, W.-R. Wu, and Y.-T. Liu, "High-Resolution AoA Estimation for Hybrid Antenna Arrays," *IEEE Transactions on Antennas and Propagation*, vol. 63, no. 7, pp. 2955–2968, 2015.

[46] F. Shu, Y. Qin, T. Liu, L. Gui, Y. Zhang, J. Li, and Z. Han, "Low-Complexity and High-Resolution DOA Estimation for Hybrid Analog and Digital Massive MIMO Receive Array," *IEEE Transactions on Communications*, vol. 66, no. 6, pp. 2487–2501, 2018.

[47] H. Li, T. Q. Wang, X. Huang, and Y. Jay Guo, "Adaptive AoA and Polarization Estimation for Receiving Polarized mmWave Signals," *IEEE Wireless Communications Letters*, vol. 8, no. 2, pp. 540–543, 2019.

[48] C. Qin, J. A. Zhang, X. Huang, and Y. J. Guo, "Virtual-Subarray-Based Angle-of-Arrival Estimation in Analog Antenna Arrays," *IEEE Wireless Communications Letters*, vol. 9, no. 2, pp. 194–197, 2020.

[49] J. A. Zhang, W. Ni, P. Cheng, and Y. Lu, "Angle-of-Arrival Estimation Using Different Phase Shifts Across Subarrays in Localized Hybrid Arrays," *IEEE Communications Letters*, vol. 20, no. 11, pp. 2205–2208, 2016.

[50] K. Wu, W. Ni, T. Su, R. P. Liu, and Y. J. Guo, "Robust Unambiguous Estimation of Angle-of-Arrival in Hybrid Array With Localized Analog Subarrays," *IEEE Transactions on Wireless Communications*, vol. 17, no. 5, pp. 2987–3002, 2018.

[51] K. Wu, W. Ni, T. Su, R. P. Liu, and Y. J. Guo, “Fast and Accurate Estimation of Angle-of-Arrival for Satellite-Borne Wideband Communication System,” *IEEE Journal on Selected Areas in Communications*, vol. 36, no. 2, pp. 314–326, 2018.

[52] V. Va, H. Vikalo, and R. W. Heath, “Beam Tracking for Mobile Millimeter Wave Communication Systems,” in *2016 IEEE Global Conference on Signal and Information Processing (GlobalSIP)*, 2016, pp. 743–747.

[53] J. Li, Y. Sun, L. Xiao, S. Zhou, and C. E. Koksal, “Fast Analog Beam Tracking in Phased Antenna Arrays: Theory and Performance,” 2017. [Online]. Available: https://arxiv.org/abs/1710.07873v4

[54] J. Lim, H.-M. Park, and D. Hong, “Beam Tracking Under Highly Nonlinear Mobile Millimeter-Wave Channel,” *IEEE Communications Letters*, vol. 23, no. 3, pp. 450–453, 2019.

[55] E. Khordad, I. B. Collings, S. V. Hanly, and G. Caire, “Millimeter Wave Beam Alignment with Symbol Based Beam Switching for Wideband Time-varying Channels,” in *2021 15th International Conference on Signal Processing and Communication Systems (ICSPCS)*, 2021, pp. 1–5.

[56] X. Song, S. Haghighatshoar, and G. Caire, “A Scalable and Statistically Robust Beam Alignment Technique for Millimeter-Wave Systems,” *IEEE Transactions on Wireless Communications*, vol. 17, no. 7, pp. 4792–4805, 2018.

[57] A. Valdes-Garcia, S. T. Nicolson, J.-W. Lai, A. Natarajan, P.-Y. Chen, S. K. Reynolds, J.-H. C. Zhan, D. G. Kam, D. Liu, and B. Floyd, “A Fully Integrated 16-Element Phased-Array Transmitter in SiGe BiCMOS for 60-GHz Communications,” *IEEE Journal of Solid-State Circuits*, vol. 45, no. 12, pp. 2757–2773, 2010.

[58] B. Sadhu, Y. Tousi, J. Hallin, S. Sahl, S. K. Reynolds, Renström, K. Sjögren, O. Haapalahti, N. Mazor, B. Bokinge, G. Weibull, H. Bengtsson, A. Carlinger, E. Westesson, J.-E. Thillberg, L. Rexberg, M. Yeck, X. Gu, M. Ferriss, D. Liu, D. Friedman, and A. Valdes-Garcia, “A 28-GHz 32-Element TRX Phased-Array IC With Concurrent Dual-Polarized Operation and Orthogonal Phase and Gain Control for 5G Communications,” *IEEE Journal of Solid-State Circuits*, vol. 52, no. 12, pp. 3373–3391, 2017.

[59] R. Bonjour, M. Singleton, S. A. Gebrewold, Y. Salamin, F. C. Abrecht, B. Baeuerle, A. Josten, P. Leuchtmann, C. Hafner, and J. Leuthold, “Ultra-Fast Millimeter Wave Beam Steering,” *IEEE Journal of Quantum Electronics*, vol. 52, no. 1, pp. 1–8, 2016.

[60] S. Jiang and A. Alkhateeb, “Computer Vision Aided Beam Tracking in A Real-World Millimeter Wave Deployment,” 2021. [Online]. Available: https://arxiv.org/abs/2111.14803

[61] M. Alrabeiah and A. Alkhateeb, "Deep Learning for mmWave Beam and Blockage Prediction Using Sub-6 GHz Channels," *IEEE Transactions on Communications*, vol. 68, no. 9, pp. 5504–5518, 2020.

[62] G. Charan, M. Alrabeiah, and A. Alkhateeb, "Vision-Aided 6G Wireless Communications: Blockage Prediction and Proactive Handoff," *IEEE Transactions on Vehicular Technology*, vol. 70, no. 10, pp. 10 193–10 208, 2021.

[63] M. Alrabeiah, A. Hredzak, and A. Alkhateeb, "Millimeter Wave Base Stations with Cameras: Vision-Aided Beam and Blockage Prediction," in *2020 IEEE 91st Vehicular Technology Conference (VTC2020-Spring)*, 2020, pp. 1–5.

[64] M. Alrabeiah, U. Demirhan, A. Hredzak, and A. Alkhateeb, "Vision Aided URLL Communications: Proactive Service Identification and Coexistence," in *2020 54th Asilomar Conference on Signals, Systems, and Computers*, 2020, pp. 174–178.

[65] T.-H. Chou, N. Michelusi, D. J. Love, and J. V. Krogmeier, "Fast Position-Aided MIMO Beam Training via Noisy Tensor Completion," *IEEE Journal of Selected Topics in Signal Processing*, vol. 15, no. 3, pp. 774–788, 2021.

[66] M. Naguib, Y. Shabara, and C. E. Koksal, "Continuous-Discrete Analog Beam Tracking for Large-Scale MIMO Systems," in *2022 56th Asilomar Conference on Signals, Systems, and Computers*, 2022.

[67] T. S. Rappaport, G. R. MacCartney, M. K. Samimi, and S. Sun, "Wideband Millimeter-Wave Propagation Measurements and Channel Models for Future Wireless Communication System Design," *IEEE Transactions on Communications*, vol. 63, no. 9, pp. 3029–3056, 2015.

[68] F. L. Lewis, L. Xie, and D. Popa, *Optimal and Robust Estimation: With an Introduction to Stochastic Control Theory.* CRC Press, 2008.

[69] D. Tse and P. Viswanath, *Fundamentals of Wireless Communication.* Cambridge University Press, 2005.

APPENDIX A: PROOFS FOR CHAPTER 5

A.1 Proof of Theorem 1 Part 1

Proof. From Eqs. (5.23) and (5.24), and given the assumption of $P(t) = 1$ and replacing $\phi(t + Tb)$, and $\phi(t)$ by ϕ_{k+1} and ϕ_k respectively, then:

$$\zeta = \frac{1}{N^2} \left| \sum_{m=0}^{N-1} e^{-j2\pi m\Delta(\cos(\phi_{k+1}) - \cos(\phi_k))} \right|^2 \tag{A.1}$$

Using the approximation given in Eq. (5.16), then ζ is given by:

$$\zeta \approx e^{-N^2[\cos(\phi_{k+1}) - \cos(\phi_k)]^2} \tag{A.2}$$

The discrete representation of the AoA model in Eq. (4.7) using *pilot period* $T = T_b$ is given by:

$$\phi_{k+1} = \phi_k + T_b\,\dot{\phi}_k \tag{A.3}$$

Now, we simplify the cosine difference in Eq. (A.2) using the discrete representation in Eq. (A.3) and $T_b\,\dot{\phi}_k \ll 1$ as follows:

$$\begin{aligned} \cos(\phi_{k+1}) &= \cos(\phi_k + T_b\,\dot{\phi}_k) \\ &= \cos(\phi_k)\cos(T_b\,\dot{\phi}_k) - \sin(\phi_k)\sin(T_b\,\dot{\phi}_k) \\ &\approx \cos(\phi_k) - T_b\,\dot{\phi}_k\,\sin(\phi_k) \end{aligned} \tag{A.4}$$

Hence, the cosine difference in Eq. (A.2) is given by:

$$\cos(\phi_{k+1}) - \cos(\phi_k) \approx -T_b\,\dot{\phi}_k\,\sin(\phi_k) \tag{A.5}$$

Now, let $T_{LR} = K\,T_b$, and define $\mu_\zeta \triangleq \mathbb{E}\,[\zeta|T_b\,,\phi_k]$, since $\dot{\phi}_k \sim \mathcal{N}(0, Q\,T_{LR})$

$$\implies \zeta = e^{-(NT_b\sin(\phi_k))^2\dot{\phi}_k^2}. \tag{A.6}$$

Hence,

$$\begin{aligned}\mu_\zeta &= \int_{-\infty}^{\infty}\frac{1}{\sqrt{2\pi\,QT_{LR}}}\,e^{-\left(T_bN\sin(\phi_k)\right)^2x^2}\,e^{-\frac{x^2}{2QT_{LR}}}dx\\ &= \sqrt{\frac{\sigma_d^2}{QT_{LR}}}\int_{-\infty}^{\infty}\frac{1}{\sqrt{2\pi\,\sigma_d^2}}\,e^{-\frac{x^2}{2\sigma_d^2}}dx\\ &= \sqrt{\frac{\sigma_d^2}{QT_{LR}}},\end{aligned} \tag{A.7}$$

where $\sigma_d^2 = QT_{LR}/\left(1 + 2QT_{LR}\,(T_bN\sin(\phi_k))^2\right)$, then:

$$\begin{aligned}\mu_\zeta &= \sqrt{\frac{1}{\left(1 + 2QT_{LR}\,(T_bN\sin(\phi_k))^2\right)}}\\ \implies T_b &= \sqrt{\frac{1/\mu_\zeta^2 - 1}{2\,Q\,T_{LR}\,\sin^2(\phi_k)N^2}}\end{aligned} \tag{A.8}$$

$\square$

A.2 Proof of Theorem 1 Part 2

Proof. Here, we follow similar steps like in Appendix A.1 but we are going to replace $\phi(t)$ by $\phi_k + T_L\hat{\dot{\phi}}_{k-1}$ since in a continuous-discrete tracking we continuously update the beamforming in-between pilot symbols. In that case, the cosine difference in Eq. (A.2) is given by:

$$\begin{aligned}\cos(t+T_L) - \cos(t) &= \cos(\phi_k + T_L\dot{\phi}_k) - \cos(\phi_k + T_L\hat{\dot{\phi}}_{k-1}) \\ &\approx -T_L \sin(\phi_k)\varepsilon_k,\end{aligned} \tag{A.9}$$

where $\varepsilon_k = \dot{\phi}_k - \hat{\dot{\phi}}_{k-1}$, and by assuming perfect estimate of the slope variation, i.e., $\hat{\dot{\phi}}_{k-1} = \dot{\phi}_{k-1}$, then $\varepsilon_k \sim \mathcal{N}(0, \alpha QT_{LR})$ for $0 < \alpha < 1$

$$\implies \zeta = e^{-(NT_L\sin(\phi_k))^2\varepsilon_k^2}. \tag{A.10}$$

Hence,

$$\begin{aligned}\mu_\zeta &= \int_{-\infty}^{\infty} \frac{e^{-\frac{x^2}{2\alpha\, QT_{LR}}}}{\sqrt{2\pi\,\alpha\, QT_{LR}}}\, e^{-\left(T_L N\sin(\phi_k)\right)^2 x^2}\, dx \\ &= \sqrt{\frac{\sigma_{cd}^2}{QT_{LR}}} \int_{-\infty}^{\infty} \frac{1}{\sqrt{2\pi\,\sigma_{cd}^2}}\, e^{-\frac{x^2}{2\sigma_{cd}^2}}\, dx \\ &= \sqrt{\frac{\sigma_{cd}^2}{\alpha\, QT_{LR}}},\end{aligned} \tag{A.11}$$

where $\sigma_{cd}^2 = \alpha\, QT_{LR}/\left(1 + 2\alpha\, QT_{LR}\,(T_L N\sin(\phi_k))^2\right)$, then:

$$\begin{aligned}\mu_\zeta &= \sqrt{\frac{1}{\left(1 + 2\alpha\, QT_{LR}\,(T_L N\sin(\phi_k))^2\right)}} \\ \implies T_L &= \sqrt{\frac{1/\mu_\zeta^2 - 1}{2\,\alpha\, Q\, T_{LR}\, \sin^2(\phi_k) N^2}}\end{aligned} \tag{A.12}$$

□

A.3 Proof of γ Distribution

Proof. **Discrete Tracking Approach:**

From Eq. (4.8), the instantaneous received SNR is given by:

$$\begin{aligned}\gamma_k &= \rho \left| \frac{1}{N} \sum_{m=0}^{N-1} e^{-j2\pi\Delta m[\cos(\phi_k)-\cos(\bar{\phi}_k)]} \right|^2 \\ &\approx \rho\, \zeta_k\end{aligned} \tag{A.13}$$

and assuming small slope variations during pilot duration, i.e., $T\dot{\phi}_k \ll 1$, for a given value of ϕ_k, and using Eq. (A.6) then:

$$\gamma_k = \rho\, e^{-N^2T^2\sin^2(\phi_k)\,\dot{\phi}_k^2} \tag{A.14}$$

using the Cumulative Distribution Function (CDF) way:

$$\begin{aligned}F(\gamma_k|\phi_k) &= P(\gamma \le \gamma_k|\phi_k) \\ &= P(\rho\, e^{-N^2T^2\sin^2(\phi_k)\,\dot{\phi}_k^2} \le \gamma_k|\phi_k) \\ &= P(e^{-N^2T^2\sin^2(\phi_k)\,\dot{\phi}_k^2} \le \frac{\gamma_k}{\rho}|\phi_k) \\ &= P(-N^2T^2\sin^2(\phi_k)\,\dot{\phi}_k^2 \le \log(\gamma_k/\rho)\,|\phi_k) \\ &= P\left(\dot{\phi}_k^2 \ge \frac{\log(\rho/\gamma_k)}{N^2T^2\sin^2(\phi_k)}|\phi_k\right) \\ &= 1 - P\left(\dot{\phi}_k^2 \le \frac{\log(\rho/\gamma_k)}{N^2T^2\sin^2(\phi_k)}|\phi_k\right)\end{aligned} \tag{A.15}$$

since $\dot{\phi}_k \sim \mathcal{N}(0, QT_{LR})$, then the squared of $\dot{\phi}_k$ has a Chi-Squared distribution with one degree of freedom. Hence,

$$P\left(\dot{\phi}_k^2 \leq \dot{\varphi}\right) = 1 - 2\,\mathbb{Q}\left(\sqrt{\frac{\dot{\varphi}}{QT_{LR}}}\right) \tag{A.16}$$

This implies;

$$F(\gamma_k|\phi_k) = 2\,\mathbb{Q}\left(\sqrt{\frac{\log\left(\rho/\gamma_k\right)}{N^2T^2\sin^2(\phi_k)QT_{LR}}}\right) \tag{A.17}$$

The Probability Density Function (PDF) is found by taking the derivative of the CDF:

$$\begin{aligned} f(\gamma_k|\phi_k) &= \frac{\partial F(\gamma_k|\phi_k)}{\partial \gamma_k} \\ &= 2\frac{\partial}{\partial \gamma_k}\left(\int_{\sqrt{\log(\frac{\rho}{\gamma_k})}}^{\infty} \frac{e^{-\frac{t^2}{2N^2T^2\sin^2(\phi_k)QT_{LR}}}}{\sqrt{2\pi N^2T^2\sin^2(\phi_k)QT_{LR}}}\,dt\right) \\ &= \frac{e^{-\frac{\log(\rho/\gamma_k)}{2N^2T^2\sin^2(\phi_k)QT_{LR}}}}{\gamma_k\sqrt{\log(\rho/\gamma_k)}} \end{aligned} \tag{A.18}$$

Continuous-Discrete Tracking Approach:

Following similar procedure as in the discrete case, and using Eq. (A.10) then,

$$\gamma_k = \rho\, e^{-N^2T^2\sin^2(\phi_k)\,\varepsilon_k^2} \tag{A.19}$$

Here, we can see the difference between Eqs. (A.14) and (A.19) is replacing $\dot{\phi}_k$ by $\varepsilon_k \sim \mathcal{N}(0, \alpha\, QT_{LR})$, then the CDF is given by:

$$\begin{aligned} F(\gamma_k|\phi_k) &= 1 - P\left(\varepsilon_k^2 \leq \frac{\log(\rho/\gamma_k)}{N^2T^2\sin^2(\phi_k)}|\phi_k\right) \\ &= 1 - 1 + 2\,\mathbb{Q}\left(\sqrt{\frac{\log(\rho/\gamma_k)}{N^2T^2\sin^2(\phi_k)\alpha\, QT_{LR}}}\right) \\ &= 2\,\mathbb{Q}\left(\sqrt{\frac{\log(\rho/\gamma_k)}{N^2T^2\sin^2(\phi_k)\alpha\, QT_{LR}}}\right) \end{aligned} \tag{A.20}$$

Similarly, the PDF is given by:

$$f(\gamma_k|\phi_k) = \; = \frac{e^{-\frac{\log(\rho/\gamma_k)}{2N^2T^2\sin^2(\phi_k)\alpha\, QT_{LR}}}}{\gamma_k\sqrt{\log(\rho/\gamma_k)}} \tag{A.21}$$

□

APPENDIX B: PROOFS FOR CHAPTER 6

B.1 Proof of Theorem 3

Proof. First, the lower bound of the number of channel measurements (pilot symbols) is the number of pilots utilized to perform beam sweeping with equally spaced beams that cover the space. Then we have,

$$N_o \leq \widetilde{N}_P \tag{B.1}$$

After that, we utilize the criteria proposed in Section 6.5 and check whether each fine stage satisfies that criteria. Then the upper bound of the number of pilot symbols is a function of that criteria. Then we start to find the upper bound of the squared error. Let us start by the approximation formula given by Eq. (6.9), and define the following: (1) $|h| \triangleq \left|h(\Omega, \bar{\Omega})\right|$, (2) $\left|\hat{h}\right| \triangleq \left|h(\bar{\Omega}, \hat{\Omega})\right|$, (3) $\mathcal{E} \triangleq \Omega - \hat{\Omega}$, (4) $\bar{\mathcal{E}} \triangleq \Omega - \bar{\Omega}$, (5) $\hat{\mathcal{E}} \triangleq \bar{\Omega} - \hat{\Omega}$, and (6) $f(\mathcal{E}) \triangleq \exp\left(-\frac{N^2}{2}\varepsilon^2\right)$. Recall from Fig. 6.2 that f is the approximation which is a concave function, as well as $|h|$ if and only if the angles are limited to the main lobe (first null). Then we can have the following:

$$f\left(\lambda\,\bar{\mathcal{E}} + (1-\lambda)\,\hat{\mathcal{E}}\right) \geq \lambda\, f\left(\bar{\mathcal{E}}\right) + (1-\lambda)\, f\left(\hat{\mathcal{E}}\right), \tag{B.2}$$

for any $\bar{\mathcal{E}}$, and $\hat{\mathcal{E}} \in [\bar{\Omega} - \frac{2}{N}, \bar{\Omega} + \frac{2}{N}]$, and $\forall \lambda \in [0,1]$. For $\lambda = 1/2$, we can say that:

$$\begin{aligned} f\left(\frac{(\bar{\mathcal{E}} + \hat{\mathcal{E}})}{2}\right) &= f\left(\frac{\mathcal{E}}{2}\right) \\ &\geq \frac{1}{2}\left(f\left(\bar{\mathcal{E}}\right) + f\left(\hat{\mathcal{E}}\right)\right) \end{aligned} \tag{B.3}$$

Now, we replace $f\left(\bar{\mathcal{E}}\right)$, $f\left(\hat{\mathcal{E}}\right)$ by $|h|$, and $|\hat{h}|$. Then we have,

$$\begin{aligned} f\left(\frac{\mathcal{E}}{2}\right) &= \exp\left(\frac{-N^2\,\mathcal{E}^2}{8}\right) \\ &\geq \frac{1}{2}\left[|h| + |\hat{h}|\right] \end{aligned} \tag{B.4}$$

This implies,

$$\mathcal{E}^2 \leq -\frac{8}{N^2}\log\left(\frac{1}{2}\left[|h| + |\hat{h}|\right]\right) \tag{B.5}$$

Up to this point, we can utilize the upper bound in Eq. (B.5) as the criteria to determine whether we need refinement. However, this is valid for a *Dynamic Decision* where the number of refinements needed and the number of equipped antenna elements at each refinement stage are random variables. Finally, in the *Dynamic Decision*, we assume $|h| = 0.6$, which is the intersection point between the overlapped beams utilized at the coarse stage. Also, $|\hat{h}|$ is given from the previous stage.

On the other hand, an *Offline Decision* means we determine the number of refinements needed and the corresponding array sizes before we start the discovery approach. However, in that case, we need to have the knowledge of the complex path gain distribution, which is assumed as $\alpha \sim \mathcal{CN}(0,1)$. Also, we assume the knowledge of the average SNR ρ, and the estimate of the path gain $|\hat{\alpha}|$ is given. Now, we need to find the upper bound in Eq. (B.5) with a specified probability. Based on the previous assumptions, and since $|\hat{h}| = \dfrac{\rho}{\rho+1}|\delta\, h + \bar{n}_k|$, then $|\hat{h}| \sim \text{Rayleigh}(\tilde{\sigma}/\sqrt{2})$. Now, using the CDF method to find the distribution of the squared-error as follows:

$$\begin{aligned} P\left(\varepsilon^2 \leq \varepsilon^2_{_{Um}}\right) &= P\left(-\frac{8}{N^2}\log\left(\frac{1}{2}\left[|h| + |\hat{h}|\right]\right) \leq \varepsilon^2_{_{Um}}\right) \\ &= P\left(\log\left(\frac{1}{2}\left[|h| + |\hat{h}|\right]\right) \geq -\frac{N^2\varepsilon^2_{_{Um}}}{8}\right) \\ &= P\left(|\hat{h}| \geq 2\exp\left(-\frac{N^2\varepsilon^2_{_{Um}}}{8}\right) - |h|\right) \\ &= \exp\left(-\frac{\left(2\exp\left(-\frac{N^2\varepsilon^2_{_{Um}}}{8}\right) - |h|\right)^2}{\tilde{\sigma}^2_m}\right) \end{aligned} \tag{B.6}$$

where, $\tilde{\sigma}^2_m = \left(\dfrac{\rho_m}{\rho_m+1}\right)^2\left[\dfrac{\rho_m\,|h|^2+1}{\rho_m\,|\hat{\alpha}|^2}\right]$, $\rho_m = N_m\,\rho_a$. Now, for a given probability we can have a closed form for the squared-error as follows:

$$\varepsilon^2_{_{Um}} = -\frac{8}{N^2}\log\left(\frac{1}{2}\left[|h| + \sqrt{\tilde{\sigma}^2_m\,\log\left(1/P\right)}\right]\right) \tag{B.7}$$

Now, at each stage, we can have an upper bound of the squared error, which means we can decide whether to have a fine stage based on comparing the upper bound with the allowed squared error for the full array size from Eq. (6.10). An indicator function is a good metric to present the need for a fine stage or not, then we have the number of the fine stages as follows:

$$\sum_{m=0}^{\infty}\mathbb{1}\left(\varepsilon^2_{_{Um}} > \frac{\log 1/\zeta}{N^2}\right) \tag{B.8}$$

Then, the total number of channel measurements is $N_{_o}$ in addition to the results of Eq. (B.8), then we have an upper bound of the channel measurement as follows:

$$\widetilde{N}_P \leq N_o + \sum_{m=0}^{\infty} \mathbb{1}\left(\varepsilon^2_{_{Um}} > \frac{\log 1/\zeta}{N^2}\right) \tag{B.9}$$

$\square$